DISSERTATION

MEASURING DISSOLUTION RATES AND INTERFACIAL ENERGETICS OF MONOLAYER MOLYBDENUM DISULFIDE ELECTRODES IN ELECTROCHEMICAL SYSTEMS

Submitted by

Justin R. Toole

Department of Chemistry

In partial fulfillment of the requirements

For the Degree of Doctor of Philosophy

Colorado State University

Fort Collins, Colorado

Summer 2023

Doctoral Committee:

Advisor: Justin Sambur

Chuck Henry
Chris Ackerson
Stuart Field

ABSTRACT

MEASURING DISSOLUTION RATES AND INTERFACIAL ENERGETICS OF MONOLAYER MOLYBDENUM DISULFIDE ELECTRODES IN ELECTROCHEMICAL SYSTEMS

Meeting carbon zero goals within the next few decades requires advances in energy conversion efficiency, and hydrogen fuel is believed to be a key part of the solution. Photoelectrochemical (PEC) devices can contribute to a renewable-based energy portfolio by directly producing storable chemical fuels. The electrode is a key component that determines what is thermodynamically and kinetically possible for a given PEC device. Unfortunately, semiconductor electrode efficiency can come at the cost of chemical stability. Also, the energetic description of an ultra-thin semiconductor electrode at the liquid interface is unclear. Here, we studied molybdenum disulfide (MoS_2), a promising two-dimensional (2D) semiconductor, to improve understanding of interfacial energetics and electron transfer. The overarching hypothesis of this work is: if we quantitatively measure band energies of this 2D material, then we improve understanding of electron transfer efficiency and rates for involved chemical reactions. Knowledge from this research informs new ways to reduce solar energy conversion losses and may improve control over chemical reactions. Our experimental approach is to make *in situ* optical measurements while changing two key variables: (1) the electrode applied voltage (E), and (2) the liquid redox electrolyte environment ($E^{0\prime}$).

This thesis is organized into six chapters. Chapter 1 motivates semiconductor photoelectrochemistry as a viable approach for solar energy and chemical fuel production. Following the chronology of key scientific advances over the past few decades, Chapter 2 delves deeper into the established principles of semiconductor photoelectrochemistry, the unique properties of monolayer MoS_2, and the current state of the field for making *in situ* optical measurements in an electrochemical cell. This chapter concludes with open questions that are addressed in Chapters 3 – 5. In Chapter 3, the stability of

MoS_2 is tested by literally pushing the semiconductor to its anodic decomposition limit. The crucial results are identification of the MoS_2 dissolution onset potential (E_D) and its thickness-dependent dissolution rates. Additional insights pertain to the long-term stability differences between monolayer and multilayer material. Chapter 4 includes the most noteworthy results wherein we develop a method to quantitatively measure the electronic band gap of monolayer MoS_2 using a relatively simple optical setup. For the first time, we use an all-optical approach and many-body theory to report an abrupt change in potential-dependent band gap energies of monolayer MoS_2 under electrochemical conditions. Chapter 5 summarizes preliminary work investigating how redox couples in the electrolyte may tune the optical signature of a monolayer MoS_2 electrode. Finally, Chapter 6 concludes the thesis with suggestions for subsequent investigations available based on the expertise and resources within the Sambur group at Colorado State University.

ACKNOWLEDGEMENTS

In autobiographical order:

Mooooooommm

D.O.D.

My Brudder

Kimmeh

Sallye Martin

Richard Garfield

John Prine

Kiddo

Shane Kuykendall

Walker Percy

Ben Britt

Lacky

Geoff Smith

Bean

Sal Khan

Benjammin

Justin Sambur

DEDICATION

To those who live authentically and love unconditionally.

TABLE OF CONTENTS

CHAPTER 1: MOTIVATION

Current solar energy conversion is limited to approximately 33% efficiency for semiconducting materials.[1–3] Eliminating thermalization losses during the energy conversion process could double efficiency (i.e., increase efficiency to 66%).[3,4] Thermalization losses occur because absorbed photon energy exceeds a material's band gap and then so-called "hot-carriers" quickly cool down to the band edge *before* the electron is transferred. Understanding hot carrier extraction is a broad goal that may guide future solar electrocatalysis and energy conversion engineering. Another broad goal is to improve efficiency of converting solar energy directly into storable chemical fuels. Control over the kinetics and thermodynamics requires a better understanding of what is happening at the site of electron transfer. This dissertation focuses on a new class of semiconducting materials, atomically thin two-dimensional (2D) transition metal dichalcogenides (TMDs), that have the potential to increase solar energy conversion efficiency via hot carrier-induced photochemistry. My research tackles current knowledge gaps in the field by measuring the energetics involved with electron transfer from a 2D semiconductor. This is important because a 2D semiconductor may have the unique ability to extract hot-carriers and tune charge transfer rates. Figure 1.1 shows a scheme of how this may be possible for a 2D semiconductor. Electron transfer out of the semiconductor occurs at the Conduction Band (CB) edge, so hot electron capture increases overall efficiency. Also, the conduction band energy states may be more tunable to improve electron transfer and drive a specific chemical reaction or avoid unwanted reactions. Perhaps we can find an "electrochemical switch" or "reaction throttle" by using the electronic tunability of 2D semiconductors.

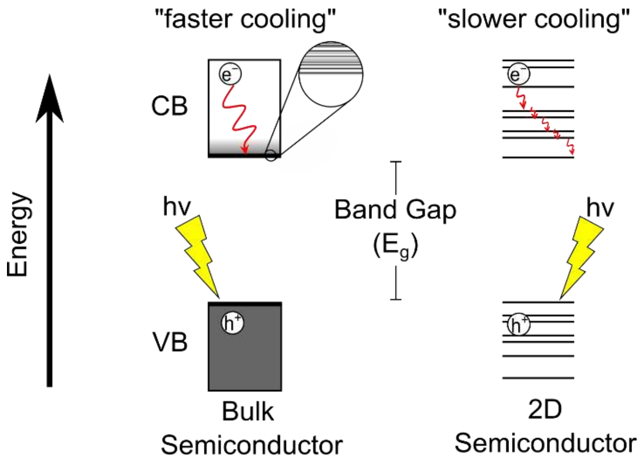

Fig. 1.1 – "Cooling" of Photoexcited Electrons in Bulk and Quantum-Confined Semiconductors. This comparative scheme shows photogeneration of electrons (e^-) and holes (h^+) into the conduction band (CB) and valence band (VB), respectively. The "hot" electrons cool faster through the CB continuum of a bulk semiconductor compared to the quantized states of a 2D semiconductor crystal. The magnified inset highlights the higher density of states in the CB for a bulk semiconductor.

We will also consider the role of the redox environment in electronically doping the semiconductor and influencing interfacial energetics. This is not a search for a Holy Grail material but rather a fundamental study to measure the unique behavior of a 2D semiconductor that may inspire improved pathways to solar energy conversion efficiency.

1.1 Converting Solar Energy with an Electrochemical Cell

Most commercial solar energy conversion devices are solid-state junction systems comprised of semiconducting silicon material. Yet for decades it has been known that a photoelectrochemical (PEC) device is an alternative approach to convert solar energy using a semiconductor-electrolyte junction. So why aren't PEC cells the leading commercial solar devices today? One primary reason is because of the trade-off between efficiency and photocorrosion rates of semiconductors in a liquid electrolyte environment.[5] For example, a more stable semiconductor electrode tends to have a wider band gap but suffers from poorer efficiency. This trade-off is not fundamental, so better semiconductors may exist that are both chemically robust and efficient. Importantly, a liquid environment is uniquely advantageous for making chemical fuels.[6] One can envision flowing reactant feedstocks into a cell, converting solar energy into a target reaction, and then capturing chemical products from the liquid solution. A PEC electrode in a liquid electrolyte environment is a logical system. If PEC devices are ever going to be a viable commercial approach in solar energy conversion, more fundamental knowledge is required to answer current questions in this field. Specifically, what is an accurate energetic description at the 2D electrode interface and how can electron transfer be controlled?

In the next chapter, we present a more robust explanation of the fundamental challenges and opportunities of a specific semiconductor photoelectrode. Here we summarize two major challenges. First, the timing is difficult when trying to capture an "uncooled" photogenerated electron. A PEC device is attractive if the goal is to harness the excess energy of hot-carriers to drive a reaction and control charge transfer rates.[7–10] As seen above in Fig. 1.1, if a photon's energy $h\upsilon$ exceeds the band gap energy of a semiconductor, then charge carriers (electrons (e^-) and holes (h^+)) are photogenerated in the semiconductor. The semiconductor bandgap is a minimum energy input requirement. However, the absorbed photon energy is the maximum energy available for energy transfer. Typically, within a picosecond the excited electron rapidly cools to the conduction band (CB) edge.[11,12] A current challenge in the field is how to make use of photogenerated hot carriers, and PEC cells uniquely place all the reactants near the surface where charge carriers are generated.

The second challenge is understanding the thermodynamics that drive a chemical reaction. PEC cells are the most efficient devices to directly convert sunlight into chemical energy.[4] The direct production of chemical products is unique for photoelectrochemical cells. For example, consider reducing liquid H_2O at a semiconducting electrode to directly produce H_2. Once sunlight reaches the semiconductor, reactants are co-located, and spontaneous charge transfer can proceed across the electrode-liquid interface. For heterogenous charge transfer, we must consider the energetics for both sides of the semiconductor-liquid junction. For a thermodynamically spontaneous (i.e., "downhill") reaction, the energy of the photoexcited electron in the electrode must exceed an available energy state in the liquid. A current knowledge gap for the field is what this interface looks like energetically.

Toward the first challenge, the Sambur group at Colorado State University, along with collaborators, investigate the kinetic challenge of extracting hot carriers.[13] In a parallel effort, this dissertation focuses on the challenge involving the energetics at the semiconductor-liquid interface. Measuring the semiconductor band edge energy enables tuning of the charge transfer rate for a reaction in the liquid. In other words, we want to tune the semiconductor to drive a chemical reaction as fast as possible. Fundamentally, before application, we must first describe and measure the energetics at the semiconductor electrode interface.

1.2 Charge Transfer Driving Force: ΔG_{CT}

Keeping solar energy conversion in mind, we want to find ways to make the semiconductor-liquid interface useful. If we consider the photoexcited electron as a reactant in the semiconductor, we wish to transfer the electron into the liquid so it may react to make new products in the liquid. The fundamental driving force for this charge transfer is the Gibbs free energy, ΔG_{CT}. This is depicted in Fig. 1.2 by the relative energy of the conduction band edge (E_{CB}) compared to the chemical potential of the semiconductor (E_F). Thus, a negative free energy of electron transfer is a thermodynamically spontaneous process.

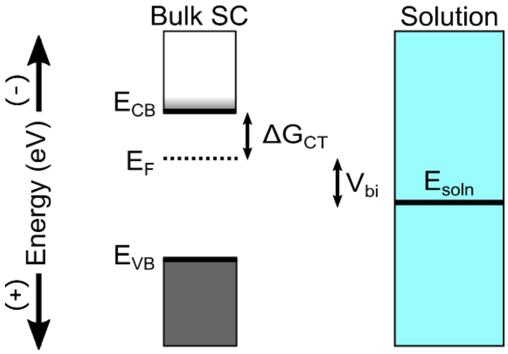

Fig. 1.2 – Relative Energetics of an Example Semiconductor (SC) and Solution. Note the energy is shown in electron volts (eV) and the built-in potential (V_{bi}) is determined by the semiconductor Fermi energy (E_F) and the electrochemical potential of the solution (E_{soln}).

In the classic model of the semiconductor-liquid interface, changing the redox environment (i.e., shifting E_{soln}) has no effect on ΔG_{CT}. In other words, the interfacial energetics are “pinned” relative to the semiconductor band edge energies. The key point is that if we want more control of the free energy of charge transfer, then we should look beyond a classic bulk semiconductor electrode in a PEC device. As will be explained in the next chapter, a logical next step is to map the energies of new semiconductor-electrolyte systems that may not be constrained by this classic thermodynamic description.

1.3 Solar Energy Conversion Frontier – Two Dimensional (2D) Semiconductors

To fundamentally advance large-scale energy production, consider some of the properties of an ideal semiconductor electrode used in a PEC application. Global change will not be accomplished with exceptionally rare materials. It turns out that certain 2D semiconductors are promising electrodes for solar energy applications considering size, flexibility, cost, and performance.[14–16] The "sheetlike" nature of an atomically-thin semiconductor limits photogenerated charge carriers to within a nanometer of the surface. A monolayer material is essentially nothing more than an interface. A 2D semiconductor may be the ideal geometry to capture sunlight and maximize the reaction surface area used to catalyze or otherwise support a chemical reaction. For example, photoexcited electrons in the conduction band of monolayer molybdenum disulfide (MoS_2) remain within 7 Å of the surface. However, 2D semiconductor energetics (i.e. conduction and valence band edges) are not well understood.[17–19] Traditional methods of measuring energetics of 2D materials are difficult if not impossible.[20] As emphasized in the previous section, without knowing the band edge energies, the ΔG_{CT} remains uncertain. Finally, 2D semiconductor band edges shift dynamically when charge carrier concentration changes.[21–23] This so-called Band Gap Renormalization further complicates the measurement of band gap energies, but at the same time, it may be exploited to tune an electrode's band edge to the precise energy desired. Regardless, the classic energy level description of bulk semiconductors inadequately explains what is experimentally observed at the 2D semiconductor-liquid interface. Knowing the band edge energy positions informs what solar energy driven reactions are possible and how fast they can go.

1.4 Project Summary

This research project investigates the 2D semiconducting material, molybdenum disulfide (MoS_2), for an electrochemical and optical study. The 1-2 eV band gap of MoS_2 overlaps well with solar radiation spectrum, but importantly it also serves as a representative 2D Transition Metal Dichalcogenide (TMD) semiconductor that is promising in a variety of solar energy conversion applications.[24–26] MoS_2 has the potential to be cheap, energetically efficient, and massively scalable.[16]

The general approach is to deposit MoS_2 onto substrates in monolayer or few atomic layer "flakes" inside a transparent electrochemical cell. We measure *in situ* optical and electrochemical changes to incident light and applied potential bias (voltage). Importantly, flake heterogeneity may spatially influence charge transfer and redox reactions, so both naturally-procured and synthetically-grown crystals are first studied. We characterize the atomically thin semiconducting material and measure band gap energies using optical techniques. Using electrochemical microscopy with spectroscopic techniques, material-dependent band energies are quantified with spatially correlated images.

The project is organized along three chronological efforts corresponding to the three subsequent chapters: (1) determine the potential window in which exfoliated MoS_2 flakes are stable for certain electrochemical conditions; (2) in conjunction with a many-body theoretical model, determine the electron density and electronic band gap energies for ML-MoS_2 under electrostatic gating; and (3) determine how a redox environment (i.e. molecular or chemical dopants) can control the electronic and optical properties of ML-MoS_2 in the same system.

CHAPTER 2: BACKGROUND

The purpose of this chapter is to establish a scientific footing for the results presented hereafter. The experimental work in this thesis advances the progress of several key studies involving bulk semiconductors, 2D materials, and more specifically MoS_2. The primary goal is to develop an all-optical experimental approach to answer questions involving a 2D semiconductor under electrochemical conditions. Therefore, it is critical to lay out the well-established scientific foundation across several fields preceding this work. The highlighted studies chronicle incremental progress. Importantly, the historical examples are not necessarily scientific leaps forward, but rather these examples are critical steppingstones that logically lead to the present work. For clarity, this chapter is organized into three sections focused on the following areas: (1) photoelectrochemistry, (2) MoS_2 properties, and (3) *in situ* optical measurement techniques. After establishing this context, this chapter concludes with a final section addressing the unanswered questions that form the basis for several hypotheses.

2.1 Semiconductor Photoelectrochemistry Advances

For additional background on semiconductor photoelectrochemistry, the reader is referred to several excellent reviews, book chapters, and key manuscripts.[4,5,27–29] Importantly, these references only consider bulk semiconductor behavior. Unique consequences of semiconductors on the 2D scale are addressed later in Section 2.2.3. This section briefly describes key terms and basic principles necessary for the experimental work in Chapters 3 – 5. Throughout this chapter, the example semiconductor is n-type, so the majority carriers are electrons. When charge carrier transfer is discussed, it will be in the context of electron transfer from the semiconductor CB edge into the liquid solution. Identical and opposite schemes occur for p-type materials with holes transferring at the VB edge.

Energy scales for the figures are shown relative to the vacuum energy level where the highest value terminates with 0 eV, and an electron is at a lower energy in the 'down' direction or more positive potential. For reference, 0 V on the Normal Hydrogen Electrode (NHE) scale corresponds to 4.5 V on the absolute scale.[10,28] The related electrochemical scale is based on relative potentials where a more negative potentials are higher on this scale. Therefore, the corresponding Fermi energy of a NHE at 0 V is −4.5 eV. The relative energy (eV) and potential (V) scales are interchangeable when considering the elementary charge of an electron (q) is ~ 1.602×10^{-19} C (i.e. $E = q\mathrm{V}$). A final clarifying point: the italicized E (units of voltage versus a reference) is differentiated from the absolute energy scale with an unitalicized E (units of eV).

2.1.1 Semiconductor-Liquid Interface Description

When a semiconductor is immersed in a liquid, a spontaneous charge transfer occurs instantly across the interface. The importance of this phenomenon cannot be overstated, and it occurs between any junction so long as the semiconductor's chemical potential (Fermi level, $\mathrm{E_F}$) is not equivalent to the chemical potential of the liquid solution ($\mathrm{E_{soln}}$). Fig. 2.1A below shows an example energy profile of the interface with a bulk semiconductor and liquid colored in grey and blue, respectively. The electron transfer continues until equilibrium is reached with $\mathrm{E_F} = \mathrm{E_{soln}}$. The electron transfer process is similar to the solid-state junction between p and n-type semiconductors. With regards to charge separation, the semiconductor-liquid junction forms a strong, spontaneous electric field. This electric field forms in the absence of light, and the field strength can exceed 100,000 V/cm.[4,30] Importantly, the electric field comes at no cost. The magnitude of the field strength influences the acceleration of charges through the semiconductor. Charge separation time can be on the order of picoseconds when considering micrometer distances.[31]

The classic model for the semiconductor-liquid interface is referred to as the "Gerischer Model". Several key results of this model are noted. First, as shown in Fig. 2.1B, a positively charged depletion region forms within the semiconductor, and the liquid side of the interface is negatively charged. The depletion width can be thought of as the distance from which electrons are extracted from within the semiconductor. The depletion width varies but is often on the micrometer scale.[4]

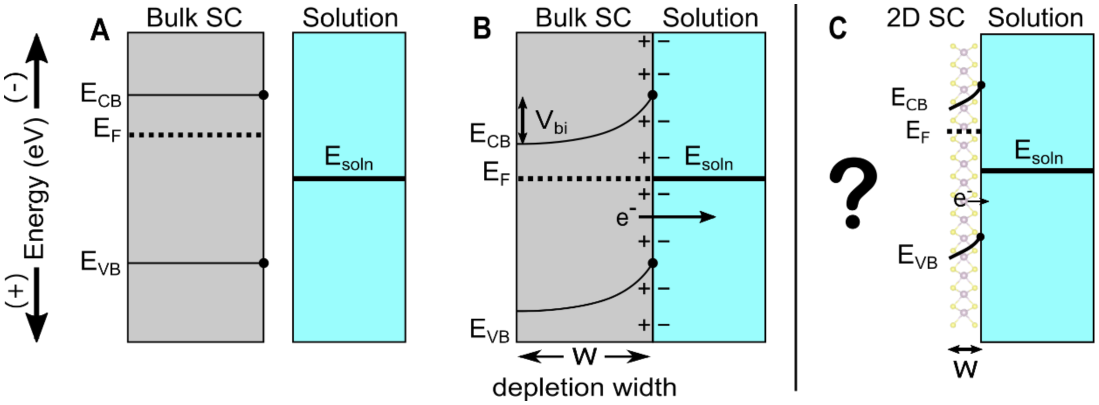

Fig. 2.1 - Energy Band Model for the Semiconductor-Liquid Interface. **(A)** Relative energies of a bulk semiconductor and solution before contact. **(B)** Classic equilibrium interfacial energy model proposed by Gerischer[32]. In this example, the Fermi level (E_F) of the semiconductor is higher than the electrochemical potential of the liquid (E_{soln}), so electrons flow out of the semiconductor. **(C)** The interface between a 2D semiconductor and a solution is unclear because of the quantized energy states and reduced thickness of the semiconductor.

Second, as Fig. 2.1B also shows, the curved lines trace the "band bending" of the CB and VB edges. The electric field is strongest at the exact interface and decreases with distance from the interface. This field is critical for separating photogenerated electrons and holes. Importantly, the built-in potential (V_{bi}) equals the magnitude of band bending (qV), and is solely the result of the differences in E_F and E_{soln} before the semiconductor contacts the liquid (see Fig. 1.2). Third, if the semiconductor electrode is controlled by a potentiostat (i.e., electrostatically gated such as with a field effect transistor), an applied potential will perturb the system from equilibrium.[17] For example, a positive (reverse) bias shifts E_F downward and net electron flow occurs into the semiconductor. Conversely, a negative (forward) bias shifts E_F upward and net electron flow occurs into the liquid. In this way, the positive bias electronically dopes the semiconductor and increases band bending. Experimentally, this "electrostatic gating" is how electron density is modulated in the experimental work in Chapters 3 – 4.

An important consequence of the Gerischer model is the relationship between the formal potential of a redox couple $E^{0\prime}(\mathrm{A/A^-})$ and the conduction band edge energy (E_{CB}). The free energy of interfacial charge transfer is given by:

$$\Delta G^{0\prime} = E_{\mathrm{CB}} - qE^{0\prime}(\mathrm{A/A^-}). \qquad (2.1)$$

Here, A and A^- are the respective electron acceptor and donor species of a reversible redox couple.[4] An electrolyte solution with more negative electrochemical potential will tend to donate electrons to the electrode and vice versa. Therefore, thermodynamic information is attained if E_{CB} is measured as a function of the potential of a known redox environment. For example, two stable redox couples with known formal potentials can bracket the CB edge of the semiconductor electrode if one couple drives an anodic current and the other couple drives a cathodic current.

Another step forward in using layered TMD semiconductors was the work by Parkinson and Spitler who used mechanical exfoliation to make electrodes with remarkable dye-enhanced efficiency.[33] Crucially, TMDs appeared to be relatively unreactive on their basal surface with minimal surface recombination. Thus, TMDs were a promising electrode from an electron transfer perspective; however, at that time there was no practical way to make a monolayer electrode.

Lastly, it is important to recognize the Gerischer model assumes ideal behavior when a semiconductor contacts a liquid. Bard and Wrighton applied the concept of "Fermi Level Pinning" to explain why experimental results from semiconductor-liquid interfaces did not fit the Gerischer model. They pointed out that charge impurities or surface states cause experimentally observed Fermi level pinning.[34] Furthermore, the Gerischer model assumes semiconductor and liquid thicknesses (i.e. "bulk" depth) are sufficiently large to accommodate charge transfer from spontaneous equilibration between the phases.

2.1.2 Thermodynamic Stability of the Semiconductor

In the early exploration of efficient solar conversion semiconductor electrodes, scientists realized a trade-off between electron transfer efficiency and chemical stability. Specifically, a wide-bandgap oxide semiconductor like TiO_2 is rugged in aqueous electrolytes, but not efficient because much of the solar emission does have enough energy to meet its band gap. On the other hand, a highly efficient , narrow-gap electrode more readily corrodes from photo-generated charge carriers. In the late 1970's, Bard and Wrighton integrated this consideration into the Gerischer model, and they came to the conclusion that avoiding corrosion and using a PEC to convert solar energy remained feasible.[35] However, the effect of photoanodic dissolution (i.e. corrosion) reduced the energetic operating range of the semiconductor electrode and therefore reduced its maximum efficiency. Light impinging on the semiconductor generates holes and electrons, and the holes will decompose the semiconductor unless the electrolyte offers a more energetically favorable species to oxidize. Now the problem became finding a semiconductor that was stable in the electrolyte yet efficient enough to catalyze electron transfer without decomposing in the process. A decade later there was a brief attempt and minimal success in mitigating the corrosion complication by adding sulfide and selenide salts to the electrolyte in an attempt to suppress photoanodic decomposition.[36] However, a similar earlier approach led by Tributsch attempted using iodide ions to scavenge the holes, but this work used n-type crystals of Transition Metal Dichalcogenides (TMDs).[8,37,38] Tributsch recognized the unique d-orbital character of both the VB and CB did not decompose the semiconductor bonds like others with p-orbital character VB molecular orbitals.[39] At this time, the crystal semiconductors were on the micrometer thickness scale, and 2D electrodes did not exist.

2.2 Properties of MoS_2

2.2.1 Bulk Physical and Optical Properties

A century ago, Linus Pauling first described the hexagonal crystal structure of MoS_2 using X-ray spectra.[40] In the 1960 and 1970's, significant research at the University of Cambridge began to elucidate more physical, optical, and electronic properties of thin crystals of MoS_2. In terms of physical structure, the layers of MoS_2 are bound by relatively weak van der Waals forces, so that the sheets exfoliate relatively easily. In fact, early researchers cleaved samples down to less than 100 nanometer thickness using simple adhesive tape.[41] The stacked hexagonal atomic structure is seen in Fig. 2.2.

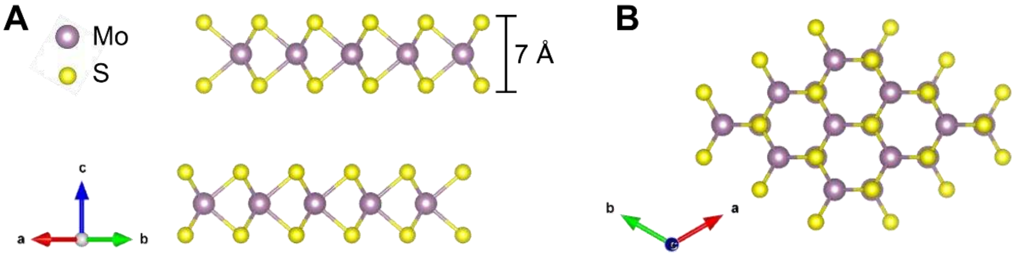

Fig. 2.2 – MoS_2 Crystal Structure. Each 3-atom thick layer is 7 Å with A-B-A repeating pattern. The basal surfaces (perpendicular to the c-axis) are formed from a layer of sulfur atoms. Each molybdenum atom forms a trigonal prismatic point group symmetry, and overall ML-MoS_2 crystal has D_{3d} symmetry.[42]

Using remarkable electron diffraction, absorbance, and reflectance data, bulk MoS_2 was well characterized decades ago. Frindt, Yoffe, and Wilson determined the layer-dependent changes in the properties of MoS_2 and assigned the prominent absorbance peaks correctly as exciton transitions.[41,43] An exciton is an electron-hole pair bound by Coulombic forces. Excitons are known to be photogenerated in semiconductors and recombination of these charge carriers also results in photoemission (i.e., photoluminescence). It is important to recognize that the exciton transition energy is not equivalent to the electronic band gap energy (E_g). The difference in E_g and exciton energy is the binding energy (E_b) associated with the bound state. For this reason, the exciton transition is associated with the optical band gap energy (E_{opt}). Thus, $E_g = E_{opt} + E_b$.

2.2.2 Electronic Properties and Band Energetics

Original attempts to describe the electronic band structure of MoS_2 came from limited spectroscopic data, though excitons were correctly assigned band gap transitions.[44] Mattheiss calculated a robust band structure from an early Muffin Tin and Tight-Binding computational approach, and this confirmed experimental data of the band gap transitions.[45] The calculated electronic band gap transitions range from 1.2 to 1.3 eV for bulk MoS_2. Later, Tributsch proposed MoS_2 as a candidate electrode for solar powered water splitting because of this energy band structure.[8,39] Specifically, Tributsch noted that the 1.75 eV optical band gap (i.e. exciton transition) was a direct transition that did not break any MoS_2 chemical bonds, and the formal potential ($E^{0\prime}$) of several common redox couples are situated within or near the band edge energies of MoS_2.

An important discovery occurred in 2007 when Galli used first principle theoretical work to explain interesting experimental spectroscopic data of MoS_2 nanoparticles.[46,47] Galli noted that the electronic band gap was uniquely symmetry-allowed for ML-MoS_2, and the band structure changed significantly in few-layer structures. For example, the classic bulk MoS_2 band gap of 1.3 eV increased abruptly to 1.8 eV as the material thinned to a single layer.

2.2.3 Consequences of Reduced Dimensionality

The work of Galli ignited a research effort in using TMDs and other types of 2D semiconductors. Around this time in early 2000's, graphene was the most prominent 2D material. Regardless of its layer thickness, graphene's semimetal properties did not provide utility for many electronic and energy conversion applications.[48] The direct bandgap TMD semiconductor more readily absorbs light exceeding its bandgap. With this prospect, research in MoS_2 and other layered semiconductors exploded.

One major consequence of ML-MoS_2 having a direct band gap is that absorbance and photoemission process is more efficient than indirect transitions. This explained the significant intensity increase in photoluminescence emission for monolayer crystals compared to two or more layers. In 2015, a defect-mediated monolayer MoS_2 photoluminescence quantum yield exceeding 95% was measured owing to the near-perfect optical properties of the pristine crystal. At that time the typical experimental PL quantum yield for TMDs was less than 1%.[49–51] This study showed how photoexcited lifetimes of the material could extend to tens of nanoseconds and also how excitons are strongly influenced by electron concentration. Importantly, sulfur vacancies in the crystal arose as the defect culprit that provided the unwanted recombination sites for exciton recombination. By shielding or repairing the defects with a chemical treatment (nonoxidizing superacid), defects were passivated or repaired. In addition to PL, Raman spectroscopy is often used to characterize the layer thickness of few-layer TMDs because of a peak splitting of two prominent E_{2g} and A_{1g} lattice vibrations.[42,52,53] For example, the difference in peak splitting between monolayer and bilayer MoS_2 is 2-3 cm^{-1}.[54]

A final consideration of reduced dimensionality is the impact on electrode design and engineering. To maximize the surface area to volume ratio, a monolayer material is ideal. The semiconductor interface is necessary to capture light and catalyze electron transfer to the liquid. Also, the penetration depth of photons into the material exceeds its thickness. This highlights another bizarre phenomenon when the semiconductor is reduced to a 2D crystal. From a design perspective, excess material is wasteful. Bulk semiconductors electrodes that are thicker than the penetration depth of light do not add any benefit to electron transfer processes occurring at the surface.[55]

2.2.4 Room Temperature Trion

A trion is another strongly bound quasiparticle observed 2D semiconductors. A trion is a bound state consisting of three charged particles, so it is either two electrons and a hole or two holes and an electron. The first reported observations of room temperature trions in MoS_2 in 2013 by Heinz and coworkers also showed that electrostatic gating modulated spectral intensities between the exciton and trion.[56] In other words, trion formation monotonically reduces excitons and vice versa. In n-type MoS_2 the majority carrier electrons means that trions arise when a second electron binds to an exciton. The trion binding energy is an order of magnitude smaller than the exciton binding energy – tens of meV versus hundreds of meV.[56–59] This also means that the trion absorbance/emission energy is necessarily slightly less than the associated exciton.

2.3 *In Situ* Optical Measurements of MoS_2 Under Electrochemical Conditions

Two important experimental steps led directly to the research approach of this project. First, in 2016, Castellanos-Gomez and others developed a simple optical approach to measure the absorbance of mechanically exfoliated MoS_2 flakes using a novel hyperspectral microscopy imaging technique.[60] This work included absorbance measurements of MoS_2 down to monolayer thickness. Second, in 2019 a team at National Renewable Energy Laboratory (Carroll, et. al.) published a report of few layer MoS_2 absorbance under electrochemical conditions. Unlike classic semiconductors, their experimental observations indicated that interfacial energetics of the MoS_2 varied with electrostatic fields.

2.3.1 Hyperspectral Microscopy Imaging

Using a sensitive camera and a narrow bandwidth light source spectrum, Castellanos-Gomez measured absorbance of MoS_2 under an optical microscope. The spectrum from our work matches that of Castellanos-Gomez's as shown in Fig. 2.3A below. Here, we spatially correlate absorbance measurements from transmission images of synthetically-grown MoS_2 on a transparent substrate. While fixing the field of view and varying the incident light source, the camera simultaneously captures a transmission image including a region of MoS_2 and a region of blank substrate. Assuming light attenuation is dominated by absorbance, the transmission intensities follow the Beer-Lambert relationship:

$$A(\lambda) = \log_{10}\left(\frac{I_0(\lambda)}{I(\lambda)}\right) \qquad (2.2)$$

where $A(\lambda)$ is the wavelength dependent absorbance and I_0 and I are the transmission intensities within the background and MoS_2 sample regions, respectively. Note this approach is advantageous to preferentially select pristine sample regions instead of most previous studies that relied on larger sample regions with more sample heterogeneity. For the first time, individual layers of MoS_2 were differentiated using this hyperspectral microscopy technique. This approach also works well to spatially correlate absorbance with other techniques such as Raman and photoluminescence spectroscopy that can also be used to characterize layer thickness of MoS_2.

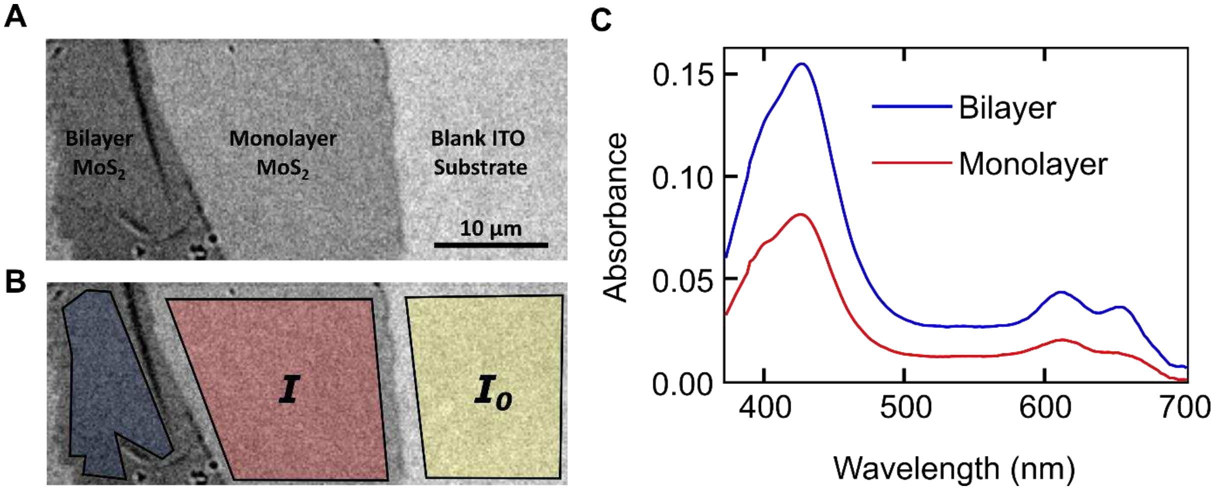

Fig. 2.3 – Example MoS_2 Absorbance Measurement from Transmission Images. **(A)** White lamp illuminated transmission image of monolayer and bilayer regions on ITO substrate. **(B)** Highlighted sample

regions used to measure average transmission intensity. **(C)** Spatially-correlated MoS_2 absorbance spectrum from hyperspectral images.

Fig. 2.3C shows an example absorbance spectrum in which the same images are used to compare the absorbance of monolayer (ML) and bilayer MoS_2. In both monolayer and bilayer MoS2, absorbance peaks are centered at 605 and 655 nanometer wavelengths, and these peaks correspond to the B and A exciton, respectively. The more prominent absorbance peak at ~425 nm is the C exciton. The separation between the A and B exciton peak arises because of spin-orbit split valence band. The optical contrast in the transmission images allow for discrimination of multi-layer regions, defects, and unknown particulates. Differences in the approach of Castellano-Gomez and this work include the following. First, Castellanos-Gomez used a fiber optic bundle with several bandpass filters to achieve spectral resolution of 10 nm. Second, the substrate is electrically insulating polydimethylsiloxane. Finally, all measurement occurred in air with mechanically exfoliated natural crystals.

2.3.2 Potential-Dependent Absorbance of MoS_2

Several previous studies determined the influence of electrostatic gating of MoS_2 in a field effect transistor.[56,61,62] A consistent result is that absorbance and reflectance intensity of TMD exciton peaks predictably change by injecting free carriers (electrons) into the material. The results indicated that the *optical* band gap increased under a more negative bias or n-doping (i.e. increased electron concentration); however, the *electronic* band gap must be larger than the exciton transition energy because of the remarkably large binding energy of the formed excitons.[63] A problem is that both the exciton binding energy and the electronic band gap simultaneously renormalize when a 2D semiconductor is electronically doped. The renormalization effect is similar in magnitude and offsetting, so this makes measurement of electronic band energies difficult from optical measurements alone.

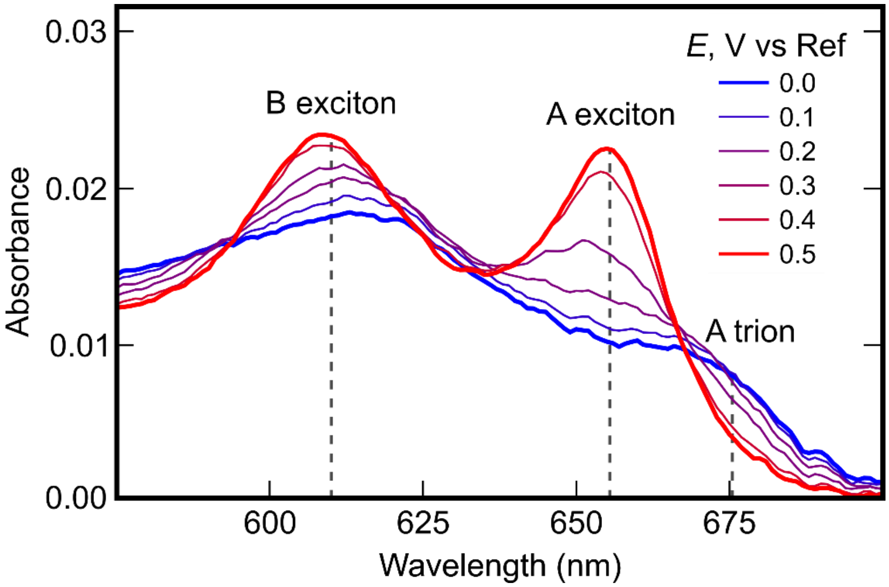

Fig. 2.4 – Potential Dependent MoS_2 Absorbance Spectrum. Key features are the bleaching of the A and B exciton peaks and emergence of A trion peak under more negative potentials. Dashed lines correspond to reported peak positions.[56] Example shown is a monolayer MoS_2 flake measured in a 0.25 M TBAPF6 / acetonitrile electrolyte. Reference versus Ag wire quasielectrode.

Differences in the approach of Carroll and this work include the following. First, absorbance from the trion resonance is not considered in the measurement. Measurement error from trion contribution would be most significant when MoS_2 is most highly doped (i.e. highest electron density at the most negative bias). Second, the samples were not strictly ML-MoS_2; the flakes size estimates ranged from 1-3 layers lateral widths less than one micrometer. The next logical step is to combine the work of Carroll with Castellanos-Gomez to spatially resolve ML regions in an electrochemical cell. Third, we identify the trion peak in an absorbance spectrum of ML-MoS_2. Fig. 2.4 shows the spectral response of an electrostatically-doped MoS_2 electrode, and a more negative applied potential increases electron density and forms additional trions. The more positive applied potentials results in a noticeable peak shoulder in the A exciton ca. 675 nm in agreement with literature.[56]

2.4 Unanswered Questions

Following the Project Summary outlined previously in Section1.4, the next several chapters address the following unanswered questions:

2.4.1 Is MoS_2 a chemically stable candidate for PEC conversion of solar energy?

Here, electrochemical stability is described primarily by the potential window (i.e. voltage range) and liquid electrolyte environment required to measure MoS_2 band energies. Photo-degradation is not specifically studied though all illumination sources will span the UV-visible spectrum and photo-excited carrier generation is briefly considered. To a lesser extent, the MoS_2 stability in various redox species may inform us of unique chemical interactions (i.e. functional groups or inner versus outer sphere electron transfer).

2.4.2 How do the band energies of ML-MoS_2 change under electrochemical conditions?

Here, we consider the electronic characteristics such as charge carrier concentration to quantify band edge energies. The key is to develop a reliable all-optical method to convert spectra into carrier density. The carrier density in this case is controlled by electrostatic gating. By doing this, we may extract *in situ* ML-MoS_2 band energetic information.

2.4.3 How does the redox environment tune the electronic properties of a ML-MoS_2?

Here, the initial hypothesis is: if redox species chemically dope MoS_2 then the optical absorbance spectrum matches that of electrostatically-gated conditions. It is unknown how a 2D material will behave given that the depletion width is less than the thickness of the material. Returning to the driving force for interfacial electron transfer: $\Delta G^{0\prime} = E_{CB} - qE^{0\prime}$ (A/A^-), the redox couple A/A^- present at the interface may control the electronic and optical properties of the ML-MoS_2. In a systematic way of varying redox species, the energetics of the material such as the flat-band potential (E_{FB}) can be bracketed on an absolute energy scale. This study provides an improved description of the semiconductor-electrolyte interface.

CHAPTER 3: ANODIC DISSOLUTION OF MOS$_2$ IN ELECTROCHEMICAL SYSTEM*

The original broad project goal of understanding MoS$_2$ energy level alignment (see Section 1.4) extended from the work of Carroll.[64] However, recent experimental observations by Merranda Schmid in the Sambur laboratory indicated that thin flakes of MoS$_2$ corroded in electrolyte under certain conditions. As detailed in Section 2.1.2, photoanodic corrosion involves the chemical dissolution of the semiconductor. Before attempting to measure band edge energies, electrode corrosion must either be controlled or avoided in our experimental setup. The research began as a control experiment to obtain the anodic potential limit of MoS$_2$. However, the optical images told an interesting story about how and where MoS$_2$ corrodes.

Mechanically exfoliated MoS$_2$ samples in this work originate from two bulk sources: natural (SPI Supplies) and synthetic (2D Semiconductors). Sample flakes of this kind had been previously characterized in Van Erdewyk's work on electronic doping heterogeneity.[65,66] This is the first time an earnest study examined the chemical stability of the material. The findings include an anodic boundary that is still well beyond the band edge of ML-MoS$_2$ and role of contaminant H_2O in accelerating the corrosion rate. Therefore, MoS$_2$ remains a viable electrode material to further study with a sufficient wide stable electrochemical potential range.

3.1 Conspectus

Electrochemical gating of 2D transition metal dichalcogenide (TMD) electrodes is an emerging frontier in the field of semiconductor electrochemistry. In this approach, an applied bias modifies the charge carrier concentration of the 2D TMD, causing band edge shifts and drastic changes in charge transfer rates. However, leveraging this affect for (photo)electrocatalysis is practically limited by the stability of the TMD material under gating conditions. Gerischer showed anodic dissolution of bulk TMD electrodes can occur

---

* This chapter is prepared as a manuscript for publication in the Journal of the Electrochemical Society. The authors' contributions are found in Appendix A – Division of Work.

in the dark and hypothesized that the reaction proceeds via an electron tunneling mechanism from surface states to the TMD conduction band.[67] Here we investigate this possibility in single MoS_2 nanoflakes using in situ optical microscopy and explore whether Gerischer's electron tunneling mechanism can explain anodic dissolution rates of thin 2D semiconductors. Spatially resolved measurements show anodic dissolution initiates at perimeter edge sites and accelerates exponentially with decreasing layer thickness, consistent with Gerischer's tunneling mechanism. Interestingly, single layer MoS_2 is impervious to anodic dissolution at applied potentials >200 mV more positive than those required to drive dissolution in bulk and multilayer-thick nanoflakes.

3.2 Introduction

Unlike bulk transition metal dichalcogenide (TMD) semiconductors (e.g., MoS_2 or WSe_2), the optical and electrochemical properties of single and few layer-thick TMDs are influenced by an applied bias.[68–71] The bias can be applied via a back gate electrode in a field effect transistor geometry[72,73] or directly to the 2D semiconductor immersed in a chemically inert electrolyte solution.[74–76] Electrochemical gating tunes the charge carrier concentration in two-dimensional (2D) semiconductors and drastically shifts its band edge energies.[77,78] Frisbie et. al. studied the electrochemical properties of 5 nm ZnO and monolayer MoS_2 in a field effect transistor geometry.[72,79] In the MoS_2 system, the applied bias to the back gate reduced the overpotential for electrocatalytic hydrogen evolution.[80] Further, electrochemical gating of MoS_2 and ZnO modulated electron transfer rates of ferrocene and 2,3,5,6 tetrabromo-1,4-benzoquinone by 250 and 20-fold, respectively.[79,81] In summary, tuning thermodynamic properties and reaction kinetics of 2D semiconductors via electrochemical gating is an emerging frontier in 2D semiconductor electrochemistry.

One practical limitation of electrochemical gating is the stability of the semiconductor under gating conditions. Bulk TMDs are remarkably stable electrode materials over a wide potential range under dark and illumination conditions because nonbonding and antibonding metal d orbitals comprise their valence and conduction band edges.[8,82,83] However, anodic dissolution occurs at sufficiently positive potentials. Bulk MoS_2 undergoes anodic dissolution at +0.7 V vs Ag/AgCl in aqueous electrolyte.[84–86] Carroll et al.

recently studied how the optical and electrochemical properties of single and few layer-thick MoS_2 electrodes change over a −2.0 to +2.0 V (vs Ag) range in dry, anerobic 0.1M tetrabutylammonium hexafluorophosphate ($TBAPF_6$)/acetonitrile electrolyte. The authors did not report MoS_2 decomposition under rigorous air-free and non-aqueous conditions.[77] In this study, we explore the 2D semiconductor stability in the same acetonitrile electrolyte under N_2-saturated conditions.

Anodic dissolution of TMD semiconductors can occur under dark and light conditions.[35,39,87] In the dark, Gerischer et al. showed $MoSe_2$ undergoes anodic dissolution at positive bias in aqueous electrolytes.[67] Alternatively, photo-generated holes can also drive anodic dissolution.[35,67,88] In fact, Tenne and Wold leveraged photoanodic etching to remove surface recombination centers on bulk WSe_2 electrodes, producing high efficiency (>14%) photoelectrochemical solar cells.[7] Gerischer proposed the following corrosion reaction mechanisms under dark (Eqn. 3.1) and light (Eqn. 3.2) conditions by comparing the charge passed during the reaction with the products detected by spectrophotometric analyses:

$$MX_2 + 11H_2O \rightarrow MO_3{\cdot}xH_2O + 2XO_4^{2-} + 22H^+ + 18e^- \qquad (3.1)$$

$$MX_2 + 9H_2O + 14h^+ \rightarrow MO_3{\cdot}xH_2O + XO_3^{2-} + 18H^+ \qquad (3.2)$$

where M is the metal such as Mo or W and X = the chalcogen atom such as Se or S.[67] Gerischer claimed that the anodic reaction under illumination can be driven by valence band holes (h^+) according to Eqn. 3.2. Under dark conditions, VB holes are unavailable to drive the anodic reaction. Instead, anodic dissolution occurs when electrons tunnel into the conduction band (CB) from mid-gap surface states (Eqn. 3.1). This mechanistic hypothesis suggested that anodic dissolution under dark conditions is highly localized compared to illumination conditions because the dark reactions initiate at high energy surface states associated with crystal defect sites. Indeed, qualitative photographic analyses of bulk crystals after polarization at positive bias showed that anodic dissolution occurred at very restricted sample locations.[67] Numerous studies of anodic dissolution and electrocatalytic activity have shown that TMD crystal dislocations, kinks, and edge sites exhibit faster surface kinetics than the inert basal planes.[88–92] However, Gerischer's anodic dissolution studies of bulk crystals have not been extended to few-layer TMDs.

Given the growing interest of ultrathin 2D semiconductors for electrocatalysis and solar energy conversion applications,[71,93–96] several groups studied the chemical stability of 2D TMDs under electrochemical[84,97–99] and non-electrochemical conditions.[100–105] Multiple groups studied the chemical and/or mechanical stability of multilayer-thick MoS_2 nanoflakes under electrochemical conditions and even leveraged anodic dissolution to prepare single layer-thick samples. Feng et. al. used transmission electron microscopy (TEM) to confirm atom-by-atom dissolution of a single layer MoS_2 nanosheet under an applied bias of +0.8 V in aqueous buffer (1M KCl, pH 7.4).[106] Liu et. al. showed that bulk MoS_2 crystals could be exfoliated to single layer or few layer-thick nanoflakes by applying a DC bias up to +10 V in 0.5 M aqueous Na_2SO_4 electrolyte.[107,108] Das et. al. extended this novel top-down electrochemical technique to TMD flakes on conductive substrates.[109–113] Those authors determined the "electro-ablation" (EA) onset potential of mechanically exfoliated TMD nanoflakes in a electrochemical cells. By monitoring micro-reflectance spectra of the nanoflakes, they determined the onset potential for MoS_2 EA in 1M LiCl aqueous electrolyte solution is ca. +0.75 V (vs Ag/AgCl).[111] However, the anodic dissolution kinetics as a function of nanoflake layer thickness remains unknown.

Our work investigates several open questions regarding the anodic dissolution of TMD nanoflakes. First, how does the dissolution onset potential (E_D) vary from nanoflake to nanoflake? Second, does dissolution preferentially occur at the step edge sites on the basal plane surface, resulting in top-down pitting, or at the perimeter edge sites? Finally, how does the anodic dissolution rate scale with layer thickness? Here we use single nanoflake-level optical density measurements in a working electrochemical cell to study the onset potential and spatially resolve the anodic dissolution of mechanically exfoliated MoS_2 nanoflakes in 0.25 M $TBAPF_6$/acetonitrile. Control experiments in the presence of 0.5 mM water confirm the reaction likely proceeds via Eqn. 3.1. We observe a narrow distribution (±25 mV, $N = 20$ nanoflakes) in the onset potential suggesting E_D is a thermodynamic barrier for the material. Interestingly, at applied potentials beyond E_D, the dissolution rate increases exponentially with decreasing layer thickness. Finally, monolayer MoS_2 nanoflakes and pure monolayer MoS_2 films grown by chemical vapor deposition (CVD) are impervious to anodic dissolution (even in the presence of water), despite the fact that thicker nanoflakes located just a few microns away undergo anodic dissolution under the same conditions. Amazingly, monolayer MoS_2 can remain intact after several days of electrostatic gating +200 mV above the E_D value of multilayer-thick MoS_2.

3.3 Methods

3.3.1 Electrochemical Flow Cell Preparation

The custom flow cell preparation is generally detailed in previous work.[99] The MoS_2 material originated from one of three sources: (1) commercially synthesized bulk MoS_2 crystals (Re-doped n-type, 2D semiconductors, BLKMoS$_2$-N, doping density 10^{17}-10^{18} cm^{-3}), (2) naturally occurring bulk MoS_2 (SPI, 470MOS2LAB), and (3) MOCVD synthetically grown monolayer sheets(see Section 4.3.1 for additional details). The bulk crystals were manually exfoliated using low residue Nitto tape (BT-150E-CM, Nitto) and was manually pressed onto the surface of bulk crystals, removed, and then folded 2-3 times to thin the flakes. A commercially available gel-film (Gelfilm from Gelpak) was used to transfer exfoliated MoS_2 from the Nitto tape to a pre-cleaned ITO electrode (4-10 Ω, 25 × 75 × 1.1 mm, Delta Technologies). The ITO cleaning procedure is provided in a previous study.[114] The nanoflake-coated ITO electrodes were

assembled into a 3-electrode electrochemical flow cell as described previously.[99] The typical lateral size of mechanically exfoliated MoS_2 flakes was 10-150 μm (see Fig. B.2A-C for example transmission images). Based on correlated profilometry and optical absorbance measurements (Fig. B.3), the thickness of the examined flakes range from monolayer to approximately 150 layers (0.7 Å to ~100 nm). The total volume of electrolyte in the cell is 10-80 μL, estimated from the average surface exposed ITO and height of a Teflon spacer. A steady flow of electrolyte reduced potential drift in the Ag wire quasi-reference. Pt (99.9%, Thermo Fisher Sci.) and Ag (99.%, Alfa Aesar) wire served as the working and quasi-reference electrodes, respectively. Both wires were approximately 0.5 mm in diameter and 3.5 cm in length (70 μm^2 surface area). Electrode wires were secured inside the electrolyte reservoir by drilling small holes and applying epoxy (Loctite E-120HP) to create an air-tight seal. An Ivium Compactstat potentiostat applied a constant potential to the ITO/MoS_2 working electrode for the duration of each corrosion or spectral measurement. All corrosion rate image data was averaged over 1 hour with a frame rate of 0.1 Hz. The observed open circuit potential of the electrolyte-filled cell was +0.3 V vs Ag wire quasi-reference electrode.

3.3.2 Nanoflake Thickness Determination

The nanoflake thickness was determined using a calibration curve that relates optical density (OD) values to the height profile of a single nanoflake (Fig. B.3). To do so, we obtained bright field transmission images of single nanoflakes and calculated OD =log(I/I_0), where I is the light transmitted through basal MoS_2 region and I_0 is the light transmitted through the adjacent background region. Next, we measured the height profile of the same single nanoflake with profilometry (Dektak XT, 12.5 μm stylus). We fit the OD versus height profile data to an empirical power function (OD) = $A(t)^B + C$, where t is thickness, and A, B and C are fit parameters. We could not resolve single layer MoS_2 with profilometry or MoS_2 step edges less than 5 nm due to the surface roughness of the ITO substrate and the limitations of the instrument. Instead, Raman micro-spectroscopy and OD measurements confirmed the layer thickness for MoS_2 material less than five layers thick. Additional details are found in the Supplementary Material (Determining Nanoflake Thickness).

3.3.3 Edge Dissolution Rate Determination

We quantified the anodic dissolution rate of single nanoflakes by monitoring how the total area and nanoflake edge boundary changed with time and potential. The procedure is described in the Results section and graphically illustrated in Fig. 3.1 and Fig. 3.2. Briefly, we threshold each image by intensity to distinguish the pixels belonging to the MoS_2 nanoflakes and the ITO substrate (i.e., background pixels). Then, we determined the contiguous nanoflake boundary using the edge function with Canny method[115] in MATLAB. A custom MATLAB script calculated the distance between all edge pixels of the first image to the nearest neighbor edge pixel in the final image of the movie. We define the lateral anodic dissolution rate (*L*, μm/hr) as the average value for all edge pixels within one potential step (Fig. B.4). Supplementary Material (Transmission Image Processing) provides further experimental details and imaging procedures.

3.4 Results

We exfoliated MoS_2 nanoflakes from either naturally occurring or synthetic MoS_2 crystals and transferred the nanoflakes to an ITO substrate. We chose to study both naturally occurring and synthetic crystals because our previous photoelectrochemical microscopy study[116] revealed hidden p-type domains in nominally n-type samples and, therefore, we wanted to explore how this doping heterogeneity might influence the anodic dissolution process. The mechanical exfoliation procedure produces a heterogeneous population of nanoflakes, allowing us to correlate anodic dissolution kinetics and physical properties (e.g., thickness, area, and perimeter edge length) at the single nanoflake-level.

Fig. 3.1A shows the experimental setup and brightfield imaging approach. The MoS_2 nanoflake-coated ITO electrode serves as the working electrode in a 3-electrode electrochemical flow cell that is mounted on the stage of an inverted optical microscope. In a typical experiment, a potentiostat applies a potential step waveform from 0.00 V to +1.70 V in 50 or 100 mV/hr increments (Fig. 3.1C). At the same time, a white light lamp illuminates a microscopic region of the sample in Kohler illumination mode and a 60× objective collects the light transmitted through the sample and projects the photons onto a sCMOS camera (Fig. 3.1B). We observe no photocurrent under these low-light conditions. The camera collects 360 images per potential step (0.1 Hz image sample rate). We also acquire images of other nanoflakes in the cell before and after each potential step by traversing the microscope stage to pre-defined positions. This procedure allowed us to amass statistics from over 20 individual nanoflakes.

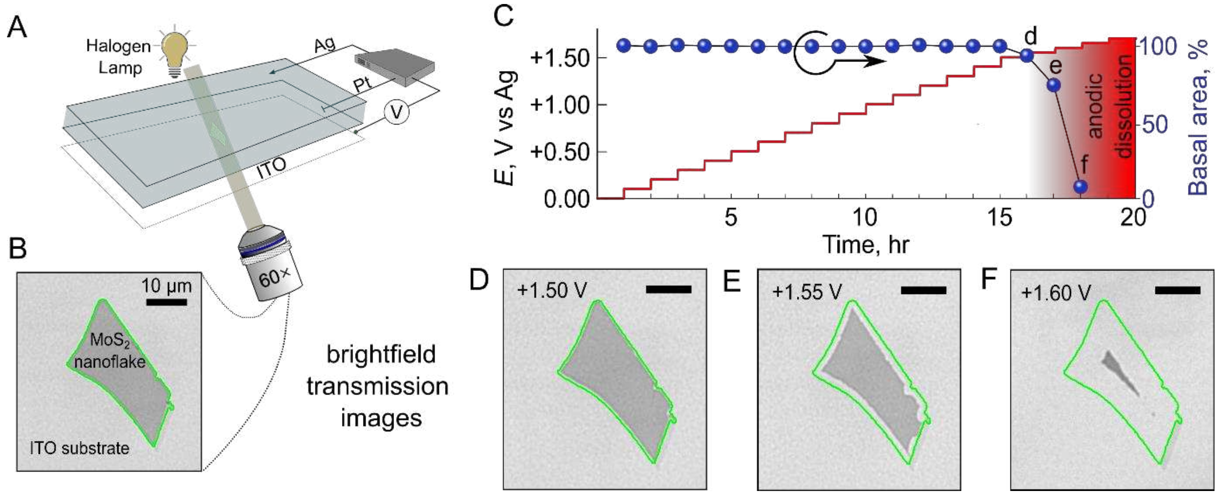

Fig. 3.1 Experimental setup. **(A)** Brightfield imaging approach to quantify anodic dissolution rates of MoS_2 nanoflakes. A white light source illuminates a microscopic region of the sample and a sCMOS camera detects photons transmitted through the MoS_2 sample and ITO substrate. **(B)** Initial transmission image of a representative nanoflake inside the electrochemical cell. **(C)** Example of the potential step waveform applied to the working electrode (0.00 V to +1.70 V vs Ag QRE). The blue data points represent the relative change in the basal surface area for the synthetic nanoflake in (B). **(D-F)** Transmission images of the same nanoflake acquired at the end of each applied potential step. Scale bars are 10 µm. The solid green line shows the initial nanoflake boundary.

Fig. 3.1B shows a representative brightfield transmission image of a single nanoflake exfoliated from a synthetic crystal at the start of the experiment, before the potentiostat applies the waveform. The nanoflake appears as a dark object against a bright background in this imaging mode because the nanoflake absorbs and scatters light. The green contour line in Fig. 3.1B indicates the nanoflake boundary, as determined by the built-in edge detection image processing algorithm in MATLAB (see Supplementary Material (Transmission Image Processing)). Upon applying increasingly positive potentials, we observe anodic dissolution along perimeter edge sites, as evidenced by decreased contrast near the nanoflake contour (Fig. 3.1D-F). Control experiments with the electrolyte solution spiked with H_2O (0.5 mM) show the dissolution rate accelerates at the nanoflake contour, suggesting the reaction mechanism proceeds via Eqn. 3.1 (Fig. B.5). Over time, this anodic dissolution process reduces the nanoflake basal surface area as the edge boundary recedes for $E \geq +1.50$ V vs Ag QRE. Fig. 3.1C shows the percentage of MoS_2 basal surface area relative to the initial area as a function of applied potential. The basal plane area rapidly decreases with increasing positive potentials as the nanoflake undergoes anodic dissolution (Fig. 3.1C). Separately, we calculate the nanoflake thickness in each frame from OD measurements using a calibration curve established by ex situ profilometry measurements. The OD of the nanoflake interior remains constant despite the shrinking edge contour (Fig. B.6), and this indicates the dissolution process occurs parallel to the MoS_2 layers and not perpendicular to the layers (i.e., anodic dissolution is kinetically anisotropic). In the naturally occurring crystals, we observed more prevalent interior pitting and cracking at interior defects (see Fig. B.7), in agreement with literature.[117] This pitting dissolution behavior observed for the naturally occurring samples could be due to the aforementioned n- and p-type doping heterogeneity induced by varying Mo:S ratio across the sample,[116,118–120] or from a higher local density of defects such as crystal dislocations and kinks.[87,121]

We developed an image analysis algorithm to quantify the anodic dissolution kinetics of single MoS_2 nanoflakes. The Supplementary Material (Transmission Image Processing) provides step-by-step details. Here we provide an overview of the image analysis procedure and how we quantify the edge corrosion rate (L, in units of μm/hr) for many individual nanoflakes. Fig. 3.2A-inset schematically illustrates how we quantify L. First, we determine the nanoflake contour with the edge function in MATLAB. The solid black line in Fig. 3.2A-inset represents the nanoflake contour after the first one-hour potential step at $E = 0.00$ V. Next, we incrementally step the potential to more positive values and evaluate the nanoflake contour at the end of the potential step. The initial potential step increment (ΔE) in the positive potential regime is 100 mV. We reduced this interval to 50 mV for $E > +1.50$ V to better resolve the accelerating edge dissolution reaction. Having determined all edge boundary pixels for the sequential experiments, we calculate a distance vector between each initial contour pixel and the nearest pixel neighbor for the following potential step contour (see Supplementary Material for details). Fig. B.4 shows an example of the distribution of pixel distance vectors after several potential steps. Finally, we determine L for each one-hour potential step experiment by averaging all vector lengths and converting to units of μm/hr.

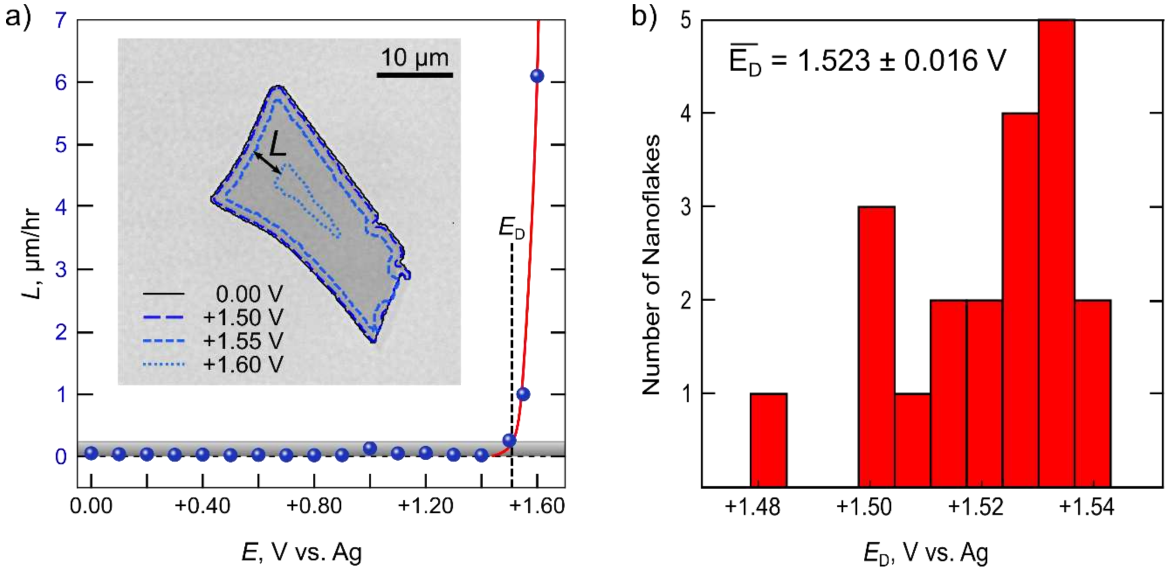

Fig. 3.2 Quantifying anodic dissolution kinetics and the dissolution potential E_{D}. (A) Edge corrosion rate (L) versus applied potential (E) for the single nanoflake shown in Figure 1b. The inset image shows a representative L vector for the corrosion rate between +1.55 V and +1.60 V for a single edge contour pixel. The blue data points in the main panel represent the average L value for all contour edge pixels (see Fig. B.4 for details). The solid red line represents a fit to the data using an exponential rise function ($L = \alpha e^{\beta E}$). The grey shaded region indicates the L value threshold for anodic dissolution. The vertical dashed line represents E_{D}, see main text for details. **(B)** Distribution of E_{D} values for 20 individual MoS_2 nanoflakes.

Anodic dissolution accelerates rapidly with increasingly positive potentials (Fig. 3.2A). To quantify how the dissolution rate accelerates with E for each nanoflake, we fit L versus E data with an exponential rise function, $L = \alpha \exp^{\beta E}$, where α is the amplitude and β describes acceleration of the linear edge corrosion rate with increasing positive potentials. We define the onset potential for anodic dissolution (E_{D}) as the E value where L exceeds a background threshold value, μ + 3SD, where μ is the average L value over the electrochemically stable range of E = 0.00 V to +1.00 V. The standard deviation of L for the nanoflake in Fig. 3.2A is 0.067 μm/hr.

The average anodic dissolution potential of 20 nanoflakes is +1.523 ± 0.016 V vs Ag QRE (Fig. 3.2B), corresponding to +1.473 ±0.016 V vs a commercial 0.01M Ag/$AgNO_3$ reference electrode. We observed no clear correlation between E_{D} and nanoflake physical properties such as thickness, perimeter length, basal plane area, or initial edge density (perimeter length divided by the area, see Fig. B.8). The lack of correlation between E_{D} and nanoflake characteristics, as well as the narrow E_{D} distribution, suggest that the onset potential for anodic dissolution reflects a thermodynamic quantity of the system and is not dominated by kinetic effects.

Interestingly, we observed a strong correlation between nanoflake thickness and the potential-dependent dissolution rate, parameterized by the fit parameter *β*. Fig. 3.3B shows representative anodic dissolution kinetics versus layer thickness for a nanoflake with monolayer (1L), bilayer (2L), and multi-layer-thick domains. Under equivalent electrochemical conditions, *L* accelerates more with increasing positive bias as the layer thickness decreases. Fig. 3.3B shows *β* scales exponentially with layer thickness for 20 nanoflakes. Our results reveal similar thickness-dependent dissolution rates for both natural (SPI Supplies, blue squares) and synthetic (2D Semiconductor, black circles) MoS_2 crystals.

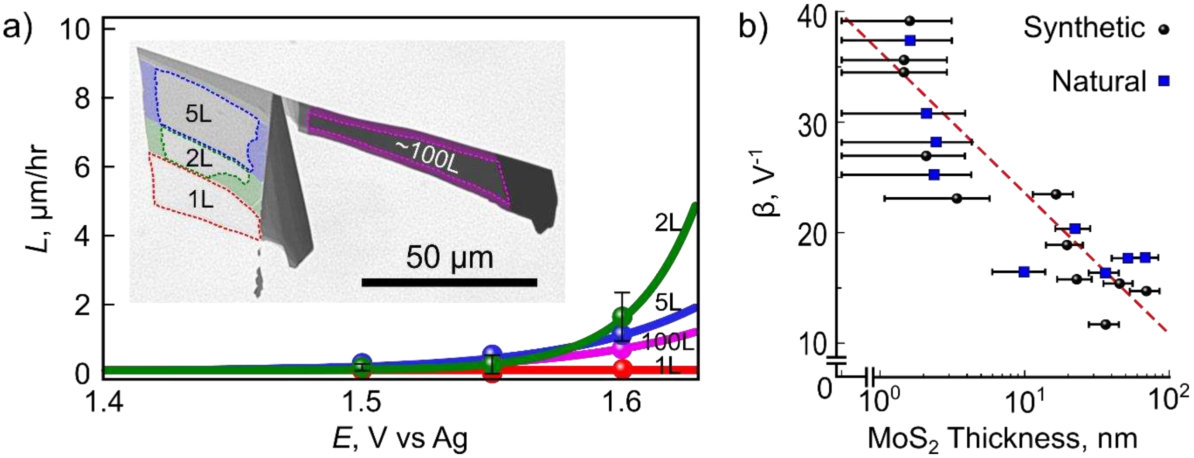

Fig. 3.3 – Thickness dependent anodic dissolution of MoS_2. **(A)** *L* versus *E* for single (1L), bilayer, and five layer-thick (5L) regions of the nanoflake shown in the inset. The solid lines are exponential fits to the *L* versus *E* data. Error bars (±3σ) are shown for the largest error associated with the 2L nanoflake region. The inset shows a brightfield transmission image of the sample after the *E* = +1.60 V potential step. The colored shaded areas highlight the original domain area. The dashed contour lines indicate the domain contour after anodic dissolution occurs. **(B)** Dissolution exponential rate parameter (β) versus nanoflake thickness for 20 nanoflakes (excludes the 1L flakes that do not undergo anodic dissolution). The thickness error bars represent ±2σ uncertainty in correlated profilometry data.

Finally, a major result from our spatially resolved measurements is single layer MoS_2 does not exhibit anodic dissolution under the same range of potentials as multi-layer flakes (see dashed red line in Fig. 3.3A and Fig. B.7 for additional examples). For the mechanically exfoliated samples, we observed two unique behaviors of single layer MoS_2. First, mechanically exfoliated monolayers do not exhibit anodic dissolution even though the material may be in direct contact with a neighboring multilayer-thick domain (Fig. B.9). Second, a multilayer-thick flake can undergo anodic dissolution, but the bottom layer of the nanoflake remains intact. This observation is consistent with literature[109] and only occurs for some regions within a single nanoflake. Possible explanations for these observations are provided in the Discussion section. Additional experiments with 1 cm^2 single layer MoS_2 film samples that were grown by chemical vapor deposition and transferred to the ITO electrode did not exhibit anodic dissolution even after applying +1.70 V for more than 12 hours over 2 days (Fig. B.10). We restricted the applied potential to $\leq$+1.70 V because the ITO electrode undergoes irreversible oxidative damage at higher potentials.[122,123]

3.5 Discussion

Here we discuss a possible explanation for why anodic dissolution occurs faster with decreasing nanoflake thickness. Under electrochemical conditions, Gerischer predicted that anodic dissolution proceeds via an electron tunneling mechanism under dark conditions.[67] In this scenario, electrons associated with midgap surface states tunnel into conduction band states. The energy level scheme below depicts how tunneling occurs (Fig. 3.4A) and how the tunneling probability could change for few layer-thick MoS_2 (Fig. 3.4B). First, the energy level of the electron in the surface state defines the tunneling distance to the isoenergetic position in the conduction band. Electrons located at the highest energy levels of the surface state have a higher probability of tunneling into the conduction band because energy level overlap occurs at a shorter distance at the solid/liquid interface, as indicated by the short thick red arrow in Fig. 3.4A. Conversely, electrons located at lower energy levels of the surface state have a lower tunneling probability into the conduction band because energy overlap occurs at a greater distance into the solid (indicated by thin dashed arrow in Fig. 3.4A).

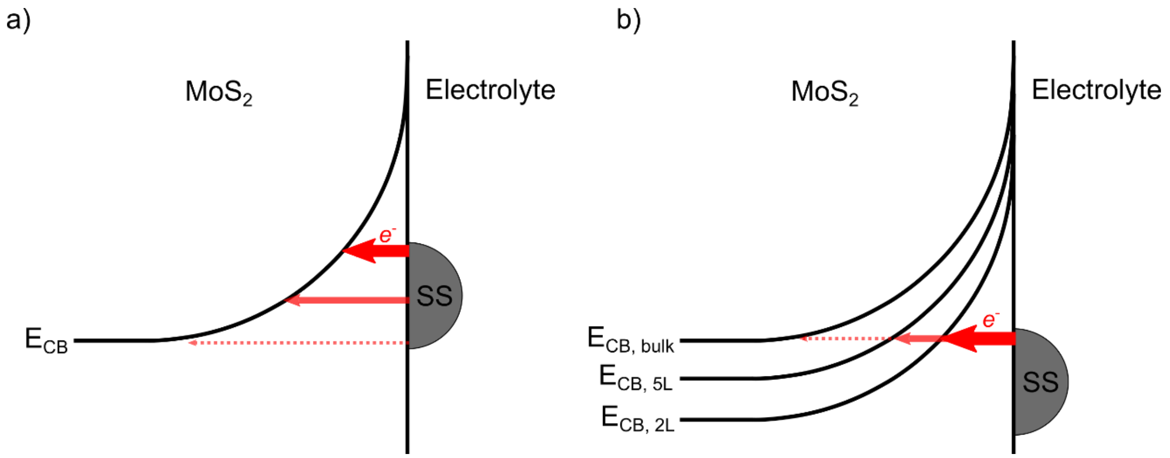

Fig. 3.4 – Energy level diagram between MoS$_2$ conduction band and surface states. (a) anodic dissolution reaction driven by electron tunneling from surface states (SS) into the bulk MoS$_2$ conduction band; (b) possible explanation for the inverse relationship between tunneling probability and layer thickness.

Fig. 3.4B illustrates one possible explanation for our observation that the anodic dissolution rate increases with decreasing layer thickness. It is possible that the band edges change with layer thickness,[77,124] and the band edge movement under applied bias moves the conduction band levels closer to the surface state.[72,79,81] MoS$_2$ undergoes an indirect band gap (1.3 eV) to direct band gap (1.9 eV) transition when the thickness decreases from bulk to monolayer.[47,50] It is possible that the electron tunneling probability increases with decreasing layer thickness as a result of greater energy overlap between the surface states and conduction band levels of the 2D semiconductor. In this scenario, under conditions of equivalent applied potential (e.g., +1.60 V), the tunneling probability is greater for thin material (few-layer, thick red arrow Fig. 3.4B) than for bulk material (thin dashed arrow). Recently, Brunet Cabré et. al. reported slower interfacial electron transfer kinetics for thicker (2L and 3L) crystals.[125] This effect could be linked to the band edge shifts schematically illustrated in Fig. 3.4B.

Next, we discuss a possible explanation for why single layer MoS$_2$ does not undergo anodic dissolution at the same applied potential as few layer-thick and bulk MoS$_2$. One explanation for the enhanced stability is the unique contact from the strong covalent interaction between the single layer MoS$_2$ and the ITO substrate.[109,110] Das et al. proposed that this strong interaction stabilizes the “contact” layer (i.e., TMD layer in contact with the substrate) by suppressing edge reactivity.[126] It is also possible that, due to the stabilization from the ITO substrate, the energy levels of the Mo edge site atoms of the single layer MoS_2 are lower in energy than those for thick layers. The tunneling probability is much less likely for electrons located at the lowest energy levels of the surface state (see Fig. 3.4B). Finally, edge oxidation can terminate dangling bonds along the 1L sheet with MoO_3 that has been shown to have a remarkably large binding energy (2.4 eV).[127] In conjunction with binding to the ITO substrate, MoO_3 could sufficiently cap the 1L edge with an impervious MoO_3 chain-like perimeter. MoO_3 formation on multiple layer MoS_2 may not prevent dissolution because there is no additional MoO_3 binding to the ITO substrate and because the lattice mismatch of edge-stacked MoO_3 would buckle[127] and expose interior defects. Also, the dry anerobic organic solvent limits oxygen to trace contaminants.

Finally, we discuss why some multilayer-thick nanoflakes undergo anodic dissolution and leave behind a single MoS_2 layer (see red region in Fig. 3.3 and Fig. B.9). One possible explanation for complete anodic dissolution is that solvent molecules and/or electrolyte ions can intercalate between the rough ITO substrate and the bottom layer of the thick nanoflake, thereby disrupting the strong interaction between the substrate and 2D semiconductor and enhancing the edge-on dissolution from the reactive edge sites. Another possibility is that the bottom layer of the thick nanoflake is not in direct electrical contact with the substrate, perhaps due to either H_2O/O_2 molecules or residual adhesive material trapped between the substrate and 2D semiconductor as a result of the mechanical exfoliation and transfer process.

3.6 Conclusions

We demonstrated an optical image analysis approach to determine edge dissolution rates of MoS_2 in organic solvent. We determine the onset potential (E_D) for MoS_2 anodic dissolution is ca. +1.473 ±0.016 V versus a 0.01M $Ag/AgNO_3$ reference. Single nanoflake-level measurements revealed that the anodic dissolution rate of MoS_2 nanoflakes increases exponentially with decreasing layer thickness. This trend can be explained via an electron tunneling mechanism, where electrons located in surface states associated with Mo defect sites tunnel into the conduction band; the tunneling probability increases with decreasing layer thickness. Interestingly, single layer MoS_2 does not exhibit anodic dissolution under the same conditions.

A strong interaction between the ITO substrate and single layer MoS_2 could lower the surface state energy of the Mo edge sites, decreasing the tunneling probability and preventing the anodic dissolution process.

CHAPTER 4: QUANTIFYING INTERFACIAL ENERGETICS OF MoS_2 WITH SPECTROELECTROCHEMSTRY AND MANY-BODY THEORY[†]

With knowledge of the stable electrochemical conditions established in Chapter 3, we move to quantifying the energy levels of the 2D semiconductor under electrochemical conditions. Specifically, we want to determine the alignment of the semiconductor's conduction and valence band edges compared to the redox potential of molecules in solution. We first examine the well-characterized absorbance spectra of monolayer MoS_2, and specifically focus on the unique interplay between the A exciton and trion peak in the 600 to 700 nanometer wavelength range. It turns out that a shift in oscillator strength between the exciton and trion peak provide a spectral fingerprint of the MoS_2 carrier density. As electron density increases, the trion peak emerges and the exciton peak is simultaneously quenched. By partnering with theory collaborators to fit experimental data to modelled spectra, we devise a new way to make band energy measurements from spatially-resolved optical measurements.

4.1 Conspectus

2D semiconductors Hot carrier extraction occurs in 2D semiconductor photoelectrochemical cells.[13] Boosting the energy efficiency of hot carrier-based photoelectrochemical cells requires maximizing the hot carrier extraction rate relative to the cooling rate. One could expect to tune the hot carrier extraction rate constant (k_{ET}) via a Marcus-Gerischer relationship, where k_{ET} depends exponentially on $\Delta G^{0\prime}$ (the standard driving force for interfacial electron transfer). $\Delta G^{0\prime}$ is defined as the energy level difference between a semiconductor's conduction/valence band (CB/VB) minima/maxima and the redox potential of reactant molecules in solution. A major challenge in the electrochemistry community is that conventional

---

[†] This chapter is prepared as a manuscript for publication in the journal Energy and Environmental Science. The authors' contributions are found in Appendix A – Division of Work.

approaches to quantify $\Delta G^{0\prime}$ for bulk semiconductors (e.g., Mott-Schottky measurements) cannot be directly applied to ultrathin 2D electrodes. The specific problem is that enormous electronic bandgap changes (>0.5 eV) and CB/VB edge movement take place upon illuminating or applying a potential to a 2D semiconductor electrode. Here, we develop an *in situ* absorbance spectroscopy approach to quantify interfacial energetics of 2D semiconductor/electrolyte interfaces using a minimal many-body model. Our results show that band edge movement in monolayer MoS_2 is significant (0.2-0.5 eV) over a narrow range of applied potentials (0.2-0.3 V). Such large band edge shifts could change k_{ET} by a factor of 10-100, which has important consequences for practical solar energy conversion applications. We discuss the current experimental and theoretical knowledge gaps that must be addressed to minimize the error in the proposed optical approach.

4.2 Introduction

2D semiconductors such as monolayer (ML)-MoS_2 are attractive for photoelectrochemical solar energy conversion and photocatalysis applications because light absorption produces hot carriers that are immediately available to participate in interfacial charge transfer reactions. This ultrathin property could enable the interfacial charge transfer of hot carriers to outcompete charge carrier cooling,[128] which represents a promising strategy to maximize solar energy conversion efficiency.[129,130] The exciting possibility of tuning the electron transfer rate and ensuring it is as fast as possible requires a fundamental understanding of the energy level alignment between the electronic states of the semiconductor and reactant molecules in solution. One could expect to tune the interfacial charge transfer rate constant (k_{ET}) via a Marcus-Gerischer relationship, $k_{\mathrm{ET}} \propto \exp \frac{(-\Delta G^{\circ\prime}+\lambda)^2}{kT}$,[131–133] where λ is the reorganization energy, k is the the Boltzmann constant, and T is temperature.[5–8] $\Delta G^{\circ\prime}$ is the standard driving force for interfacial electron transfer:Boltzmann constant, and T is temperature.[134–136] $\Delta G^{\circ\prime}$ is the standard driving force for interfacial electron transfer:

$$\Delta G^{\circ\prime} = \mathrm{E}_{\mathrm{CB}} - qE^{\circ\prime}, \qquad (4.1)$$

where E_{CB} is the energy of the conduction band edge, $E^{\circ\prime}$ is the formal potential of the redox couple in the electrolyte, and q is the electronic charge. However, rationally tuning the electron transfer kinetics of the 2D semiconductor is difficult because the interfacial energetics of 2D semiconductor/electrolyte interfaces are poorly understood.

The specific problem is the 2D semiconductor energy levels move under working photocatalytic or photoelectrochemical conditions, due to both the applied potential (E)[64,137] and absorption of photons.[138,139] The phenomenon called band gap renormalization (BGR) involves movement of the semiconductor band edges,[21] resulting in a potential- or light intensity-dependent $\Delta G^{0\prime}$ that currently remains unknown or ill-defined.[64] BGR results in the semiconductor band gap energy (E_g) and, therefore, band edge positions change with the semiconductor's carrier concentration (n, cm^{-3}). BGR effects are enormous in 2D semiconductors (e.g., >360 meV in photo-excited ML-MoS_2)[139] due to strong Coulomb interactions, reduced screening effects, and quantum confinement.[21,64,140–148] In the context of photoelectrochemistry, BGR shifts the semiconductor band edges dramatically upon applying a potential to or illuminating the semiconductor, changing $\Delta G^{\circ\prime}$ (see Eqn. 4.1). Importantly, determining the extent to which applied potential, BGR, and other effects tune the semiconductor band energies in these low dimensional materials remains a largely open question inspiring active research. In addition, the large band edge movement is significant because it violates a key assumption in the field of semiconductor electrochemistry: k_{ET} is essentially independent of E because the band edges are "fixed".[149] This assumption means E_{CB} and E_{VB} are independent of E and, therefore, $\Delta G^{\circ\prime}$ is independent of E, too. There is a critical need to quantify interfacial energetics of 2D semiconductor/electrolyte interfaces so we can rationally tune the electron transfer kinetics of these systems for solar energy conversion applications.

Existing approaches and measurement techniques for quantifying interfacial energetics of bulk semiconductors cannot be directly applied to ultrathin 2D electrode materials. Hankin and co-workers discussed and compared popular methods:[20] (1) Mott-Schottky (MS)[150,151] analysis of differential capacitance versus potential data, (2) Gärtner-Butler (GB) analysis[152] of photocurrent-potential data, and

(3) determination of the transition potential between anodic and cathodic photocurrents under chopped illumination. Each method involves key assumptions to extract band edge positions. Those assumptions often fail even for bulk single crystal electrode materials[20] and likely fail for 2D electrode materials. For example, MS and GB analyses assume the applied potential manifests as a potential drop within the semiconductor and the band edges remain fixed. As discussed above, large band edge movement is inherent to 2D semiconductor electrodes. The transition potential method between cathodic and anodic photocurrents interprets the transition potential as the flatband condition, where the band bending in the semiconductor is zero. Interpreting this potential as the flatband condition is problematic for 2D semiconductors because they have large (500 meV)[21] exciton binding energies, and it is unclear how much additional electric field strength (i.e., applied potential) is required to overcome the large binding energy and induce current flow near the zero-field condition. Another complicating factor is the exciton binding energies also renormalize upon applying a potential to the 2D semiconductor. Extracting E_g with optical measurements alone is problematic because we cannot assume the optical band gap and E_g renormalize in the same way.[63,148,153] Another practical experimental challenge for MS measurements is making defect-free 2D semiconductor/substrate contacts so the underlying metallic substrate does not contribute to the capacitance measurement. In summary, the methods for quantifying interfacial energetics of bulk semiconductor/electrolyte interfaces may not be valid for 2D semiconductor electrodes.

Here we propose a new measurement approach to quantify the band edge movement of 2D semiconductor electrodes. Our optical approach involves the following steps: (1) acquire potential-dependent absorbance spectra; (2) extract carrier concentration at each E using many-body theory; (3) determine E_g as a function of carrier concentration using theory or literature data; (2) extract carrier concentration at each E by matching the phenomenology of a physically transparent many-body model shown to predict the dependence of spectra on carrier concentration; (3) determine E_g as a function of carrier concentration using theory,[154] time and angle-resolved photoelectron spectroscopy (TR-ARPES) results,[139] and scanning tunnelling microscopy (STM) measurements[155]; and (4) construct an energy level diagram that quantifies BGR and band edge movement as a function of E. The novel aspect of the approach is how it quantifies carrier concentration via an easily accessible absorbance measurement. The Discussion section describes critical assumptions in steps 2-4 that currently limit the method to the model ML-MoS_2 system, and pinpoints needed developments in experiment and theory to validate the approach for a wide range of 2D materials.

4.3 Methods

4.3.1 Material Synthesis and Transfer

ML-MoS_2 films were grown via MOCVD on sapphire substrates according to Sebastian et al.[156] Molybdenum hexacarbonyl ($Mo(CO)_6$) and hydrogen sulfide (H_2S) served as the Mo and S sources. H_2 served as the carrier gas. The samples were transfer to a 25 mm ×75 mm ×1.1 mm ITO coated glass substrates (Delta Technologies Part No. CB-40IN-S111, R_s=4-10 Ω) using a polymethyl-methacrylate (PMMA)-assisted wet transfer process.[157] First, PMMA (IMM, 495K A5) was spin coated on the ML-MoS_2 coated sapphire substrate. The PMMA-coated sample was immersed in a 1.0 M NaOH solution at 70 °C to separate the PMMA/ML-MoS_2 film from the sapphire substrate. The separated film was then rinsed multiple times inside a water bath and finally transferred onto the target ITO substrate. The rinsed film was lifted from the water bath using the ITO and dried with N_2 gas. A representative Raman spectrum for ML-MoS_2 before and after transfer is shown in Fig 4.1 below. The excitation laser light source is a 532 nm, 1 mW laser. The slight increase in Raman peak splitting is consistent with uniaxial strain from increased surface roughness[158] or the possibility of additional charge impurities or defects introduced from the transfer to ITO[159]. Note the peak splitting increase did not change to such an extent to indicate multilayer MoS_2 (e.g. bi-layer MoS_2 peak splitting is 22-23 cm^{-1}).

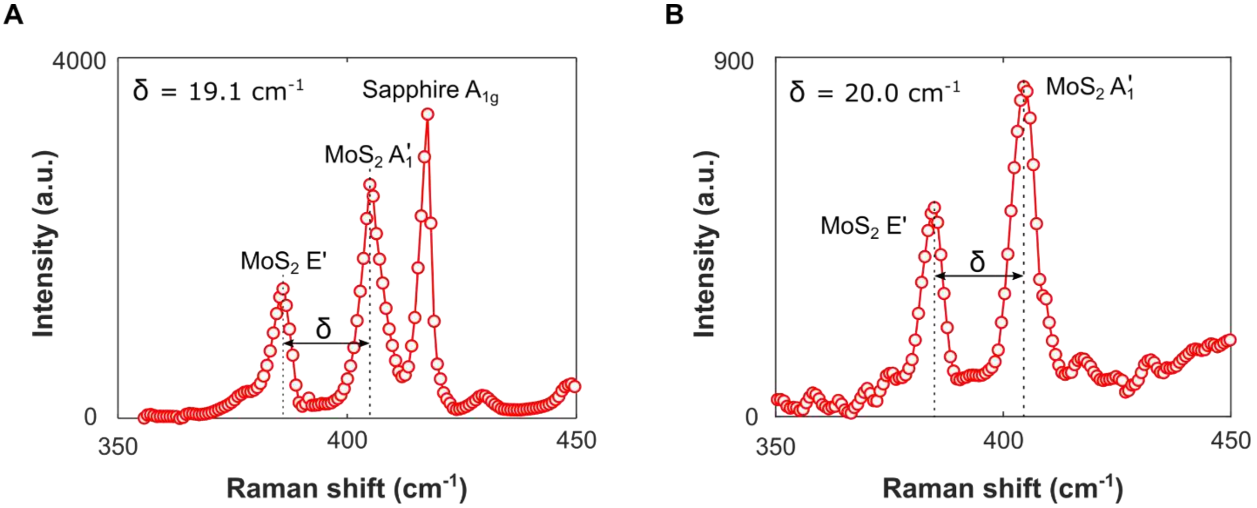

Fig 4.1 - Representative ML-MoS_2 Raman spectra. MOCVD-synthesized MoS_2 on **(A)** sapphire and **(B)** ITO. The Raman peak splitting between the A_1' and E' vibrations is 19.1 cm^{-1} and 20.0 cm^{-1} for the sapphire (as grown) and ITO (transferred) substrates, respectively, in agreement with literature reports for ML-MoS_2.[52]

Confocal Raman micro-spectroscopy was performed on an Olympus IX-73 optical microscope with a 532 nm Ondax THz laser source. Incident light focused on the sample through a 100× NA 0.95 air objective (Olympus PlanFL N100X) with a beam diameter of 0.7 μm (determined from FWHM of the beam profile). The laser power at the sample was typically 1 mW. Light was collected in a backscattering geometry, filtered by the Ondax system, passed through a Horiba iHR550 imaging spectrometer (1800 and 1200 gr/mm), and detected on a Synapse back-illuminated deep depletion charge-coupled device (CCD). The Raman spectra are the average of four sequential 30 s acquisitions. The spectral resolution is < 2 cm^{-1}. The system was calibrated to the pair of Stokes and anti-Stokes Raman peaks for either crystalline silicon ($\pm$ 520.8 cm^{-1}) or sapphire A_{1g} ($\pm$ 417.4 cm^{-1}). All measurements occurred in air at room temperature.

4.3.2 In Situ Spectroelectrochemistry

We constructed a transparent three-electrode microfluidic electrochemical cell according to Wang et al.[99] Electrolyte flowed through the cell at a constant rate of 50 μL/min using an automated syringe pump. The measured potentials versus Ag wire were converted to common vacuum and NHE energy scales using a standard Fc/Fc$^+$ redox couple and a commercial Ag wire / 0.01 *M* $AgNO_3$ electrode

(CHI #112, Fig. B.**1**). The electrolyte was sparged (and later blanketed) with N_2 gas for at least 30 mins prior to flowing through the electrochemical cell.

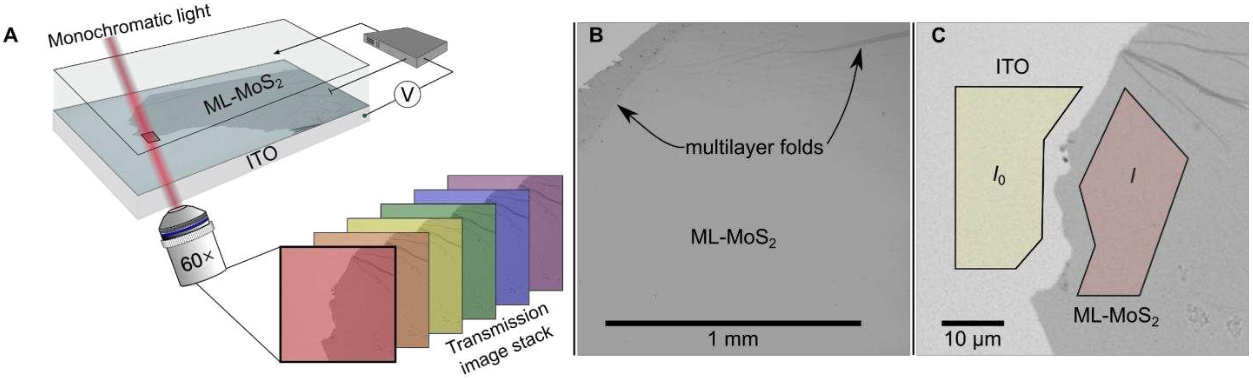

Fig 4.2 - Experimental Setup and Example ML-MoS$_2$ Sample Region. (A) Cartoon illustration of the experimental setup. **(B)** Representative 10× bright field transmission image of the sample showing predominantly ML-MoS$_2$ and some macroscopic defects. **(C)** 60× image of the sample edge. The yellow and red polygons show I_0 and I ROIs used for $A(\lambda) = \log_{10}(I_0(\lambda)/I(\lambda))$ calculations.

The electrochemical cell was mounted on the stage of an inverted optical microscope (Olympus IX73) where a 60× objective UPLANSAPO60x/W) focused light onto a sCMOS camera (Teledyne Prime 95B). An Ivium Compactstat Potentiostat applied a constant potential during each spectral measurement using a Pt wire counter electrode and Ag wire quasi-reference electrode. A Horiba OBB monochromator (1200 gr/mm, 1.2 mm slit) selected light from a Xe lamp source in 2 nm wavelength steps.

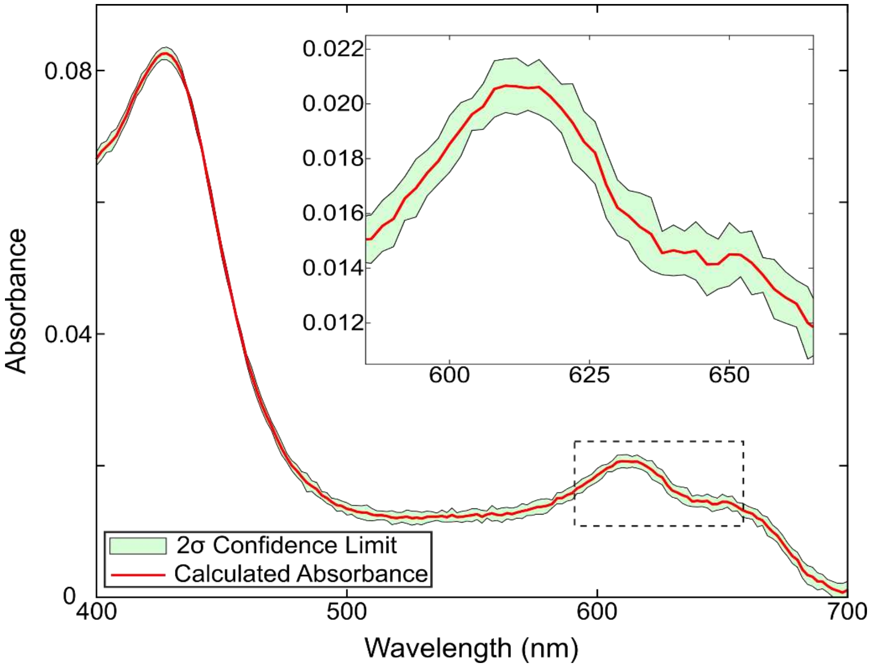

Fig 4.3 - Representative absorbance spectrum with propagated uncertainty. The spectrum was collected for ML-MoS$_2$ immersed in electrolyte in an electrochemical cell without an applied potential (V_{oc} = +0.2 V vs Ag). The shaded region represents the 2σ confidence limit for the measurement calculated at each spectral step (i.e. illumination wavelength).

$A(\lambda)$ was calculated for each respective image with I and I_0 ROI boundaries for each set of potential-dependent spectral data. Each $A(\lambda)$ is the average of measurements from 12 to 16 images. The absorbance data was collected using non-sequential applied potentials. A data acquisition system (DATAQ 4108) synchronized the camera, monochromator, and potentiostat signals. Flake-to-flake variation of mechanically exfoliated natural crystals[160,161] and heterogeneity across individual CVD-grown ML-MoS$_2$ flakes[162] has been shown to influence optical measurements. This spatial variation could influence the absolute n value in a minor way, much smaller than the differences shown in Fig 4.3. Additional experimental details and imaging procedures are located in Section B.11 and Fig. B.11.

4.4 Results

4.4.1 In Situ Absorbance Spectroscopy of ML-MoS$_2$

We employ a widefield hyperspectral imaging method[60] on an optical microscope to ensure our spectroelectrochemistry data stems from only ML-MoS$_2$ material. Fig 4.2A shows the experimental setup.

A MoS$_2$-coated ITO sample serves as the working electrode in an optically transparent three-electrode electrochemical cell (see Methods for detailed metal-organic chemical vapor deposition (MOCVD) MoS$_2$ growth and subsequent wet transfer procedure). In a typical experiment, we immerse the ML-MoS$_2$ sample in dry, N$_2$-saturated electrolyte consisting of 0.25 M tetrabutylammonium hexafluorophosphate ([Bu$_4$N][PF$_6$]) and acquire hyperspectral image stacks at constant E by illuminating a microscopic 0.01 cm^2 sample region with monochromatic light over the range of 400-700 nm in 2 nm increments (Fig 4.3). A 60× objective collects the transmitted light from the sample and projects it onto a sensitive sCMOS camera. Fig 4.2B shows a representative bright field transmission image of the sample. The uniform image contrast across a large 1 mm^2 area indicates the sample is predominantly ML-MoS$_2$, as confirmed by Raman micro-spectroscopy measurements. However, microscopic defects such as tears, voids, wrinkles, and multilayer folds exist within the sample (see black arrows in Fig 4.2B and Fig. B.2D-F. Those defect features ordinarily contribute to and complicate the interpretation of ensemble-level electrochemical and optical data.

To ensure our optical data stems from ML-MoS$_2$ only, we spatially select regions of interest (ROIs) within each image that represent pristine ML-MoS$_2$ and ITO (see Fig 4.2C), and calculate A(l) = log$_{10}$(I_0(l)/I(l)), where I_0(l) and I(l) are the monochromatic light intensities transmitted through the ITO substrate and ML-MoS$_2$, respectively. In this way, we acquire spatially resolved *in situ* absorbance (A) data as a function of applied potential (E (V) vs Ag wire quasi-reference electrode). This procedure effectively removes the contributions from macroscopic defects in the sample. The uncertainty in A is < 0.003 as demonstrated in Fig 4.3. For each absorbance spectrum, the A exciton/trion superpeak is fit to a Gaussian function to extract peak position (centroid) and absorbance (amplitude) parameters. Additional detailed methods of the absorbance measurement and Monte Carlo routine to select ROIs are described previously in Appendix B – Supplemental Information.

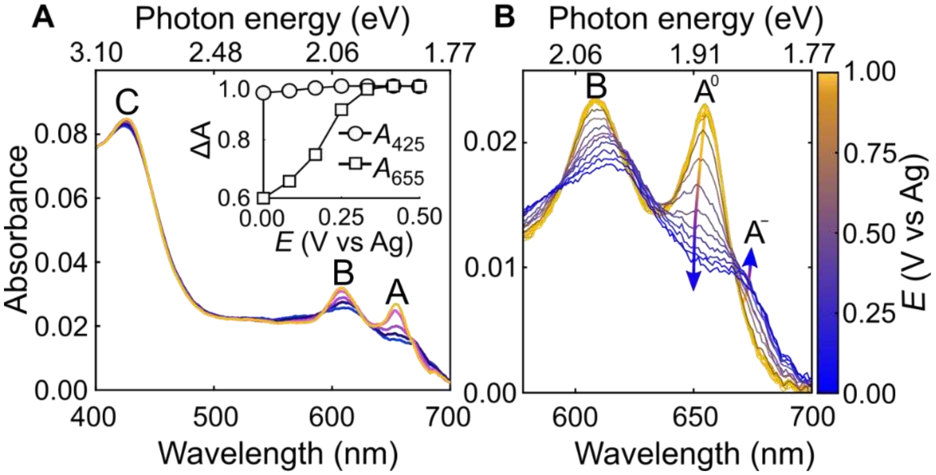

Fig 4.4 - Potential-dependent absorbance spectra. (A) ML-MoS_2 in 0.25 M [Bu4N][PF6] acetonitrile electrolyte. The inset highlights the A (655 nm) and C-exciton (425 nm) peak absorbance changes over a 500 mV potential range, where ΔA is absorbance at each E normalized to the maximum value ($\Delta A = A_V / A_{max}$). **(B)** ML-MoS_2 potential-dependent absorbance highlighting the A-exciton region with 50 mV E steps. The arrows represent potential-dependent absorbance trends for A^0 and A^-.

Fig 4.4 shows representative absorbance spectra of ML-MoS_2 using the hyperspectral imaging technique. Figure B.12 shows additional experimental data from multiple samples and for multiple potential cycles. Regardless of the sample, the number of cycles, and the scan direction, we observed the following potential-dependent trends. First, the absorbance spectra at more positive potentials (light yellow trace in Fig 4.4) shows three distinct peaks at 655, 610, and 425 nm, which can be attributed to the A, B, and C exciton transitions, respectively.[43] The A and B exciton peak intensities decrease and broaden with more negative potential (dark blue trace in Fig 4.4). On the other hand, the C exciton absorbance feature is essentially potential-independent (Fig 4.4 - inset).

The potential-dependent trends in Fig 4.4B agree with literature spectroelectrochemistry data for thin films of three layer-thick MoS_2 nanosheets and >4 nm-thick colloidal film electrodes.[64,163] However, little attention has been paid to the A-exciton lineshape as a function of applied potential. Fig 4.4B shows potential-dependent spectra of the A-exciton peak for another ML-MoS_2 sample using identical experimental conditions as Fig 4.4A. Two distinct optical transitions contribute to the absorption feature.[164] The neutral A-exciton absorbance (A^0) dominates at positive potentials. At more negative potentials, the negatively charged trion (A^-) absorbs strongly, resulting in a shoulder feature at 670 nm (Fig 4.4B). In the section that follows, we describe an approach to quantitatively link the measured absorbance spectrum of ML-MoS_2 to carrier concentration using a minimal complexity many-body model of trion formation in ML TMDs.[164‡] Regardless of the sample or the number of cycles, we observed the same potential-dependent trends as Fig 4.4. In other words, there was no optical hysteresis from the sequence of applied potentials. For the 1.0 V potential range, the absolute change in the absorbance peak amplitudes (ΔA) is consistently 0.011 ± 0.002 (Fig 4.3).

4.4.2 MND Model and fitting procedure to determine electron density (n)

Here we adopt a model based on the Mahan-Noziéres-De Dominicis (MND) Hamiltonian[12], a minimal many-body model of a Fermi polaron, to compute carrier density that best describes the measured absorbance spectrum at each E.[9] A key feature of the model is its ability to capture how A^0 and A^- transitions shift in energy and transfer oscillator strength between one another as a function of doping concentration. Before we discuss the detailed calculation and fitting procedures, we first describe the predictions of the MND model at positive, intermediate, and negative potentials.

MOCVD-grown ML-MoS_2 is n-type, so henceforth we refer to carrier density (n) in terms of electron density.[156,165,166] The majority carriers are conduction band electrons whose population is modulated by the external power supply. At positive potentials (e.g., $E = +1.00$ V, Fig 4.5A), the "undoped" MoS_2 sample consists of a fully occupied valence band and unfilled conduction band. At this undoped condition, the MND model predicts two peaks for the A^0 and A^- transitions (dashed and dotted lines in Fig 4.5A-B). The oscillator strength is mostly associated with the higher energy A^0 transition, as indicated by the thick black line in Fig 4.5A. After convolving the calculated A^0 and A^- linewidths to account for Gaussian broadening and the instrument response, we obtain a single broad peak at 1.894 eV (solid line in Fig 4.5B). The key point here is that the experimentalist observes a single absorbance peak at positive potentials because the oscillator strength is mostly associated with A^0 at lower electron concentrations.

[‡] Additional citation reference pending acceptance and publication (Red/Blue Shift paper)

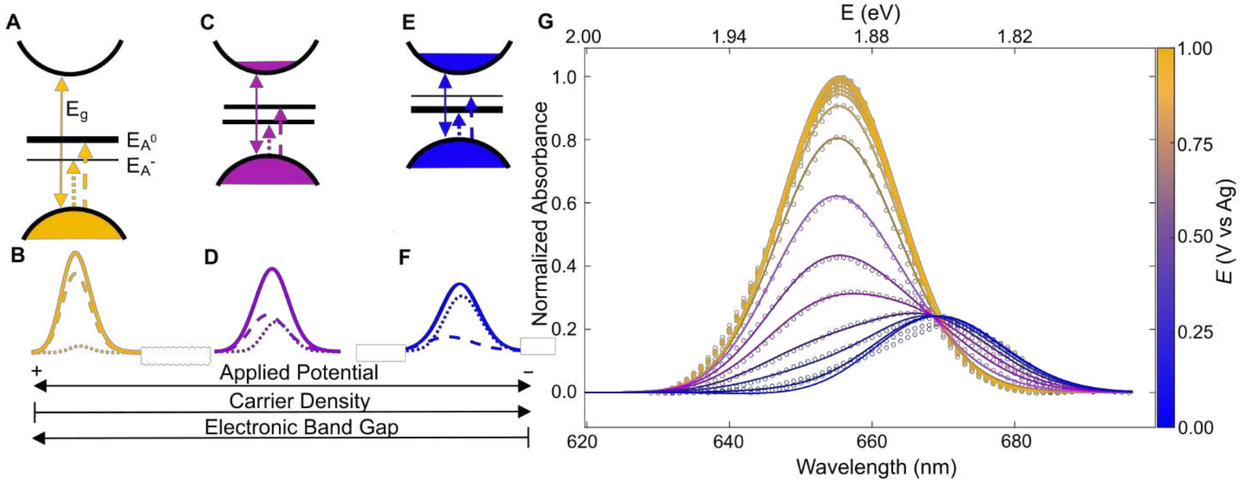

Fig 4.5 - Model Scheme and Fitting of Experimental Absorbance Data. Cartoon illustration of ML-MoS_2 electronic structure changes predicted by the MND model. **(A)** Electronic band gap energy (E_g), neutral A-exciton energy (E_{A^0}) and negatively charged trion energy (E_{A^-}) at the low doping condition (e.g., +1.00 V). **(B)** Simulated absorbance spectrum (solid lines) predicted from the exciton and trion contributions (dashed and dotted lines, respectively). **(C-D)** same as **(A-B)** but for intermediate potentials/intermediate electron doping. **(E-F)** same as **(A-B)** but for most negative potentials/highest electron doping. (**G**) Simulated and optimized absorbance spectra (solid lines) for each experimentally measured absorbance spectrum (circles).

The situation changes as electron concentration increases. The MND model predicts oscillator strength transfers from A^0 to A^-, as indicated by thicker lines for the A^- transition in Fig 4.5E versus Fig 4.5A,C. At the same time, the A^0 and A^- energies decrease, but in different amounts (see dashed and dotted arrows in Fig 4.5C,E versus Fig 4.5A). The oscillator strength shift changes the A^0:A^- intensity ratio and the peak energy shifts complicate the observed spectrum. As the applied potential shifts from positive to negative, the experimentalist observes a "super peak" split into two discernable peaks (see convolved spectrum in Fig 4.5D, F). A key point of the scheme in Fig 4.5 is that the MND model predicts how and why the "super peak" absorbance feature at low n (positive potentials) transitions to two separate peaks at high n (negative potentials). Having summarized the general predictions of the model, we can now discuss the general fitting procedure to determine electron concentration at each E for the experimental data in Fig 4.4. Complete MND model calculation details are found in previous work.* Briefly, the model quantitatively links the experimental observable (absorbance spectrum) to electron concentration via the Fermi doping energy parameter ε_F, defined as an energy level position at or above the conduction band minimum.[56,164,167]

First, we obtain model parameters, the undoped A^0 peak position (i.e., energy, width, and height), using data acquired at E = +1.00 V and account for phenomenological peak broadening by convolving the simulated peak with a Gaussian. Then, for all other more negative E values (i.e., higher ε_F conditions), we make an initial guess at the parameters for both A^0 and A^- and perform a 5-step procedure to determine ε_F for every E.[*] The rationale of the steps is to model the data at the level of the MND outputs (peak positions, heights, and widths) instead of guessing at the correct Hamiltonian. We can infer the doping density from the ratio of peak heights in the experimental data based on the series of spectra predicted from the MND model.

Fig 4.5G shows the results of the fitting procedure applied to the absorbance spectra in Fig 4.4. The model captures all potential-dependent features of the A-exciton region, specifically how the A^0 and A^- peak intensities, positions, and widths change with applied potential. A key point of Fig 4.5G is that we obtain a single ε_F value that best describes the measured spectrum. Minor disagreement between the MND model and experimental data, such as the high energy tail region, is likely due to the fact that the MND model only considers the ML-MoS_2 sample in vacuum and does not consider the possible screening effects from the substrate and redox electrolyte.[9] Disagreement between the theory and experiment may also be due to non-Gaussian sources of broadening that we do not consider, as well as the simple background subtraction method that does not accurately remove contributions from the B exciton and B trion,[59] which the model does not consider.

Having determined ε_F for each E, we then calculate electron concentration. Previous work applying the MND Hamiltonian to ML-MoS_2 has derived an equation to calculate 2D electron concentration, n (in units of cm^{-2}) assuming a parabolic band structure:

$$n = \frac{\upsilon m_e \mu}{2\pi} \qquad (4.2)$$

where the degeneracy factor v = 1, the effective mass of the electron m_e = 0.045 eV^{-1}Å^{-2} s for pristine ML-MoS$_2$[164] and μ is the chemical potential. At T = 0 K, $\varepsilon_{\mathrm{F}} = \mu$. Hence, we substitute the fitted ε_{F} values for μ in Eqn. 4.2 to calculate electron concentration. We discuss limitations of this zero-temperature approach below.

Fig 4.6 shows calculated electron density n values versus E. Electron concentration remains low for E > +0.50 V, and then it abruptly increases by an order of magnitude over a narrow range (0.30 to 0.50 V). Electron concentration steadily increases with increasingly negative potentials (E < 0.20 V). The calculated n values agree with measured values for ML-MoS$_2$ samples synthesized using the same MOCVD procedure[156]. For comparison, we also calculated n values using the approach of Carroll et al.[64], who adapted Wannier-Mott (WM) effective mass theory for 2D quantum wells[168,169] to 2D semiconductors. The model assumes that the exciton is strongly confined within two dimensions, and that the photogenerated electron in the conduction band and the hole in the valence band have essentially the same magnitude. Therefore, the exciton states are written as a linear combination of the independent electron holes and states and, the carrier density is derived from relative ratio of exciton oscillator strength[64,168]. Notably, the WM model does not consider the potential-dependent A^{-} feature and, therefore, the A-exciton region of the absorbance spectrum is fitted with a single component Gaussian. As shown below in Fig 4.6 the electron concentration differs by an order of magnitude but the models result in qualitatively similar behaviour.

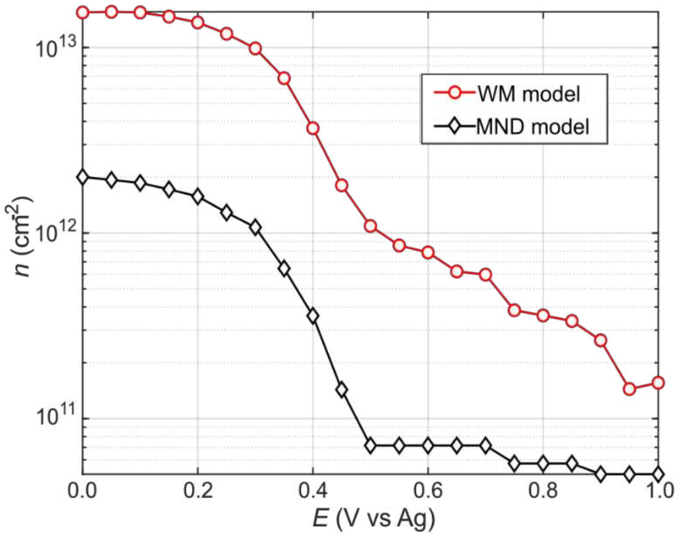

Fig 4.6 - Comparison of two models to calculate electron density. Potential-dependent electron concentration values calculated via the MND (black diamonds) and WM models (red circles).

The n values calculated from the MND model are likely lower because the approach ignores thermal contributions and, therefore, will underestimate the true concentration of conduction band electrons. The MND model only considers the ML-MoS$_2$ sample in vacuum and does not consider substrate/electrolyte or sulfur vacancy contributions to n-type doping.[54,170] On the other hand, the n values calculated from the Wannier-Mott model sensitively depend on the exciton Bohr radius ($n \propto a_0^{-2}$), which linearly depends on the effective mass of the electron (m_e).[58] Varying a_0 or m_e by a factor of 3 results in nearly an order of magnitude change in n (Fig 4.7). The Bohr radius is influenced by the dielectric environment of the sample and needs to be addressed.

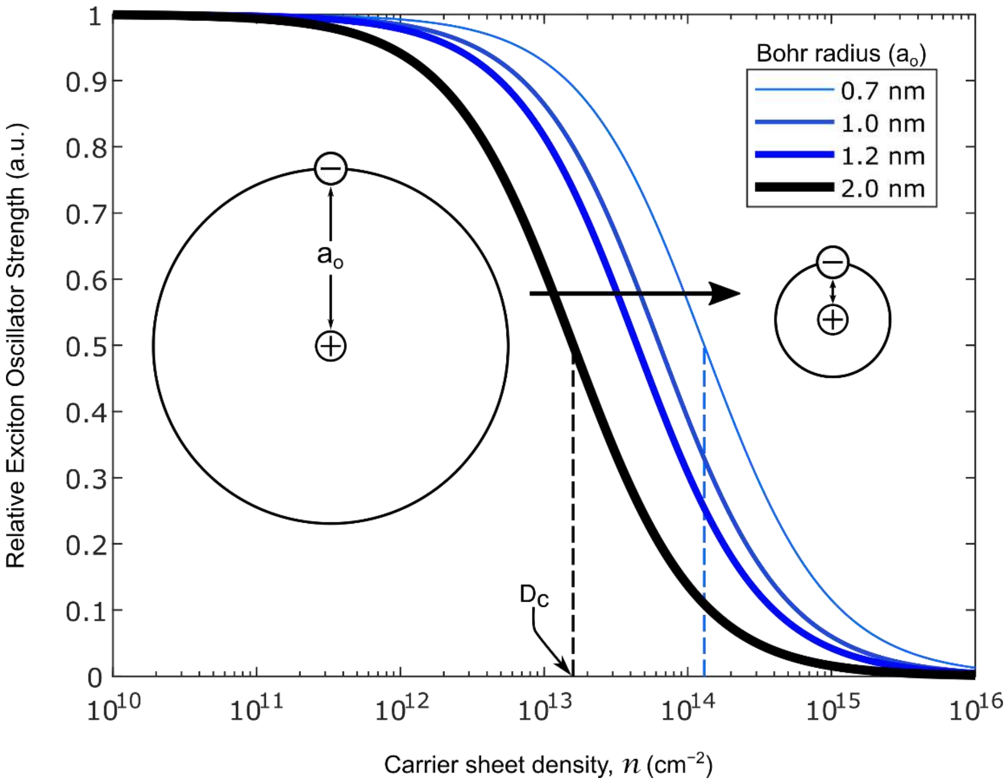

Fig 4.7 - Relative exciton oscillator strengths as a function of n using the Wannier-Mott model. The critical doping density (D_c) is annotated with a dashed line to highlight the large influence of a_0 on n using this method.

The dielectric environment considered here consists of three layers: ε_{ITO}, ε_{MoS_2}, and ε_{MeCN} with reference values for the respective dielectrics taken as 4.0,[171] 12,[58] and 36[172]. The effective dielectric constant, ε_{eff}, is wave vector dependent in ML-MoS$_2$ because its thickness and exciton radius are comparable. In the large wave vector limit, ε_{eff} approaches ε_{MoS_2} = 12.[58] In the small wave vector limit, ε_{eff} approaches $\frac{\varepsilon_{ITO} + \varepsilon_{MeCN}}{2}$ = 21. The dielectric environment, n, and a_0 are not mutually exclusive parameters, so several values of a_0 are used to calculate the carrier density using the WM model (Fig 4.7).[168] The a_0 distances chosen in Fig 4.7 correspond to a range of experimental and theoretical results and the ε_{eff} in this study.[58,169,173] Importantly, this shows the dramatic effect of a_0 when using this approach to calculate n from exciton oscillator strength (i.e. relative absorbance values). Regardless, while it is difficult to know at this stage what the true absolute numbers for the electron concentration are, the remarkable agreements in the trends obtained using the two different approaches discussed indicate that the trends observed for the electron density as a function of applied potential are robust.

4.4.3 Band Energy Diagram Construction

Finally, we construct a band energy diagram for the ML-MoS_2 electrode using the following assumptions. First, we pin the conduction band edge of ML-MoS_2 at +0.45 V vs NHE[154,174,175]. Second, we assume band gap renormalization (BGR) only occurs in the valence band (VB), in agreement with theory,[154] time- and angle-resolved photoelectron spectroscopy (TR-ARPES) results,[139] and scanning tunnelling microscopy (STM) measurements[155]. Third, we position the VB edge relative to the fixed CB edge using n-dependent band gap energy, E_g, from theory (**Fig 4.8**) or experiment.[63]

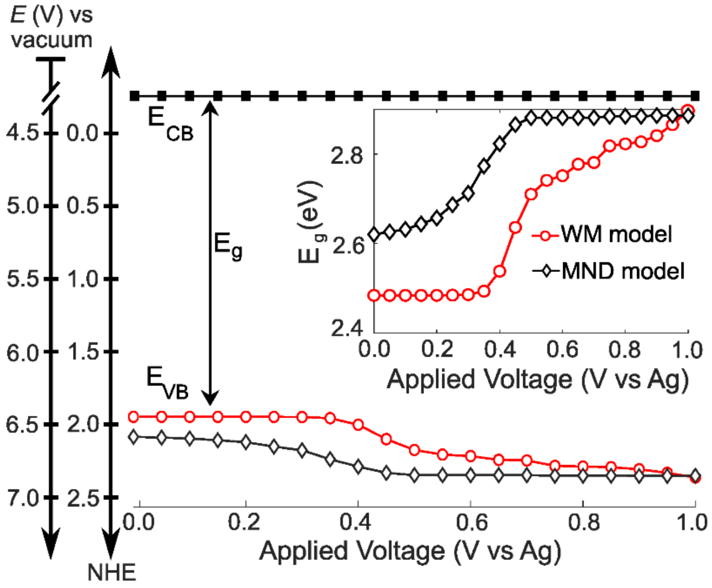

Fig 4.8 - Potential-Dependent Band Energy Diagram of ML-MoS_2. The inset shows the band gap energy as a function of *E*. All measurements with 0.25 M [Bu_4N][PF_6] acetonitrile electrolyte.

Fig 4.8 shows the resulting band energy diagrams of ML-MoS_2 as a function of *E* using *n* values calculated from both the MND and WM models. At positive potentials, E_g approaches the value predicted for "undoped" ML-MoS_2 (see **Fig 4.8** inset). E_g decreases with increasingly negative *E*, causing the VB minimum to shift by over 200 meV over a narrow *E* range. The E_g decrease (and upward VB shift) is larger for larger values of *n*, such as those predicted by the WM model (see red circles in **Fig 4.8**). E_g values obtained from TR-ARPES measurements[139] qualitatively agree. The key point of **Fig 4.8** is that BGR effects cause significant band edge movement (0.2-0.5 eV) and should be given consideration when designing 2D electrodes for electrochemical applications, as will be discussed more below. Importantly, the majority of the BGR shown here occurs over a relatively narrow range of applied potentials.

4.5 Discussion

The enormous BGR effect in 2D semiconductors has important consequences for any electrochemical application involving interfacial charge transfer. The large CB or VB shifts (0.5 eV) can occur over a very narrow range of applied potentials (0.2-0.3 V). In turn, the fundamental driving force for the reaction $\Delta G^{\circ\prime}$ changes dramatically. From a kinetic standpoint, the large band edge movements will dramatically affect interfacial charge transfer rates. If the electron transfer rate constant k_{ET} follows a Marcus-Gerischer relationship, where $k_{\mathrm{ET}} \propto \exp \frac{(-\Delta G^{\circ\prime}+\lambda)^2}{kT}$, then large $\Delta G^{\circ\prime}$ changes (e.g., 0.5 eV) could change k_{ET} by a factor of 10-100.[135,136] It is even possible that $\Delta G^{\circ\prime}$ changes sign if the VB/CB edge moves above/below $E^{\circ\prime}$. This means the (photo)electrocatalytic reaction could transition from being spontaneous in one potential regime to non-spontaneous in another. Note, our study focused only on BGR effects caused by the applied potential. For light-driven reactions in a photoelectrosynthetic cell, the band edge movement will be driven by the applied bias and the photogenerated carrier population,[176] further complicating the interfacial energetics. One could envision leveraging this kinetic or thermodynamic information to design an “electrochemical switch” for a desired reaction.

We now discuss key assumptions in the proposed approach and point out clear next steps to make this approach more robust with future advances in experiment and theory. First, our experimental method does not directly measure band edge positions. We assumed a potential-independent CB minimum value for this model MoS_2 system, which may not be valid across all 2D materials and those that have yet to be discovered. New *in situ* methods are needed to determine band edge positions of the 2D electrode. Direct measurement of CB and VB edges yield E_g, which could be compared to the E_g values we extract from *in situ* absorbance measurements.

Second, we quantify band edge movement by extracting E_g values as a function of n. The first problem with this strategy is the accuracy of n values obtained using either the MND or WM models. We calculate n from the ε_F parameter in the MND model using Eqn 4.2, which considers the pristine semiconductor at 0 K. Aside from ignoring the thermally excited carriers, the MND model does not consider the electrolyte, underlying substrate, spin-orbit coupling to treat the B-exciton and B-trion, and defects that could serve as extrinsic dopants in the 2D material. A growing body of evidence has shown that defect concentrations and types,[159] substrate materials,[54] solvent,[177] and surrounding environment[61] all influence n.[178] Current theory does not consider many practical materials and electrochemical factors. Future theory development is needed to accurately determine electron concentration using *in situ* spectroelectrochemistry (e.g., absorbance/reflectance, Raman, or PL spectroscopy). The second problem with the strategy is it relies also on the accuracy of E_g values as a function of n. Experimentally measured E_g values[139] show similar trends as the theoretical calculations,[179,180] but the absolute values can differ by as much as 0.2 eV. The disagreement could be due to the fact the models do not consider defects and substrate/environmental doping effects. Despite the current inaccuracy of calculating n and E_g, we believe *in situ* absorbance measurements, modelled by many-body theory, represent a viable approach to quantify interfacial energetics because there is a robust theoretical framework connecting the observed spectrum to critical parameters relevant to semiconductor energy levels (n and E_g).

One clear advantage of our proposed approach is experimental simplicity. Commercially available UV-vis spectrophotometers have absorbance resolution ≤ 0.001, which is an order of magnitude lower than exciton absorbance peak values of ultrathin semiconductors (Fig 4.3). However, large area, defect-free samples are required for benchtop absorbance measurements. Ensemble-average measurements in a benchtop instrument report on the average behaviour of the entire sample in the light path, which could include defects and pinholes in the material as shown in Fig 4.2B and Fig. B.2D-F. One disadvantage of our proposed approach is the MND model calculations are not trivial. We argue the advantages and disadvantages of the optical approach proposed herein are similar to the popular Mott-Schottky method for bulk semiconductor/electrolyte interfaces; Mott-Schottky data is easy to acquire but can be difficult to interpret.[20] Future experimental and theoretical work is needed to adapt the proposed approach for a wide range of 2D materials and electrochemical cell geometries and components.

4.6 Conclusions

In summary, we developed an all-optical approach to quantify the interface energetics of ML-MoS_2 semiconductor-electrolyte interfaces. The method involves (1) measuring potential-dependent absorbance spectra; (2) fitting the neutral exciton and trion features in the absorbance spectrum using the MND model to extract the electron concentration, n; (3) extrapolating the electronic band gap at each E using n; (4) constructing an energy level diagram assuming a known, potential-independent CB edge value. Our results show that band edge movement in ML-MoS_2 is significant (0.2-0.5 eV) over a narrow range of applied potentials (0.2-0.3 V). The band edge movement magnitude depends on the calculated n values. Large band edge shifts have important consequences for practical electrochemical applications involving interfacial charge transfer because k_{ET} could change by a factor of 10-100. Future experimental and theoretical work is needed to accurately measure n from *in situ* spectroelectrochemical measurements such as absorbance/reflectance, Raman, or PL spectroscopy.

4.7 Acknowledgements

This research was supported by the U.S. Department of Energy, Office of Science, Office of Basic Energy Sciences, under Award DE-SC0021189. Justin Sambur acknowledges a Sloan Research Fellowship. Justin Toole acknowledges funding through the Army Advacned Civil School program and support from the United States Military Academy (West Point, NY).

The samples were grown in the 2D Crystal Consortium Materials Innovation Platform (2DCC-MIP) facility at Penn State which is supported by the National Science Foundation under cooperative agreement DMR-2039351.

This material is based upon work supported by the National Science Foundation Graduate Research Fellowship Program under Grant No. DGE1255832.

CHAPTER 5: REDOX CONTROL OF MONOLAYER MoS2 INTERFACIAL ENERGETICS

The next question addressed in this project is how the interfacial energetics of ML-MoS_2 changes when immersed in different electrolyte environments. Extending the methods and electrochemical cell from the previous study, we now turn to the other side of the interface: the electrolyte. We aim to control optical and electronic properties of the ML-MoS_2 by interfacial contact with different redox species.

Here, the initial hypothesis is: if redox species chemically dope MoS_2 then the optical absorbance spectrum matches that of electrostatically-gated conditions. In a systematic way of varying redox species, it may be possible the energetics of the material such as the flat-band potential (E_{FB}) can be bracketed on an absolute energy scale. This study provides an improved description of the semiconductor-electrolyte interface.

5.1 Introduction

Layered transition metal dichalcogenides (TMDs) semiconductors show promise in many electronic, solar, and sensor applications. One such well-studied two-dimensional (2D) TMD is MoS_2. The stable exciton formation that dominates its visible absorbance spectrum can be influenced by electron density.[56,181] In addition electron density modulates the formation of an additional charge exciton with further changes the optical properties of MoS_2 even at room temperature.[56] One traditional method of modulating charge carrier concentration in semiconductors is applying a gate bias in a field-effect transition device, but this device requires a fixed geometry with finite terminals. An alternate approach is to chemically dope the semiconductor via charge transfer: either injecting electrons (n-type dopant) or extracting electrons (p-type dopant). This charge transfer should immediately induce a shift in the semiconductor's Fermi level and thus immediately change its electrical and optical properties.

Others reported chemical or molecular doping of MoS_2 using surface drop cast methods,[182] gas physisorption,[183] solvent immersion[184] and computational calculations.[185] In these cases, the general methodology is to measure one two chemical dopant environments to compare the electron donating or withdrawing effects on MoS_2. However, the spontaneous charge transfer does not occur if the chemical potential of the species is equivalent to the Fermi level of MoS_2, and this is the case for equilibrium conditions at the surface of the semiconductor.

A liquid electrochemical flow cell environment is ideal for rapidly evaluating many chemical species with varying electrochemical potentials. First, the formal potential ($E^{0\prime}$) of an electrochemically reversible redox couple in a solution defines its electrochemical potential. Here an oxidant (O) + e $\rightleftharpoons$ reductant (R). In addition, the equilibrium redox potential is a function of the relative activity of O and R, and characterized by the Nernst equation:

$$E = E^{0\prime} - \frac{RT}{nF}\ln\frac{\alpha_O}{\alpha_R} \qquad (5.1)$$

Control of the electrochemical potential of the redox environment by flowing electrolytes across the MoS_2 surface should modulate its electron concentration immediately. This electronic modulation can be optically measured. Crucially, redox species concentration is a way to fine-tune the electronic state to within a couple hundred meV.

Here our preliminary data demonstrates that redox species chemically dope ML-MoS2 in an electrochemical flow cell. The optical absorbance signatures drastically change as a result of n-dopant or p-dopant molecules. Further investigations by controlling redox couple concentrations may pinpoint the elusive flat band potential of a 2D semiconductor using optical measurements.

5.2 Methods

The rationale for selecting the redox potentials of many reversible 1-electron transfer couples begins with previous measurements in organic electrolytes.[186] The electrolyte influence on the interfacial energetics may be determined using optical exciton absorbance measurements in a transparent electrochemical flow cell. The MOCVD grown MoS_2 monolayers is n-type, so the Fermi level (E_F) is near the conduction band edge (E_{CB}) .[156,165] For example, Fig. 5.1 shows the formal potential of several common redox couples in the approximate band gap region of MoS_2. Under electrostatic gating, modulation of the semiconductor E_F relative to a fixed redox formal potential will deplete or accumulate electrons in the semiconductor and results in a measurable cathodic or anodic flow of electrons, respectively.

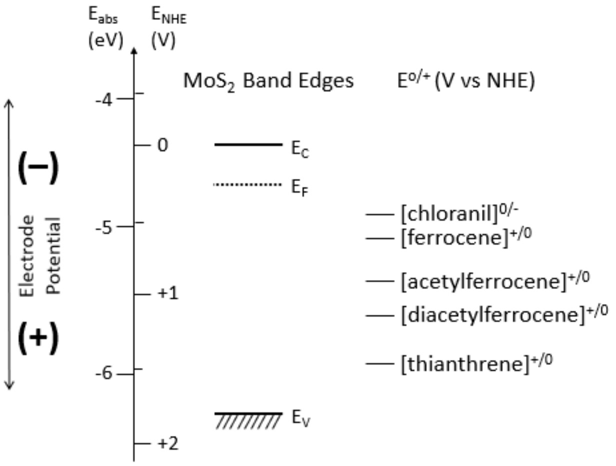

Fig. 5.1 – Relative formal potential of several reversible redox couples. The rational for selecting the redox species is based on the location of the formal potential ($E^{0\prime}$) versus the intrinsic MoS2 band edges.

5.3 Preliminary Results

As a proof of concept, measurements with ferrocene / ferrocenium (Fc/Fc^+) and decamethylferrocene / decamethylferrocenium ($Me_{10}Fc/Me_{10}Fc^+$) redox couples in the flow cell indicate optical response of MoS_2 is controlled by the electrolyte. For example, Fig. 5.2 shows the absorbance spectrum of $Me_{10}Fc/Me_{10}Fc^+$ in electrolyte matches an equivalent applied potential of +0.1 V vs Ag wire. The measured redox potential of this couple is -0.4 V vs Ag wire, so the charge transfer is less than expected; however, it should be pointed out that the optical response deviates from the open circuit potential. The experimental data proves the electrolyte is manipulating the optical properties. However, the redox does not modulate the optical response to such an extent that matches the formal potential of the couple.

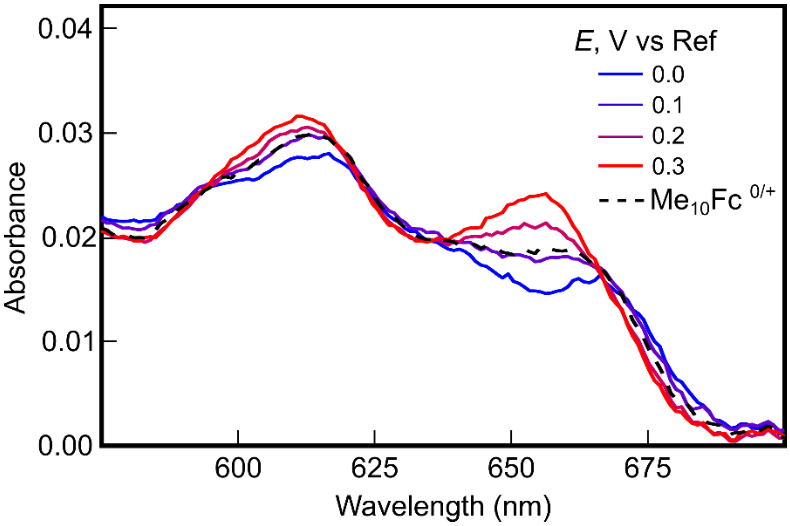

Fig. 5.2 – MoS_2 Absorbance Spectrum with $Me_{10}Fc$ redox couple. The optical spectrum of decamethyl ferrocene redox couple is similar to an applied potential of +0.1 V vs Ag wire quasireference.

5.4 Discussion

For illustration, Fig. 2.1 depicts relative band edge energy levels of MoS_2 and electrochemical potential of a liquid electrolyte (e.g. ferrocenium/ferrocene solution). The relative energy levels are independent before the phases are in contact. The example electrolyte represents any stable liquid solution containing a redox pair (A^+/A) where $A^+ + e^- \rightleftharpoons A$ is a reversible reaction. The uncertainty in the absolute A exciton peak absorbance is estimated as 0.003 as shown in Fig 4.3, so changes in peak absorbance . Also, the absorbance of the redox species should not affect the measurements because the liquid electrolyte immerses the MoS_2 and the ITO with equivalent pathlength of the incident light.

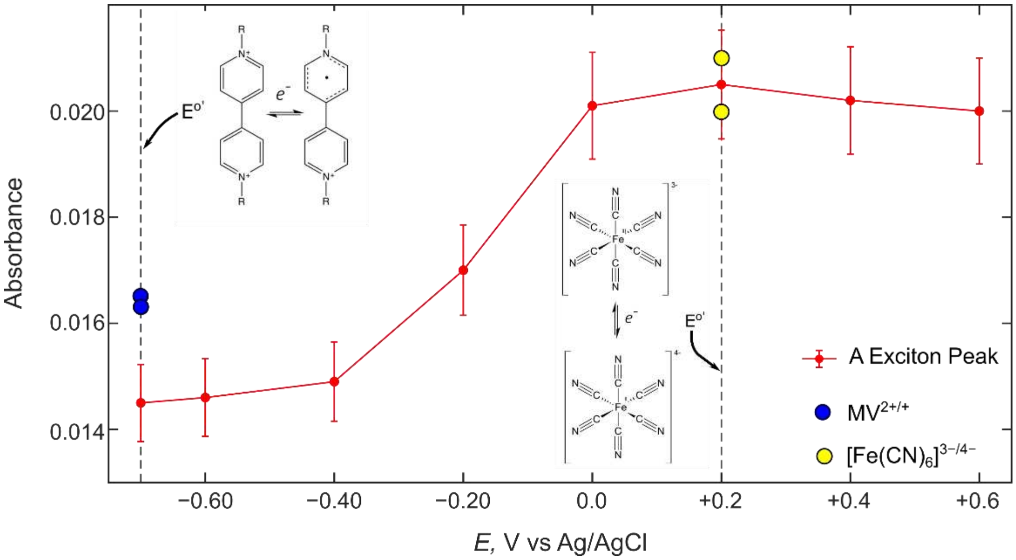

Fig. 5.3 – Additional redox couple molecular gating of MoS_2. Reference is Ag/AgCl and electrolyte is 0.1 M KCl in H_2O.[§]

Fig. 5.3 highlights the promising correlation of the optical properties of MoS_2 after chemical doping. However, the inability of methyl viologen (MV) to fully bleach the A exciton is attributed to several potential causes. First, surface states from defects (most likely S vacancies) are expected to pin the Fermi level. Second, the physical contact of the redox couple may be restricted in the flow cell arrangement. The flow rate through the cell may indicate if the Third, the ITO electrode may chemically bind the redox couple. Specifically, Fe has been reported to bind to this electrode.[187]

[§] Data provided by Rafael Almaraz (see Appendix A)

CHAPTER 6: OUTLOOK AND FUTURE WORK

In addition to the necessary development of results shown in Chapter 5, several logical extensions of this work are described below. The purpose of this chapter is to document logical progression of this work based on the resources available to the Sambur research group at Colorado State University. This also provides initial hypotheses and considerations to guide new investigations.

6.1 MoS_2 Doping Heterogeneity Influence on Corrosion

The most recent and directly relevant work in the Sambur group that overlaps with this work is that of Van Erdewyk.[65,188] A reasonable hypothesis is p and n-type doped domain junctions correlate to the inter-flake corrosion initiation sites. Correlated photocurrent mapping following by full-flake corrosion experiments may show that these junctions are more likely to initiate and/or accelerate corrosion. This is in addition to the interesting possibility that the majority carrier (e^- or h^+) may also control the corrosion onset or rate. For example, it is possible that natural p-doped regions do not behave similar to the predominant n-doped regions. Differences in the natural (i.e. SPI source) and synthetic crystals deserves attention to more fully develop this possibility. This includes correlated photocurrent mapping and possibly illuminating with various high intensity light sources to photo-anodically accelerate or otherwise control the corrosion.[17]

The recent setup of a Scanning Electrochemical Cell Microscopy (SECCM) instrument allows for localized corrosion investigations. SECCM uses a nano or micro-pipette droplet to confine the size of a electrochemical cell, and by hopping the pipette across the material or substrate, an electrochemical map is revealed.[189–191] This is a proven technique that can operate in the aprotic electrolyte use here and at the potential range necessary to initial anodic corrosion. An obvious hypothesis is that the edge corrosion onset potential and lateral corrosion rate would match that of the ensemble electrochemical cell. In addition, the SECCM permits localized current measurements that are not possible with. This is especially important to measure the potential at which photoexcited material begins to anodic current if the illumination of the n-type material increases the anodic potential.

BIBLIOGRAPHY

(1) Henry, C. H. Limiting Efficiencies of Ideal Single and Multiple Energy Gap Terrestrial Solar Cells. *J. Appl. Phys.* **1980**, *51* (8), 4494–4500. https://doi.org/10.1063/1.328272.

(2) Heller, A. Conversion of Sunlight into Electrical Power and Photoassisted Electrolysis of Water in Photoelectrochemical Cells. *Acc. Chem. Res.* **1981**, *14* (5), 154–162. https://doi.org/10.1021/ar00065a004.

(3) Ross, R. T.; Nozik, A. J. Efficiency of Hot-Carrier Solar Energy Converters. *J. Appl. Phys.* **1982**, *53* (5), 3813–3818. https://doi.org/10.1063/1.331124.

(4) Tan, M. X.; Laibinis, P. E.; Nguyen, S. T.; Kesselman, J. M.; Stanton, C. E.; Lewis, N. S. Principles and Applications of Semiconductor Photoelectrochemistry. *Princ. Appl. Semicond. Photoelectrochem.* **1994**, *41*, 21–144.

(5) Haram, S. Semiconductor Electrodes. In *Handbook of Electrochemistry*; Elsevier, 2007; pp 329–389. https://doi.org/10.1016/B978-044451958-0.50022-7.

(6) Chiu, Y.-H.; Lai, T.-H.; Kuo, M.-Y.; Hsieh, P.-Y.; Hsu, Y.-J. Photoelectrochemical Cells for Solar Hydrogen Production: Challenges and Opportunities. *APL Mater.* **2019**, *7* (8), 080901. https://doi.org/10.1063/1.5109785.

(7) Tenne, R.; Wold, A. Passivation of Recombination Centers in N-WSe2 Yields High Efficiency (>14%) Photoelectrochemical Cell. *Appl. Phys. Lett.* **1998**, *47* (7), 707. https://doi.org/10.1063/1.96066.

(8) Tributsch, H. Solar Energy-Assisted Electrochemical Splitting of Water. Some Energetical, Kinetical and Catalytical Considerations Verified on MoS2 Layer Crystal Surfaces. *Z. Für Naturforschung A* **1977**, *32* (9), 972–985. https://doi.org/10.1515/zna-1977-0911.

(9) Gerischer, H. Electrochemical Photo and Solar Cells - Principles and Some Experiments. *J. Electroanal. Chem.* **1975**, *58* (1), 263–274. https://doi.org/10.1016/S0022-0728(75)80359-7.

(10) Gratzel, M. Photoelectrochemical Cells. *Nature* **2001**, *414* (6861), 338–344. https://doi.org/10.1038/35104607.

(11) Shank, C. V.; Fork, R. L.; Leheny, R. F.; Shah, J. Dynamics of Photoexcited GaAs Band-Edge Absorption with Subpicosecond Resolution. *Phys. Rev. Lett.* **1979**, *42* (2), 112–115. https://doi.org/10.1103/PhysRevLett.42.112.

(12) Nie, Z.; Long, R.; Sun, L.; Huang, C.-C.; Zhang, J.; Xiong, Q.; Hewak, D. W.; Shen, Z.; Prezhdo, O. V.; Loh, Z.-H. Ultrafast Carrier Thermalization and Cooling Dynamics in Few-Layer MoS_2. *ACS Nano* **2014**, *8* (10), 10931–10940. https://doi.org/10.1021/nn504760x.

(13) Austin, R.; Farah, Y.; Sayer, T.; Luther, B. M.; Montoya-Castillo, A.; Krummel, A.; Sambur, J. Hot Carrier Extraction from 2D Semiconductor Photoelectrodes. arXiv October 24, 2022. http://arxiv.org/abs/2210.13588 (accessed 2023-03-04).

(14) Rogdakis, K.; Karakostas, N.; Kymakis, E. Up-Scalable Emerging Energy Conversion Technologies Enabled by 2D Materials: From Miniature Power Harvesters towards Grid-Connected Energy Systems. *Energy Environ. Sci.* **2021**, *14* (6), 3352–3392. https://doi.org/10.1039/D0EE04013D.

(15) Qian, W.; Xu, S.; Zhang, X.; Li, C.; Yang, W.; Bowen, C. R.; Yang, Y. Differences and Similarities of Photocatalysis and Electrocatalysis in Two-Dimensional Nanomaterials: Strategies, Traps, Applications and Challenges. *Nano-Micro Lett.* **2021**, *13* (1), 156. https://doi.org/10.1007/s40820-021-00681-9.

(16) Wadia, C.; Alivisatos, A. P.; Kammen, D. M. Materials Availability Expands the Opportunity for Large-Scale Photovoltaics Deployment. *Environ. Sci. Technol.* **2009**, *43* (6), 2072–2077. https://doi.org/10.1021/es8019534.
(17) Velicky, M.; Toth, P. From Two-Dimensional Materials to Their Heterostructures: An Electrochemist's Perspective. *Appl. Mater. Today* **2017**, *8*, 68–103. https://doi.org/10.1016/j.apmt.2017.05.003.
(18) Kang, S.; Lee, D.; Kim, J.; Capasso, A.; Kang, H. S.; Park, J.-W.; Lee, C.-H.; Lee, G.-H. 2D Semiconducting Materials for Electronic and Optoelectronic Applications: Potential and Challenge. *2D Mater.* **2020**, *7* (2), 022003. https://doi.org/10.1088/2053-1583/ab6267.
(19) Liu, X.; Choi, M. S.; Hwang, E.; Yoo, W. J.; Sun, J. Fermi Level Pinning Dependent 2D Semiconductor Devices: Challenges and Prospects. *Adv. Mater.* **2021**, *n/a* (n/a), 2108425. https://doi.org/10.1002/adma.202108425.
(20) Hankin, A.; Bedoya-Lora, F. E.; Alexander, J. C.; Regoutz, A.; Kelsall, G. H. Flat Band Potential Determination: Avoiding the Pitfalls. *J. Mater. Chem. A* **2019**, *7* (45), 26162–26176. https://doi.org/10.1039/C9TA09569A.
(21) Ugeda, M. M.; Bradley, A. J.; Shi, S.-F.; da Jornada, F. H.; Zhang, Y.; Qiu, D. Y.; Ruan, W.; Mo, S.-K.; Hussain, Z.; Shen, Z.-X.; Wang, F.; Louie, S. G.; Crommie, M. F. Giant Bandgap Renormalization and Excitonic Effects in a Monolayer Transition Metal Dichalcogenide Semiconductor. *Nat. Mater.* **2014**, *13* (12), 1091–1095. https://doi.org/10.1038/nmat4061.
(22) Chernikov, A.; Ruppert, C.; Hill, H. M.; Rigosi, A. F.; Heinz, T. F. Population Inversion and Giant Bandgap Renormalization in Atomically Thin WS2 Layers. *Nat. Photonics* **2015**, *9* (7), 466–470. https://doi.org/10.1038/nphoton.2015.104.
(23) Qiu, Z.; Trushin, M.; Fang, H.; Verzhbitskiy, I.; Gao, S.; Laksono, E.; Yang, M.; Lyu, P.; Li, J.; Su, J.; Telychko, M.; Watanabe, K.; Taniguchi, T.; Wu, J.; Neto, A. H. C.; Yang, L.; Eda, G.; Adam, S.; Lu, J. Giant Gate-Tunable Bandgap Renormalization and Excitonic Effects in a 2D Semiconductor. *Sci. Adv.* **2019**, *5* (7), eaaw2347. https://doi.org/10.1126/sciadv.aaw2347.
(24) Jiang, C.; Moniz, S. J. A.; Wang, A.; Zhang, T.; Tang, J. Photoelectrochemical Devices for Solar Water Splitting – Materials and Challenges. *Chem. Soc. Rev.* **2017**, *46* (15), 4645–4660. https://doi.org/10.1039/C6CS00306K.
(25) Sivula, K.; Van De Krol, R. Semiconducting Materials for Photoelectrochemical Energy Conversion. *Nat. Chem.* **2016**, 1–16. https://doi.org/10.1038/natrevmats.2015.10.
(26) Yu, X.; Sivula, K. Toward Large-Area Solar Energy Conversion with Semiconducting 2D Transition Metal Dichalcogenides. *ACS Energy Lett.* **2016**, *1* (1), 315–322. https://doi.org/10.1021/acsenergylett.6b00114.
(27) Sze, S. M.; Li, Y.; Ng, K. K. *Physics of Semiconductor Devices*; John Wiley & Sons, 2021.
(28) Bard, A. J.; Faulkner, L. R. *Electrochemical Methods: Fundamentals and Applications*, 2nd ed.; Wiley: New York, 2001.
(29) Peter, L. M. Dynamic Aspects of Semiconductor Photoelectrochemistry. *Semicond. Photoelectrochem.*
(30) Sze, S. M. *Semiconductor Devices*; Physics and Technology; John Wiley & Sons, 2013.
(31) Thornber, K. K. Relation of Drift Velocity to Low-Field Mobility and High-Field Saturation Velocity. *J. Appl. Phys.* **1980**, *51* (4), 2127. https://doi.org/10.1063/1.327885.
(32) Gerischer, H. Charge Transfer Processes at Semiconductor-Electrolyte Interfaces in Connection with Problems of Catalysis. *Surf. Sci.* **1969**, *18* (1), 97–122.
(33) Spitler, M.; Parkinson, B. A. Efficient Infrared Dye Sensitization of van Der Waals Surfaces of Semiconductor Electrodes. *Langmuir* **1986**, *2* (5), 549–553. https://doi.org/10.1021/la00071a003.
(34) Bard, A. J.; Bocarsly, A. B.; Fan, F. R. F.; Walton, E. G.; Wrighton, M. S. The Concept of Fermi Level Pinning at Semiconductor/Liquid Junctions. Consequences for Energy Conversion Efficiency and Selection of Useful Solution Redox Couples in Solar Devices. *J. Am. Chem. Soc.* **1980**, *102* (11), 3671–3677. https://doi.org/10.1021/ja00531a001.

(35) Bard, A. J.; Wrighton, M. S. Thermodynamic Potential for the Anodic Dissolution of N-Type Semiconductors: A Crucial Factor Controlling Durability and Efficiency in Photoelectrochemical Cells and an Important Criterion in the Selection of New Electrode/Electrolyte Systems. *J. Electrochem. Soc.* **1977**, *124* (11), 1706–1710. https://doi.org/10.1149/1.2133140.

(36) Natan, M. J.; Thackeray, J. W.; Wrighton, M. S. Interaction of Thiols with N-Type Cadmium Sulfide and n-Type Cadmium Selenide in Aqueous Solutions: Adsorption of Thiolate Anion and Efficient Photoelectrochemical Oxidation to Disulfides. *J. Phys. Chem.* **1986**, *90* (17), 4089–4098. https://doi.org/10.1021/j100408a051.

(37) Kautek, W.; Gerischer, H.; Tributsch, H. The Role of Carrier Diffusion and Indirect Optical Transitions in the Photoelectrochemical Behavior of Layer Type D-Band Semiconductors. *J. Electrochem. Soc.* **1980**, *127* (11), 2471–2478. https://doi.org/10.1149/1.2129499.

(38) Tributsch, H.; Bennett, J. C. Electrochemistry and Photochemistry of MoS2 Layer Crystals. *J. Electroanal. Chem.* **1977**, *81*, 97–111.

(39) Tributsch, H. Hole Reactions from D-Energy Bands of Layer Type Group VI Transition Metal Dichalcogenides: New Perspectives for Electrochemical Solar Energy Conversion. *J. Electrochem. Soc.* **1978**, *125* (7), 1086–1093. https://doi.org/10.1149/1.2131625.

(40) Dickinson, R. G.; Pauling, L. The Crystal Structure of Molybdenite. *J. Am. Chem. Soc.* **1923**, *45* (6), 1466–1471. https://doi.org/10.1021/ja01659a020.

(41) Frindt, R. F.; Yoffe, A. D. Physical Properties of Layer Structures : Optical Properties and Photoconductivity of Thin Crystals of Molybdenum Disulphide. *Proc. R. Soc. Lond. Ser. Math. Phys. Sci.* **1963**, *273* (1352), 69–83. https://doi.org/10.1098/rspa.1963.0075.

(42) Zhang, X.; Qiao, X.-F.; Shi, W.; Wu, J.-B.; Jiang, D.-S.; Tan, P.-H. Phonon and Raman Scattering of Two-Dimensional Transition Metal Dichalcogenides from Monolayer, Multilayer to Bulk Material. *Chem. Soc. Rev.* **2015**, *44* (9), 2757–2785. https://doi.org/10.1039/C4CS00282B.

(43) Wilson, J. A.; Yoffe, A. D. The Transition Metal Dichalcogenides Discussion and Interpretation of the Observed Optical, Electrical and Structural Properties. *Adv. Phys.* **1969**, *18* (73), 193–335. https://doi.org/10.1080/00018736900101307.

(44) Connell, G. A. N.; Wilson, J. A.; Yoffe, A. D. Effects of Pressure and Temperature on Exciton Absorption and Band Structure of Layer Crystals: Molybdenum Disulphide. **1969**, 10.

(45) Mattheiss, L. F. Band Structures of Transition-Metal-Dichalcogenide Layer Compounds. *Phys. Rev. B* **1973**, *8* (8), 3719–3740. https://doi.org/10.1103/PhysRevB.8.3719.

(46) Li, T.; Galli, G. Electronic Properties of MoS $_2$ Nanoparticles. *J. Phys. Chem. C* **2007**, *111* (44), 16192–16196. https://doi.org/10.1021/jp075424v.

(47) Splendiani, A.; Sun, L.; Zhang, Y.; Li, T.; Kim, J.; Chim, C.-Y.; Galli, G.; Wang, F. Emerging Photoluminescence in Monolayer MoS $_2$. *Nano Lett.* **2010**, *10* (4), 1271–1275. https://doi.org/10.1021/nl903868w.

(48) Geim, A. K. Graphene: Status and Prospects. *Science* **2009**, *324* (5934), 1530–1534. https://doi.org/10.1126/science.1158877.

(49) Yuan, L.; Huang, L. Exciton Dynamics and Annihilation in WS 2 2D Semiconductors. *Nanoscale* **2015**, *7* (16), 7402–7408. https://doi.org/10.1039/C5NR00383K.

(50) Mak, K. F.; Lee, C.; Hone, J.; Shan, J.; Heinz, T. F. Atomically Thin MoS 2 : A New Direct-Gap Semiconductor. *Phys. Rev. Lett.* **2010**, *105* (13), 136805. https://doi.org/10.1103/PhysRevLett.105.136805.

(51) Wang, H.; Zhang, C.; Rana, F. Ultrafast Dynamics of Defect-Assisted Electron–Hole Recombination in Monolayer MoS $_2$. *Nano Lett.* **2015**, *15* (1), 339–345. https://doi.org/10.1021/nl503636c.

(52) Lee, C.; Yan, H.; Brus, L. E.; Heinz, T. F.; Hone, J.; Ryu, S. Anomalous Lattice Vibrations of Single- and Few-Layer MoS $_2$. *ACS Nano* **2010**, *4* (5), 2695–2700. https://doi.org/10.1021/nn1003937.

(53) Li, H.; Zhang, Q.; Yap, C. C. R.; Tay, B. K.; Edwin, T. H. T.; Olivier, A.; Baillargeat, D. From Bulk to Monolayer MoS2 : Evolution of Raman Scattering. *Adv. Funct. Mater.* **2012**, *22* (7), 1385–1390. https://doi.org/10.1002/adfm.201102111.

(54) Buscema, M.; Steele, G. A.; van der Zant, H. S. J.; Castellanos-Gomez, A. The Effect of the Substrate on the Raman and Photoluminescence Emission of Single-Layer MoS2. *Nano Res.* **2014**, *7* (4), 561–571. https://doi.org/10.1007/s12274-014-0424-0.

(55) Bisquert, J.; Garcia-Belmonte, G.; Fabregat-Santiago, F. Modelling the Electric Potential Distribution in the Dark in Nanoporous Semiconductor Electrodes. *J. Solid State Electrochem.* **1999**, *3* (6), 337–347. https://doi.org/10.1007/s100080050164.

(56) Mak, K. F.; He, K.; Lee, C.; Lee, G. H.; Hone, J.; Heinz, T. F.; Shan, J. Tightly Bound Trions in Monolayer MoS2. *Nat. Mater.* **2013**, *12* (3), 207–211. https://doi.org/10.1038/nmat3505.

(57) Lin, Y.; Ling, X.; Yu, L.; Huang, S.; Hsu, A. L.; Lee, Y.-H.; Kong, J.; Dresselhaus, M. S.; Palacios, T. Dielectric Screening of Excitons and Trions in Single-Layer MoS $_2$. *Nano Lett.* **2014**, *14* (10), 5569–5576. https://doi.org/10.1021/nl501988y.

(58) Zhang, C.; Wang, H.; Chan, W.; Manolatou, C.; Rana, F. Absorption of Light by Excitons and Trions in Monolayers of Metal Dichalcogenide Mo S 2 : Experiments and Theory. *Phys. Rev. B* **2014**, *89* (20), 205436. https://doi.org/10.1103/PhysRevB.89.205436.

(59) Drüppel, M.; Deilmann, T.; Krüger, P.; Rohlfing, M. Diversity of Trion States and Substrate Effects in the Optical Properties of an MoS2 Monolayer. *Nat. Commun.* **2017**, *8* (1), 2117. https://doi.org/10.1038/s41467-017-02286-6.

(60) Castellanos-Gomez, A.; Quereda, J.; van der Meulen, H. P.; Agraït, N.; Rubio-Bollinger, G. Spatially Resolved Optical Absorption Spectroscopy of Single- and Few-Layer MoS $_2$ by Hyperspectral Imaging. *Nanotechnology* **2016**, *27* (11), 115705. https://doi.org/10.1088/0957-4484/27/11/115705.

(61) Tongay, S.; Zhou, J.; Ataca, C.; Liu, J.; Kang, J. S.; Matthews, T. S.; You, L.; Li, J.; Grossman, J. C.; Wu, J. Broad-Range Modulation of Light Emission in Two-Dimensional Semiconductors by Molecular Physisorption Gating. *Nano Lett.* **2013**, *13* (6), 2831–2836. https://doi.org/10.1021/nl4011172.

(62) Liu, B.; Zhao, W.; Ding, Z.; Verzhbitskiy, I.; Li, L.; Lu, J.; Chen, J.; Eda, G.; Loh, K. P. Engineering Bandgaps of Monolayer MoS2 and WS2 on Fluoropolymer Substrates by Electrostatically Tuned Many-Body Effects. *Adv. Mater.* **2016**, *28* (30), 6457–6464. https://doi.org/10.1002/adma.201504876.

(63) Gao, S.; Liang, Y.; Spataru, C. D.; Yang, L. Dynamical Excitonic Effects in Doped Two-Dimensional Semiconductors. *Nano Lett.* **2016**, *16* (9), 5568–5573. https://doi.org/10.1021/acs.nanolett.6b02118.

(64) Carroll, G. M.; Zhang, H.; Dunklin, J. R.; Miller, E. M.; Neale, N. R.; van de Lagemaat, J. Unique Interfacial Thermodynamics of Few-Layer 2D MoS 2for (Photo)Electrochemical Catalysis. *Energy Env. Sci* **2019**, *140*, 441–449. https://doi.org/10.1039/C9EE00513G.

(65) Erdewyk, M. V.; Sambur, J. B. Single Nanoflake Photoelectrochemistry Reveals Intrananoflake Doping Heterogeneity That Explains Ensemble-Level Photoelectrochemical Behavior. *ACS Appl. Mater. Interfaces* **2021**, acsami.1c14928. https://doi.org/10.1021/acsami.1c14928.

(66) Sambur, J. B.; Shepherd, D. P.; Hesari, M.; Van Erdewyk, M.; Choudhary, E.; Chen, P. Correlated Single-Molecule Reaction Imaging and Photocurrent Measurements Reveal Underlying Rate Processes in Photoelectrochemical Water Splitting. *J. Electrochem. Soc.* **2019**, *166* (5), H3286–H3293. https://doi.org/10.1149/2.040195jes.

(67) Gerischer, H.; Ross, D.; Lubke, M. Electrochemistry of N-Type MoSe2: A Comparison of Photocorrosion and Dissolution under High Anodic Bias. *Z. Physickalische Chem.* **1984**, *139* (139), 1–9.

(68) Du, H.; Lin, X.; Xu, Z.; Chu, D. Electric Double-Layer Transistors: A Review of Recent Progress. *J. Mater. Sci.* **2015**, *50* (17), 5641–5673. https://doi.org/10.1007/s10853-015-9121-y.

(69) Costanzo, D.; Jo, S.; Berger, H.; Morpurgo, A. F. Gate-Induced Superconductivity in Atomically Thin MoS2 Crystals. *Nat. Nanotechnol.* **2016**, *11* (4), 339–344. https://doi.org/10.1038/nnano.2015.314.

(70) Bertolazzi, S.; Gobbi, M.; Zhao, Y.; Backes, C.; Samorì, P. Molecular Chemistry Approaches for Tuning the Properties of Two-Dimensional Transition Metal Dichalcogenides. *Chem. Soc. Rev.* **2018**, *47* (17), 6845–6888. https://doi.org/10.1039/C8CS00169C.

(71) Velický, M.; Dryfe, R. A. W. Electrochemistry of 2D Nanomaterials. In *Frontiers of Nanoscience*; Elsevier, 2021; Vol. 18, pp 485–536. https://doi.org/10.1016/B978-0-12-820055-1.00009-5.

(72) Kim, C.-H.; Frisbie, C. D. Field Effect Modulation of Outer-Sphere Electrochemistry at Back-Gated, Ultrathin ZnO Electrodes. *J. Am. Chem. Soc.* **2016**, *138* (23), 7220–7223. https://doi.org/10.1021/jacs.6b02547.

(73) Bediako, D. K.; Rezaee, M.; Yoo, H.; Larson, D. T.; Zhao, S. Y. F.; Taniguchi, T.; Watanabe, K.; Brower-Thomas, T. L.; Kaxiras, E.; Kim, P. Heterointerface Effects in the Electrointercalation of van Der Waals Heterostructures. *Nature* **2018**, *558* (7710), 425–429. https://doi.org/10.1038/s41586-018-0205-0.

(74) Vanmaekelbergh, D.; Houtepen, A. J.; Kelly, J. J. Electrochemical Gating: A Method to Tune and Monitor the (Opto)Electronic Properties of Functional Materials. *Electrochimica Acta* **2007**, *53* (3), 1140–1149. https://doi.org/10.1016/j.electacta.2007.02.045.

(75) Bisri, S. Z.; Shimizu, S.; Nakano, M.; Iwasa, Y. Endeavor of Iontronics: From Fundamentals to Applications of Ion-Controlled Electronics. *Adv. Mater.* **2017**, *29* (25), 1607054. https://doi.org/10.1002/adma.201607054.

(76) Velický, M. Electrolyte versus Dielectric Gating of Two-Dimensional Materials. *J. Phys. Chem. C* **2021**, *125* (40), 21803–21809. https://doi.org/10.1021/acs.jpcc.1c04795.

(77) Carroll, G. M.; Zhang, H.; Dunklin, J. R.; Miller, E. M.; Neale, N. R.; van de Lagemaat, J. Unique Interfacial Thermodynamics of Few-Layer 2D MoS2 for (Photo)Electrochemical Catalysis. *Energy Environ. Sci.* **2019**, *12* (5), 1648–1656. https://doi.org/10.1039/C9EE00513G.

(78) Almaraz, R.; Sayer, T.; Toole, J.; Austin, R.; Farah, Y.; Trainor, N.; Redwing, J. M.; Krummel, A.; Montoya-Castillo, A.; Sambur, J. Quantifying Interfacial Energetics of 2D Semiconductor Electrodes Using in Situ Spectroelectrochemistry and Many-Body Theory. ChemRxiv April 13, 2023. https://doi.org/10.26434/chemrxiv-2023-kl1cv.

(79) Wang, Y.; Kim, C.-H.; Yoo, Y.; Johns, J. E.; Frisbie, C. D. Field Effect Modulation of Heterogeneous Charge Transfer Kinetics at Back-Gated Two-Dimensional MoS $_2$ Electrodes. *Nano Lett.* **2017**, *17* (12), 7586–7592. https://doi.org/10.1021/acs.nanolett.7b03564.

(80) Wang, Y.; Udyavara, S.; Neurock, M.; Frisbie, C. D. Field Effect Modulation of Electrocatalytic Hydrogen Evolution at Back-Gated Two-Dimensional MoS $_2$ Electrodes. *Nano Lett.* **2019**, *19* (9), 6118–6123. https://doi.org/10.1021/acs.nanolett.9b02079.

(81) Kim, C.-H.; Wang, Y.; Frisbie, C. D. Continuous and Reversible Tuning of Electrochemical Reaction Kinetics on Back-Gated 2D Semiconductor Electrodes: Steady-State Analysis Using a Hydrodynamic Method. *Anal. Chem.* **2019**, *91* (2), 1627–1635. https://doi.org/10.1021/acs.analchem.8b05216.

(82) Tributsch, H. Photoelectrochemical Behaviour of Layer-Type Transition Metal Dichalcogenides. *Faraday Discuss. Chem. Soc.* **1980**, *70*, 189–205. https://doi.org/10.1039/DC9807000189.

(83) Coehoorn, R.; Haas, C.; De Groot, R. A. Electronic Structure of MoSe 2 , MoS 2 , and WSe 2 . II. The Nature of the Optical Band Gaps. *Phys. Rev. B* **1987**, *35* (12), 6203–6206. https://doi.org/10.1103/PhysRevB.35.6203.

(84) Bonde, J.; Moses, P. G.; Jaramillo, T. F.; Nørskov, J. K.; Chorkendorff, I. Hydrogen Evolution on Nano-Particulate Transition Metal Sulfides. **2009**, 15.

(85) Ambrosi, A.; Sofer, Z.; Pumera, M. Lithium Intercalation Compound Dramatically Influences the Electrochemical Properties of Exfoliated MoS2. *Small* **2015**, *11* (5), 605–612. https://doi.org/10.1002/smll.201400401.

(86) Mohamad Nasir, M. Z.; Sofer, Z.; Ambrosi, A.; Pumera, M. A Limited Anodic and Cathodic Potential Window of MoS 2 : Limitations in Electrochemical Applications. *Nanoscale* **2015**, *7* (7), 3126–3129. https://doi.org/10.1039/C4NR06899H.

(87) Gerischer, H. Electrolytic Decomposition and Photodecomposition of Compound Semiconductors in Contact with Electrolytes. *J. Vac. Sci. Technol.* **1978**, *15* (4), 1422–1428. https://doi.org/10.1116/1.569800.

(88) Kautek, W.; Gerischer, H. Anisotropic Photocorrosion of N-Type MoS2 MoSe2, and WSe2 Single Crystal Surfaces: The Role of Cleavage Steps, Line and Screw Dislocations. *Surf. Sci.* **1982**, *119* (1), 46–60. https://doi.org/10.1016/0039-6028(82)90186-8.

(89) Bahl, O. P.; Evans, E. L.; Thomas, J. M. The Identification and Some Properties of Point Defects and Non-Basal Dislocations in Molybdenite Surfaces. *Proc. R. Soc. Lond. Ser. Math. Phys. Sci.* **1968**, *306* (1484), 53–65.

(90) Ahmed, S. M.; Gerischer, H. Influence of Crystal Surface Orientation on Redox Reactions at Semiconducting MoS2. *Electrochimica Acta* **1979**, *24* (6), 705–711. https://doi.org/10.1016/0013-4686(79)87055-3.

(91) Jaegermann, W.; Tributsch, H. *Interfacial Properties of Semiconducting Transition Metal Chalcogenides*; 1988.

(92) Tan, S. M.; Ambrosi, A.; Sofer, Z.; Huber, S.; Sedmidubsky, D.; Pumera, M. Pristine Basal- and Edge-Plane-Oriented Molybdenite MoS 2 Exhibiting Highly Anisotropic Properties. *Chem. Eur. J.* **2015**, *21* (19), 7170–7178. https://doi.org/10.1002/chem.201500435.

(93) Jaramillo, T. F.; Jørgensen, K. P.; Bonde, J.; Nielsen, J. H.; Horch, S.; Chorkendorff, I. Identification of Active Edge Sites for Electrochemical H2 Evolution from MoS2 Nanocatalysts. *Science* **2007**, *317* (5834), 100. https://doi.org/10.1126/science.1141483.

(94) Chia, X.; Pumera, M. Characteristics and Performance of Two-Dimensional Materials for Electrocatalysis. *Nat. Catal.* **2018**, *1* (12), 909–921. https://doi.org/10.1038/s41929-018-0181-7.

(95) Li, Z.; Attanayake, N. H.; Blackburn, J. L.; Miller, E. M. Carbon Dioxide and Nitrogen Reduction Reactions Using 2D Transition Metal Dichalcogenide (TMDC) and Carbide/Nitride (MXene) Catalysts. *Energy Environ. Sci.* **2021**, *14* (12), 6242–6286. https://doi.org/10.1039/D1EE03211A.

(96) Joseph, A.; Vijayan, A. S.; Shebeeb, C. M.; Akshay, K. S.; Mathew, K. P. J.; Sajith, V. A Review on Tailoring the Corrosion and Oxidation Properties of MoS2-Based Coatings. *J. Mater. Chem. A* **2023**, *11* (7), 3172–3209. https://doi.org/10.1039/D2TA07821J.

(97) Eng, A. Y. S.; Ambrosi, A.; Sofer, Z.; Šimek, P.; Pumera, M. Electrochemistry of Transition Metal Dichalcogenides: Strong Dependence on the Metal-to-Chalcogen Composition and Exfoliation Method. *ACS Nano* **2014**, *8* (12), 12185–12198. https://doi.org/10.1021/nn503832j.

(98) Sebastian, A.; Zhang, F.; Dodda, A.; May-Rawding, D.; Liu, H.; Zhang, T.; Terrones, M.; Das, S. Electrochemical Polishing of Two-Dimensional Materials. *ACS Nano* **2019**, *13* (1), 78–86. https://doi.org/10.1021/acsnano.8b08216.

(99) Wang, L.; Sambur, J. B. Efficient Ultrathin Liquid Junction Photovoltaics Based on Transition Metal Dichalcogenides. *Nano Lett.* **2019**, *19* (5), 2960–2967. https://doi.org/10.1021/acs.nanolett.9b00070.

(100) KC, S.; Longo, R. C.; Wallace, R. M.; Cho, K. Surface Oxidation Energetics and Kinetics on MoS2 Monolayer. *J. Appl. Phys.* **2015**, *117* (13), 135301. https://doi.org/10.1063/1.4916536.

(101) Wang, Z.; Von Dem Bussche, A.; Qiu, Y.; Valentin, T. M.; Gion, K.; Kane, A. B.; Hurt, R. H. Chemical Dissolution Pathways of MoS $_2$ Nanosheets in Biological and Environmental Media. *Environ. Sci. Technol.* **2016**, *50* (13), 7208–7217. https://doi.org/10.1021/acs.est.6b01881.

(102) Gao, J.; Li, B.; Tan, J.; Chow, P.; Lu, T.-M.; Koratkar, N. Aging of Transition Metal Dichalcogenide Monolayers. *ACS Nano* **2016**, *10* (2), 2628–2635. https://doi.org/10.1021/acsnano.5b07677.

(103) Walter, T. N.; Kwok, F.; Simchi, H.; Aldosari, H. M.; Mohney, S. E. Oxidation and Oxidative Vapor-Phase Etching of Few-Layer MoS2. *J. Vac. Sci. Technol. B* **2017**, *35* (2), 021203. https://doi.org/10.1116/1.4975144.

(104) Zhang, H.; R. Dunklin, J.; G. Reid, O.; Joon Yun, S.; U. Nanayakkara, S.; Hee Lee, Y.; L. Blackburn, J.; M. Miller, E. Disentangling Oxygen and Water Vapor Effects on Optoelectronic Properties of Monolayer Tungsten Disulfide. *Nanoscale* **2020**, *12* (15), 8344–8354. https://doi.org/10.1039/C9NR09326E.

(105) Zhou, H.; Yu, F.; Liu, Y.; Zou, X.; Cong, C.; Qiu, C.; Yu, T.; Yan, Z.; Shen, X.; Sun, L.; Yakobson, B. I.; Tour, J. M. Thickness-Dependent Patterning of MoS2 Sheets with Well-Oriented Triangular Pits by Heating in Air. *Nano Res.* **2013**, *6* (10), 703–711. https://doi.org/10.1007/s12274-013-0346-2.

(106) Feng, J.; Liu, K.; Graf, M.; Lihter, M.; Bulushev, R. D.; Dumcenco, D.; Alexander, D. T. L.; Krasnozhon, D.; Vuletic, T.; Kis, A.; Radenovic, A. Electrochemical Reaction in Single Layer MoS $_2$: Nanopores Opened Atom by Atom. *Nano Lett.* **2015**, *15* (5), 3431–3438. https://doi.org/10.1021/acs.nanolett.5b00768.

(107) You, X.; Liu, N.; Lee, C. J.; Pak, J. J. An Electrochemical Route to MoS2 Nanosheets for Device Applications. *Mater. Lett.* **2014**, *121*, 31–35. https://doi.org/10.1016/j.matlet.2014.01.052.

(108) Liu, N.; Kim, P.; Kim, J. H.; Ye, J. H.; Kim, S.; Lee, C. J. Large-Area Atomically Thin MoS $_2$ Nanosheets Prepared Using Electrochemical Exfoliation. *ACS Nano* **2014**, *8* (7), 6902–6910. https://doi.org/10.1021/nn5016242.

(109) Das, S.; Bera, M. K.; Tong, S.; Narayanan, B.; Kamath, G.; Mane, A.; Paulikas, A. P.; Antonio, M. R.; Sankaranarayanan, S. K. R. S.; Roelofs, A. K. A Self-Limiting Electro-Ablation Technique for the Top-Down Synthesis of Large-Area Monolayer Flakes of 2D Materials. *Sci. Rep.* **2016**, *6* (1), 28195. https://doi.org/10.1038/srep28195.

(110) Huang, Y.-T.; Dodda, A.; Schulman, D. S.; Sebastian, A.; Zhang, F.; Buzzell, D.; Terrones, M.; Feng, S.-P.; Das, S. Anomalous Corrosion of Bulk Transition Metal Diselenides Leading to Stable Monolayers. *ACS Appl. Mater. Interfaces* **2017**, *9* (44), 39059–39068. https://doi.org/10.1021/acsami.7b13107.

(111) Kumar, A.; Sebastian, A.; Das, S.; Ringe, E. In Situ Optical Tracking of Electroablation in Two-Dimensional Transition-Metal Dichalcogenides. *ACS Appl. Mater. Interfaces* **2018**, *10* (47), 40773–40780. https://doi.org/10.1021/acsami.8b14585.

(112) Schulman, D. S.; Sebastian, A.; Buzzell, D.; Huang, Y.-T.; Arnold, A. J.; Das, S. Facile Electrochemical Synthesis of 2D Monolayers for High-Performance Thin-Film Transistors. *ACS Appl. Mater. Interfaces* **2017**, *9* (51), 44617–44624. https://doi.org/10.1021/acsami.7b14711.

(113) Schulman, D. S.; May-Rawding, D.; Zhang, F.; Buzzell, D.; Alem, N.; Das, S. Superior Electro-Oxidation and Corrosion Resistance of Monolayer Transition Metal Disulfides. *ACS Appl. Mater. Interfaces* **2018**, *10* (4), 4285–4294. https://doi.org/10.1021/acsami.7b17660.

(114) Todt, M. A.; Isenberg, A. E.; Nanayakkara, S. U.; Miller, E. M.; Sambur, J. B. Single-Nanoflake Photo-Electrochemistry Reveals Champion and Spectator Flakes in Exfoliated MoSe $_2$ Films. *J. Phys. Chem. C* **2018**, *122* (12), 6539–6545. https://doi.org/10.1021/acs.jpcc.7b12715.

(115) Canny, J. A Computational Approach to Edge Detection. *IEEE Trans. Pattern Anal. Mach. Intell.* **1986**, *PAMI-8* (6), 679–698. https://doi.org/10.1109/TPAMI.1986.4767851.

(116) Erdewyk, M. V.; Sambur, J. B. Single Nanoflake Photoelectrochemistry Reveals Intrananoflake Doping Heterogeneity That Explains Ensemble-Level Photoelectrochemical Behavior. *ACS Appl. Mater. Interfaces* **2022**, *14* (20), 22737–22746. https://doi.org/10.1021/acsami.1c14928.

(117) Lévy-Clément, C.; Tenne, R. Modification of Surface Properties of Layered Compounds by Chemical and (Photo)Electrochemical Processes. In *Photoelectrochemistry and Photovoltaics of Layered Semiconductors*; Aruchamy, A., Ed.; Physics and Chemistry of Materials with Low-Dimensional Structures; Springer Netherlands: Dordrecht, 1992; pp 155–194. https://doi.org/10.1007/978-94-015-1301-2_4.

(118) Menezes, S.; Schneemeyer, L. F.; Lewerenz, H. J. Efficiency Losses from Carrier-type Inhomogeneity in Tungsten Diselenide Photoelectrodes. *Appl. Phys. Lett.* **1981**, *38* (11), 949–951. https://doi.org/10/bpmvbx.

(119) Hill, J. W.; Hill, C. M. H. Directly Mapping Photoelectrochemical Behavior within Individual Transition Metal Dichalcogenide Nanosheets. *Nano Lett.* **2019**, *19* (8), 1–7. https://doi.org/10.1021/acs.nanolett.9b02336.

(120) Tolbert, C. L.; Hill, C. M. Electrochemically Probing Exciton Transport in Monolayers of Two-Dimensional Semiconductors. *Faraday Discuss.* **2022**, *233* (0), 163–174. https://doi.org/10.1039/D1FD00052G.

(121) Gerischer, H.; Mindt, W. The Mechanisms of the Decomposition of Semiconductors by Electrochemical Oxidation and Reduction. *Electrochimica Acta* **1968**, *13* (6), 1329–1341. https://doi.org/10.1016/0013-4686(68)80060-X.

(122) Armstrong, N. R.; Lin, A. W. C.; Fujihira, Masamichi.; Kuwana, Theodore. Electrochemical and Surface Characteristics of Tin Oxide and Indium Oxide Electrodes. *Anal. Chem.* **1976**, *48* (4), 741–750. https://doi.org/10.1021/ac60368a035.

(123) Benck, J. D.; Pinaud, B. A.; Gorlin, Y.; Jaramillo, T. F. Substrate Selection for Fundamental Studies of Electrocatalysts and Photoelectrodes: Inert Potential Windows in Acidic, Neutral, and Basic Electrolyte. *PLoS ONE* **2014**, *9* (10), e107942. https://doi.org/10.1371/journal.pone.0107942.

(124) Padilha, J. E.; Peelaers, H.; Janotti, A.; Van de Walle, C. G. Nature and Evolution of the Band-Edge States in MoS 2 : From Monolayer to Bulk. *Phys. Rev. B* **2014**, *90* (20), 205420. https://doi.org/10.1103/PhysRevB.90.205420.

(125) Brunet Cabré, M.; Paiva, A. E.; Velický, M.; Colavita, P. E.; McKelvey, K. Electrochemical Kinetics as a Function of Transition Metal Dichalcogenide Thickness. *Electrochimica Acta* **2021**, *393*, 139027. https://doi.org/10.1016/j.electacta.2021.139027.

(126) Das, S. K.; Gawas, R.; Chakrabarty, S.; Harini, G.; Patidar, R.; Jasuja, K. An Unexpected Transformation of Organic Solvents into 2D Fluorescent Quantum Dots during Ultrasonication-Assisted Liquid-Phase Exfoliation. *J. Phys. Chem. C* **2019**, *123* (41), 25412–25421. https://doi.org/10.1021/acs.jpcc.9b03975.

(127) Martincová, J.; Otyepka, M.; Lazar, P. Is Single Layer MoS2 Stable in the Air? *Chem. – Eur. J.* **2017**, *23* (53), 13233–13239. https://doi.org/10.1002/chem.201702860.

(128) Nozik, A. J.; Boudreaux, D. S.; Chance, R. R.; WILLIAMS, F. Charge Transfer at Illuminated Semiconductor-Electrolyte Interfaces. *Interfacial Photoprocesses Energy Convers. Synth.* **1980**, *184*, 155–171. https://doi.org/10.1021/ba-1980-0184.ch009.

(129) Boudreaux, D. S.; WILLIAMS, F.; Nozik, A. J. Hot Carrier Injection at Semiconductor-Electrolyte Junctions. *J. Appl. Phys.* **1980**, *51* (4), 2158. https://doi.org/10.1063/1.327889.

(130) Cooper, G.; Turner, J. A.; Parkinson, B. A.; Nozik, A. J. Hot Carrier Injection of Photogenerated Electrons at Indium Phosphide–Electrolyte Interfaces. *J. Appl. Phys.* **1983**, *54* (11), 6463. https://doi.org/10.1063/1.331928.

(131) Bard, A. J.; Faulkner, L. R. Kinetics of Electrode Reactions. In *Electrochemical Methods: Fundamentals and Applications*; John Wiley & Sons, Inc.: New York, 2001; pp 87–134.

(132) Gerischer, H. Semiconductor Electrochemistry. In *Physical Chemstry: An Advanced Treatise*; Eyring, H., Henderson, D., Jost, W., Eds.; Academic: New York, 1970; Vol. IXA.

(133) Marcus, R. A. Chemical and Electrochemical Electron-Transfer Theory. *Annu. Rev. Phys. Chem.* **1964**, *15* (1), 155–196. https://doi.org/10.1146/annurev.pc.15.100164.001103.

(134) Fajardo, A. M.; Lewis, N. S. Free-Energy Dependence of Electron-Transfer Rate Constants at Si/Liquid Interfaces. *J Phys Chem B* **1997**, *101* (51), 11136–11151. https://doi.org/10.1021/jp972087p.

(135) Hamann, T. W.; Gstrein, F.; Brunschwig, B. S.; Lewis, N. S. Measurement of the Free-Energy Dependence of Interfacial Charge-Transfer Rate Constants Using ZnO/H 2O Semiconductor/Liquid Contacts. **2005**, *127* (21), 7815–7824. https://doi.org/10.1021/ja0436188.

(136) Hamann, T. W.; Gstrein, F.; Brunschwig, B. S.; Lewis, N. S. Measurement of the Driving Force Dependence of Interfacial Charge-Transfer Rate Constants in Response to PH Changes at n-ZnO/H2O Interfaces. *Chem. Phys.* **2006**, *326* (1), 15–23. https://doi.org/10.1016/j.chemphys.2006.02.027.

(137) Nguyen, P. V.; Teutsch, N. C.; Wilson, N. P.; Kahn, J.; Xia, X.; Graham, A. J.; Kandyba, V.; Giampietri, A.; Barinov, A.; Constantinescu, G. C.; Yeung, N.; Hine, N. D. M.; Xu, X.; Cobden, D. H.; Wilson, N. R. Visualizing Electrostatic Gating Effects in Two-Dimensional Heterostructures. *Nature* **2019**, *572* (7768), 220–223. https://doi.org/10.1038/s41586-019-1402-1.

(138) Park, Y.; Wook Han, S.; S. Chan, C. C.; L. Reid, B. P.; A. Taylor, R.; Kim, N.; Jo, Y.; Im, H.; S. Kim, K. Interplay between Many Body Effects and Coulomb Screening in the Optical Bandgap of Atomically Thin MoS 2. *Nanoscale* **2017**, *9* (30), 10647–10652. https://doi.org/10.1039/C7NR01834G.

(139) Liu, F.; Ziffer, M. E.; Hansen, K. R.; Wang, J.; Zhu, X. Direct Determination of Band-Gap Renormalization in the Photoexcited Monolayer MoS 2. *Phys. Rev. Lett.* **2019**, *122* (24), 246803. https://doi.org/10.1103/PhysRevLett.122.246803.

(140) Liu, B.; Zhao, W.; Ding, Z.; Verzhbitskiy, I.; Li, L.; Lu, J.; Chen, J.; Eda, G.; Loh, K. P. Engineering Bandgaps of Monolayer MoS 2and WS 2on Fluoropolymer Substrates by Electrostatically Tuned Many-Body Effects. *Adv. Mater.* **2016**, *28* (30), 6457–6464. https://doi.org/10.1002/adma.201504876.

(141) Sie, E. J.; Frenzel, A. J.; Lee, Y.-H.; Kong, J.; Gedik, N. Intervalley Biexcitons and Many-Body Effects in Monolayer MoS2. *Phys Rev B* **2015**, *92*, 125417. https://doi.org/10.1103/PhysRevB.92.125417.

(142) Yu, Y.; Dang, J.; Qian, C.; Sun, S.; Peng, K.; Xie, X.; Wu, S.; Song, F.; Yang, J.; Xiao, S.; Yang, L.; Wang, Y.; Shan, X.; Rafiq, M. A.; Li, B.-B.; Xu, X. Many-Body Effect of Mesoscopic Localized States in ${\mathrm{MoS}}_{2}$ Monolayer. *Phys. Rev. Mater.* **2019**, *3* (5), 051001. https://doi.org/10.1103/PhysRevMaterials.3.051001.

(143) Qiu, D. Y.; da Jornada, F. H.; Louie, S. G. Optical Spectrum of MoS2: Many-Body Effects and Diversity of Exciton States. *Phys. Rev. Lett.* **2013**, *111* (21), 216805. https://doi.org/10.1103/PhysRevLett.111.216805.

(144) Lin, T. N.; Santiago, S. R. M.; Caigas, S. P.; Yuan, C. T.; Lin, T. Y.; Shen, J. L.; Chen, Y. F. Many-Body Effects in Doped WS2 Monolayer Quantum Disks at Room Temperature. *Npj 2D Mater. Appl.* **2019**, *3* (1), 46. https://doi.org/10.1038/s41699-019-0129-z.

(145) Chernikov, A.; van der Zande, A. M.; Hill, H. M.; Rigosi, A. F.; Velauthapillai, A.; Hone, J.; Heinz, T. F. Electrical Tuning of Exciton Binding Energies in Monolayer WS2. *Phys. Rev. Lett.* **2015**, *115* (12), 126802–126806. https://doi.org/10.1103/PhysRevLett.115.126802.

(146) Yao, K.; Yan, A.; Kahn, S.; Suslu, A.; Liang, Y.; Barnard, E. S.; Tongay, S.; Zettl, A.; Borys, N. J.; Schuck, P. J. Optically Discriminating Carrier-Induced Quasiparticle Band Gap and Exciton Energy Renormalization in Monolayer MoS2. *Phys. Rev. Lett.* **2017**, *119* (8), 087401–087406. https://doi.org/10.1103/PhysRevLett.119.087401.

(147) Efimkin, D. K.; MacDonald, A. H. Many-Body Theory of Trion Absorption Features in Two-Dimensional Semiconductors. *Phys. Rev. B* **2017**, *95* (3), 035417. https://doi.org/10.1103/PhysRevB.95.035417.

(148) Kuc, A.; Heine, T. The Electronic Structure Calculations of Two-Dimensional Transition-Metal Dichalcogenides in the Presence of External Electric and Magnetic Fields. *Chem. Soc. Rev.* **2015**, *44* (9), 2603–2614. https://doi.org/10.1039/C4CS00276H.

(149) Lewis, N. S. An Analysis of Charge Transfer Rate Constants for Semiconductor/Liquid Interfaces. *Annu. Rev. Phys. Chem.* **1991**, *42* (1), 543–580.

(150) Cardon, F.; Gomes, W. P. On the Determination of the Flat-Band Potential of a Semiconductor in Contact with a Metal or an Electrolyte from the Mott-Schottky Plot. *J. Phys. Appl. Phys.* **1978**, *11* (4), L63–L67. https://doi.org/10.1088/0022-3727/11/4/003.

(151) MEMMING, R.; Schwandt, G. Potential and Charge Distribution at Semiconductor-Electrolyte Interfaces. *Angew. Chem. Int. Ed Engl.* **1967**, *6* (10), 851–861.

(152) Butler, M. A. Photoelectrolysis and Physical Properties of the Semiconducting Electrode WO3. *J. Appl. Phys.* **1977**, *48* (5), 1914. https://doi.org/10.1063/1.323948.

(153) Chaves, A.; Azadani, J. G.; Alsalman, H.; da Costa, D. R.; Frisenda, R.; Chaves, A. J.; Song, S. H.; Kim, Y. D.; He, D.; Zhou, J.; Castellanos-Gomez, A.; Peeters, F. M.; Liu, Z.; Hinkle, C. L.; Oh, S.-H.; Ye, P. D.; Koester, S. J.; Lee, Y. H.; Avouris, Ph.; Wang, X.; Low, T. Bandgap Engineering of Two-Dimensional Semiconductor Materials. *Npj 2D Mater. Appl.* **2020**, *4* (1), 29. https://doi.org/10.1038/s41699-020-00162-4.

(154) Padilha, J. E.; Peelaers, H.; Janotti, A.; Van de Walle, C. G. Nature and Evolution of the Band-Edge States in ${\mathrm{MoS}}_{2}$: From Monolayer to Bulk. *Phys. Rev. B* **2014**, *90* (20), 205420. https://doi.org/10.1103/PhysRevB.90.205420.

(155) Bampoulis, P.; van Bremen, R.; Yao, Q.; Poelsema, B.; Zandvliet, H. J. W.; Sotthewes, K. Defect Dominated Charge Transport and Fermi Level Pinning in MoS $_2$ /Metal Contacts. *ACS Appl. Mater. Interfaces* **2017**, *9* (22), 19278–19286. https://doi.org/10.1021/acsami.7b02739.

(156) Sebastian, A.; Pendurthi, R.; Choudhury, T. H.; Redwing, J. M.; Das, S. Benchmarking Monolayer MoS2 and WS2 Field-Effect Transistors. *Nat. Commun.* **2021**, *12* (1), 693. https://doi.org/10.1038/s41467-020-20732-w.

(157) Zhang, F.; Erb, C.; Runkle, L.; Zhang, X.; Alem, N. Etchant-Free Transfer of 2D Nanostructures. *Nanotechnology* **2017**, *29* (2), 025602. https://doi.org/10.1088/1361-6528/aa9c21.

(158) Castellanos-Gomez, A.; Roldán, R.; Cappelluti, E.; Buscema, M.; Guinea, F.; van der Zant, H. S. J.; Steele, G. A. Local Strain Engineering in Atomically Thin MoS $_2$. *Nano Lett.* **2013**, *13* (11), 5361–5366. https://doi.org/10.1021/nl402875m.

(159) Mignuzzi, S.; Pollard, A. J.; Bonini, N.; Brennan, B.; Gilmore, I. S.; Pimenta, M. A.; Richards, D.; Roy, D. Effect of Disorder on Raman Scattering of Single-Layer Mo S 2. *Phys. Rev. B* **2015**, *91* (19), 195411. https://doi.org/10.1103/PhysRevB.91.195411.

(160) McDonnell, S.; Addou, R.; Buie, C.; Wallace, R. M.; Hinkle, C. L. Defect-Dominated Doping and Contact Resistance in MoS $_2$. *ACS Nano* **2014**, *8* (3), 2880–2888. https://doi.org/10.1021/nn500044q.

(161) Niu, Y.; Gonzalez-Abad, S.; Frisenda, R.; Marauhn, P.; Drüppel, M.; Gant, P.; Schmidt, R.; Taghavi, N.; Barcons, D.; Molina-Mendoza, A.; de Vasconcellos, S.; Bratschitsch, R.; Perez De Lara, D.; Rohlfing, M.; Castellanos-Gomez, A. Thickness-Dependent Differential Reflectance Spectra of Monolayer and Few-Layer MoS2, MoSe2, WS2 and WSe2. *Nanomaterials* **2018**, *8* (9), 725. https://doi.org/10.3390/nano8090725.

(162) Borys, N. J.; Barnard, E. S.; Gao, S.; Yao, K.; Bao, W.; Buyanin, A.; Zhang, Y.; Tongay, S.; Ko, C.; Suh, J.; Weber-Bargioni, A.; Wu, J.; Yang, L.; Schuck, P. J. Anomalous Above-Gap Photoexcitations and Optical Signatures of Localized Charge Puddles in Monolayer Molybdenum Disulfide. *ACS Nano* **2017**, *11* (2), 2115–2123. https://doi.org/10.1021/acsnano.6b08278.

(163) Wurst, K.; Strolka, O.; Lauth, J.; Scheele, M. *Electronic Structure of Colloidal 2H-MoS2 Mono- and Bilayers Determined by Spectroelectrochemistry*; preprint; Chemistry, 2022. https://doi.org/10.26434/chemrxiv-2022-1hc2j.

(164) Chang, Y.-W.; Reichman, D. R. Many-Body Theory of Optical Absorption in Doped Two-Dimensional Semiconductors. *Phys. Rev. B* **2019**, *99* (12), 125421. https://doi.org/10.1103/PhysRevB.99.125421.

(165) Kang, K.; Xie, S.; Huang, L.; Han, Y.; Huang, P. Y.; Mak, K. F.; Kim, C.-J.; Muller, D.; Park, J. High-Mobility Three-Atom-Thick Semiconducting Films with Wafer-Scale Homogeneity. *Nature* **2015**, *520* (7549), 656–660. https://doi.org/10.1038/nature14417.

(166) Radisavljevic, B.; Radenovic, A.; Brivio, J.; Giacometti, V.; Kis, A. Single-Layer MoS2 Transistors. *Nat. Nanotechnol.* **2011**, *6* (3), 147–150. https://doi.org/10.1038/nnano.2010.279.

(167) Astakhov, G. V.; Kochereshko, V. P.; Yakovlev, D. R.; Ossau, W.; Nürnberger, J.; Faschinger, W.; Landwehr, G. Oscillator Strength of Trion States in ZnSe-Based Quantum Wells. *Phys. Rev. B* **2000**, *62* (15), 10345–10352. https://doi.org/10.1103/PhysRevB.62.10345.

(168) Huang, D.; Chyi, J.-I.; Morkoç, H. Carrier Effects on the Excitonic Absorption in GaAs Quantum-Well Structures: Phase-Space Filling. *Phys. Rev. B* **1990**, *42* (8), 5147–5153. https://doi.org/10.1103/PhysRevB.42.5147.

(169) Cheiwchanchamnangij, T.; Lambrecht, W. R. L. Quasiparticle Band Structure Calculation of Monolayer, Bilayer, and Bulk MoS 2. *Phys. Rev. B* **2012**, *85* (20), 205302. https://doi.org/10.1103/PhysRevB.85.205302.

(170) McDonnell, S. J.; Wallace, R. M. Atomically-Thin Layered Films for Device Applications Based upon 2D TMDC Materials. *Thin Solid Films* **2016**, *616*, 482–501. https://doi.org/10.1016/j.tsf.2016.08.068.

(171) Cheng, L.; Zhang, C.; Liu, Y. Why Two-Dimensional Semiconductors Generally Have Low Electron Mobility. *Phys. Rev. Lett.* **2020**, *125* (17), 177701. https://doi.org/10.1103/PhysRevLett.125.177701.

(172) Daniels, I. N.; Wang, Z.; Laird, B. B. Dielectric Properties of Organic Solvents in an Electric Field. *J. Phys. Chem. C* **2017**, *121* (2), 1025–1031. https://doi.org/10.1021/acs.jpcc.6b10896.

(173) Zhu, X.; Monahan, N. R.; Gong, Z.; Zhu, H.; Williams, K. W.; Nelson, C. A. Charge Transfer Excitons at van Der Waals Interfaces. *J. Am. Chem. Soc.* **2015**, *137* (26), 8313–8320. https://doi.org/10.1021/jacs.5b03141.

(174) Schulman, D. S.; Arnold, A. J.; Das, S. Contact Engineering for 2D Materials and Devices. *Chem. Soc. Rev.* **2018**, *47* (9), 3037–3058. https://doi.org/10.1039/C7CS00828G.

(175) Bussolotti, F.; Yang, J.; Kawai, H.; Wong, C. P. Y.; Goh, K. E. J. Impact of S-Vacancies on the Charge Injection Barrier at the Electrical Contact with the MoS $_2$ Monolayer. *ACS Nano* **2021**, *15* (2), 2686–2697. https://doi.org/10.1021/acsnano.0c07982.

(176) Pogna, E. A. A.; Marsili, M.; De Fazio, D.; Dal Conte, S.; Manzoni, C.; Sangalli, D.; Yoon, D.; Lombardo, A.; Ferrari, A. C.; Marini, A.; Cerullo, G.; Prezzi, D. Photo-Induced Bandgap Renormalization Governs the Ultrafast Response of Single-Layer MoS $_2$. *ACS Nano* **2016**, *10* (1), 1182–1188. https://doi.org/10.1021/acsnano.5b06488.

(177) Mao, N.; Chen, Y.; Liu, D.; Zhang, J.; Xie, L. Solvatochromic Effect on the Photoluminescence of MoS2 Monolayers. *Small* **2013**, *9* (8), 1312–1315. https://doi.org/10.1002/smll.201202982.

(178) Chakraborty, B.; Bera, A.; Muthu, D. V. S.; Bhowmick, S.; Waghmare, U. V.; Sood, A. K. Symmetry-Dependent Phonon Renormalization in Monolayer MoS 2 Transistor. *Phys. Rev. B* **2012**, *85* (16), 161403. https://doi.org/10.1103/PhysRevB.85.161403.

(179) Liang, Y.; Yang, L. Carrier Plasmon Induced Nonlinear Band Gap Renormalization in Two-Dimensional Semiconductors. *Phys. Rev. Lett.* **2015**, *114* (6), 063001. https://doi.org/10.1103/PhysRevLett.114.063001.

(180) Gao, S.; Yang, L. Renormalization of the Quasiparticle Band Gap in Doped Two-Dimensional Materials from Many-Body Calculations. *Phys. Rev. B* **2017**, *96* (15), 155410. https://doi.org/10.1103/PhysRevB.96.155410.

(181) Ross, J. S.; Wu, S.; Yu, H.; Ghimire, N. J.; Jones, A. M.; Aivazian, G.; Yan, J.; Mandrus, D. G.; Xiao, D.; Yao, W.; Xu, X. Electrical Control of Neutral and Charged Excitons in a Monolayer Semiconductor. *Nat. Commun.* **2013**, *4* (1), 1474. https://doi.org/10.1038/ncomms2498.

(182) Mouri, S.; Miyauchi, Y.; Matsuda, K. Tunable Photoluminescence of Monolayer MoS $_2$ via Chemical Doping. *Nano Lett.* **2013**, *13* (12), 5944–5948. https://doi.org/10.1021/nl403036h.

(183) Tongay, S.; Fan, W.; Kang, J.; Park, J.; Koldemir, U.; Suh, J.; Narang, D. S.; Liu, K.; Ji, J.; Li, J.; Sinclair, R.; Wu, J. Tuning Interlayer Coupling in Large-Area Heterostructures with CVD-Grown MoS2 and WS2 Monolayers. *Nano Lett.* **2014**, *14* (6), 3185–3190. https://doi.org/10.1021/nl500515q.

(184) Kiriya, D.; Tosun, M.; Zhao, P.; Kang, J. S.; Javey, A. Air-Stable Surface Charge Transfer Doping of MoS2 by Benzyl Viologen. *J. Am. Chem. Soc.* **2014**, *136* (22), 7853–7856. https://doi.org/10.1021/ja5033327.

(185) Cai, Y.; Zhou, H.; Zhang, G.; Zhang, Y.-W. Modulating Carrier Density and Transport Properties of MoS2 by Organic Molecular Doping and Defect Engineering. *Chem. Mater.* **2016**, *28* (23), 8611–8621. https://doi.org/10.1021/acs.chemmater.6b03539.

(186) Baglio, J. A.; Calabrese, G. S.; Harrison, D. J.; Kamieniecki, E.; Ricco, A. J.; Wrighton, M. S.; Zoski, G. D. Electrochemical Characterization of P-Type Semiconducting Tungsten Disulfide Photocathodes: Efficient Photoreduction Processes at Semiconductor/Liquid Electrolyte Interfaces. *J. Am. Chem. Soc.* **1983**, *105* (8), 2246–2256. https://doi.org/10.1021/ja00346a024.

(187) Astruc, D. Why Is Ferrocene so Exceptional? *Eur. J. Inorg. Chem.* **2017**, *2017* (1), 6–29. https://doi.org/10.1002/ejic.201600983.

(188) Erdewyk, M. V.; Sambur, J. B. Molecular Reaction Imaging of a Surface Recombination Process Explains Performance Variation Among Smooth MoS $_2$ Photoelectrodes. *J. Electrochem. Soc.* **2022**, *169* (9), 096519. https://doi.org/10.1149/1945-7111/ac94a8.

(189) Daviddi, E.; Gonos, K. L.; Colburn, A. W.; Bentley, C. L.; Unwin, P. R. Scanning Electrochemical Cell Microscopy (SECCM) Chronopotentiometry: Development and Applications in Electroanalysis

and Electrocatalysis. *Anal. Chem.* **2019**, *91* (14), 9229–9237. https://doi.org/10.1021/acs.analchem.9b02091.

(190) Ebejer, N.; Güell, A. G.; Lai, S. C. S.; McKelvey, K.; Snowden, M. E.; Unwin, P. R. Scanning Electrochemical Cell Microscopy: A Versatile Technique for Nanoscale Electrochemistry and Functional Imaging. *Annu. Rev. Anal. Chem. Palo Alto Calif* **2013**, *6* (1), 329–351. https://doi.org/10.1146/annurev-anchem-062012-092650.

(191) Bentley, C. L.; Kang, M.; Unwin, P. R. Scanning Electrochemical Cell Microscopy (SECCM) in Aprotic Solvents: Practical Considerations and Applications. *Anal. Chem.* **2020**, *92* (17), 11673–11680. https://doi.org/10.1021/acs.analchem.0c01540.

(192) Tsierkezos, N. G.; Ritter, U. Electrochemical Impedance Spectroscopy and Cyclic Voltammetry of Ferrocene in Acetonitrile/Acetone System. *J. Appl. Electrochem.* **2010**, *40* (2), 409–417. https://doi.org/10.1007/s10800-009-0011-3.

(193) Pavlishchuk, V. V.; Addison, A. W. Conversion Constants for Redox Potentials Measured versus Different Reference Electrodes in Acetonitrile Solutions at 25°C. *Inorganica Chim. Acta* **2000**, *298* (1), 97–102. https://doi.org/10.1016/S0020-1693(99)00407-7.

APPENDICES

A – Division of Work

For Chapter 3, Justin Toole performed the experimental investigation, data analysis, and MATLAB code development. Justin Toole and Justin Sambur contributed equally to experimental design, data interpretation, and authorship.

For Chapter 4, all experiments were designed and executed by Justin Toole unless otherwise stated below. Data processing occurred using custom MATLAB script adapted from Justin Sambur and Michael Van Erdewyk. The experimental approach for Chapter 4 was originally developed by Justin Sambur. Justin Sambur was the primary author of Chapter 4, and Justin Toole is the primary author for all other work. Rafael Almaraz synthesized and transferred all ML-MoS_2 samples. Justin Toole, Rafael Almaraz, and Justin Sambur contributed equally to figures. MND Modeling was entirely conducted by Thomas Sayer at University of Colorado-Boulder. The preliminary absorbance data of MoS_2 in aqueous electrolyte solutions was measured by Rafael Almaraz.

B – Supplemental Information

B.1 Converting Reference Potential to NHE and Vacuum Energy Scales

All experimental data was acquired versus the Ag quasi reference electrode (QRE). To convert measured potentials to other common reference scales, we determined the formal potential ($E^{\circ\prime}$) of a common redox couple using our QRE and a commercial non-aqueous fritted Ag wire / 0.01 *M* $AgNO_3$ electrode (CHI #112). To do so, we measured cyclic voltammograms of ferrocene/ferrocenium (Fc/Fc^+) versus the same

Ag QRE as in the flow cell but using clean, polished Pt discs (CHI #102) as working and counter electrodes. We measured cyclic voltammograms in the same dry, air-free 0.25 *M* NBu_4PF_6 acetonitrile electrolyte. We calculate $E^{\circ\prime}$ from $E_{1/2}$ values, $0.5(E_{p,a} + E_{p,c})$, where $E_{p,a}$ and $E_{p,c}$ are the anodic and cathodic peak potentials. Here we assume the diffusion coefficients of the oxidized and reduced species are equal ($D_{Fc} = D_{Fc^+}$) (Wang/Compton, 2010). Then, we measured the $E^{\circ\prime}$ of Fc/Fc^+ versus commercial non-aqueous fritted Ag wire / 0.01 *M* $AgNO_3$ electrode using the same approach (see blue dashed line in Fig. B.1**Error! Reference source not found.**). The respective current peak splitting (ΔE_p) is 68 mV for both references. Our measured $E^{\circ\prime}_{Fc/Fc+}$ versus the 0.01 *M* $AgNO_3$ / Ag reference electrode is +0.056 V, which agrees with literature.[186,192] Our measured $E^{\circ\prime}_{Fc/Fc+}$ versus the Ag QRE is +0.106 V. Thus, the potential conversion from our Ag QRE to this standard Ag/$AgNO_3$ reference is −0.050 V (Equation B1 below). The potential scale conversion to the NHE scale from Ag/$AgNO_3$ reference in this solution is +0.548 V Equation B2.[193] Therefore, we sum Equation B1 and Equation B2 to yield the total conversion of +0.498 V from our measured Ag QRE to NHE scale (Equation B3):

$$\text{E (V vs 0.01 } M \text{ AgNO}_3 \text{ / Ag)} = \text{E (V vs Ag QRE)} - 0.050 \text{ V} \qquad \text{(B1)}$$

$$\text{E (V vs NHE)} = \text{E (V vs 0.01 } M \text{ AgNO}_3 \text{ / Ag)} + 0.548 \text{ V} \qquad \text{(B2)}$$

$$\text{E (V vs NHE)} = \text{E (V vs Ag QRE)} + 0.498 \text{ V} \qquad \text{(B3)}$$

Combining Equation B1 and Equation B2 we use Equation B3 to convert our measured V_{app} vs Ag to the NHE and vacuum scales.[131,193]

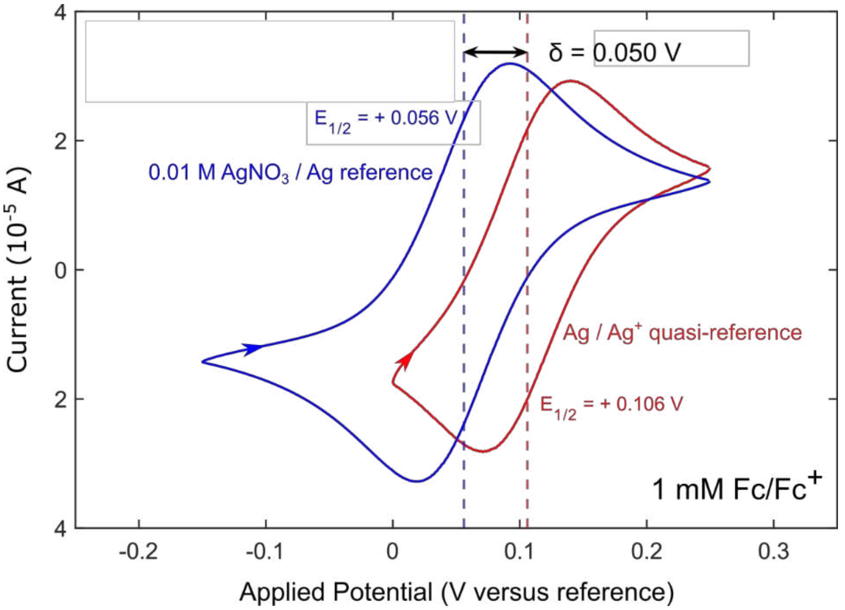

Fig. B.1 – Cyclic voltammograms of 1 mM ferrocene/ferrocenium in 0.25 M NBu_4PF_6 in MeCN vs Ag wire quasi-reference (red trace, right) and standard non-aqueous Ag / 0.01 *M* $AgNO_3$ fritted reference (blue trace, left). The scan rate is 100 mV/s. The working and counter electrode geometric surface area is 0.07 cm^2.

B.2 Additional Example Transmission Images of MoS_2

Representative bright field transmission images of the ML-MoS_2 sample in on ITO-coated glass substrates contrast the thickness (i.e. optical density), relative sizes, and shapes of the mechanically exfoliated and MOCVD-grown MoS_2. In Fig. B.2A-C are mechanically exfoliated natural MoS_2 crystals (SPI), and Fig. B.2D-F are much larger and mostly pristine ML MoS_2 sheets. The MOCVD ML sheets are encapsulated inside a 3-electrode electrochemical flow cell.

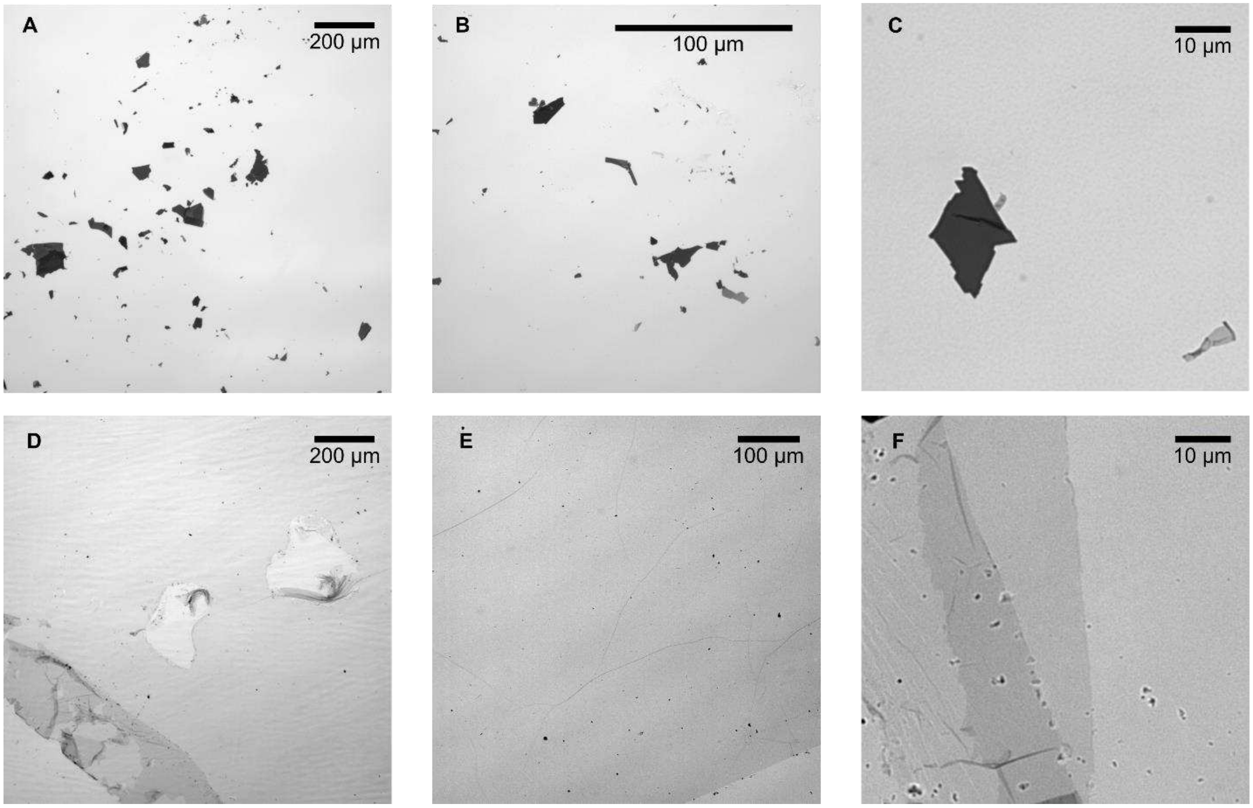

Fig. B.2 – Additional Example MoS_2 Transmission Images. (**A**) 10× image showing a variety of flake shapes and lateral sizes of mechanically exfoliated MoS_2 crystals on ITO. (**B**) 60× image showing similar flakes of a variety of thickness (as assessed by optical density). (**C**) Higher resolution 60× image showing intraflake differences in thickness. (**D**) 10× image showing macroscopic defects include two interior tears and a bilayer edge fold. (**E**) 20× image showing dark particulate debris and interior micro-folds. (**F**) 60× image showing bilayer regions and particulate debris. All images illuminated with white lamp.

B.3 Determination of Nanoflake Thickness

We calculate nanoflake thickness by correlating optical density values obtained via bright field transmission images with profilometry data of individual mechanically exfoliated MoS_2 nanoflakes. We measure the nanoflakes on identical ITO substrates prior to encapsulation inside the electrochemical flow cell. First, we collect brightfield transmission images of the nanoflakes with an inverted Olympus optical microscope (IX73) with a 60× objective. The nanoflakes in the main text (Fig. 3.2 and **Fig. 3.**3) ranged from 25 to 200 μm in lateral size. The light source for all transmission imaging is a white halogen lamp (Olympus U-LH100-3). The total illumination area was ca. 250 x 250 μm^2 with average irradiance of ca. 0.01 $W\cdot cm^{-2}$. The camera is a sensitive Photometrics Prime 95B back-illuminated camera with 1200 × 1200 pixel array 11 μm CMOS detector. We calculate spatially resolved OD values following transmittance intensity measurements reported previously.**[78]** Briefly, we calculate OD $=\log(I/I_0) = -\log(T)$, where I is the light transmitted through a region of an MoS_2 nanoflake and I_0 is the light transmitted through an adjacent ITO background region.

Next, we measure the thickness of the same regions of the same nanoflake using a DektakXT profilometer with stylus radius of 12.5 μm. The profilometry data was background subtracted and surface-leveled using Vision64 software (ver. 5.40). The profilometer minimum vertical range was 6.5 um (0.1 nm bit resolution) with stylus force of 1 mg. Mapping steps between line scans ranged from 5 to 10 μm. The profile height sensitivity is limited to the surface roughness of 3-4 nm RMS.

Fig. B.3A shows a single profilometry line scan and bright field optical transmission image of the same MoS_2 nanoflake. **Fig. B.**3B shows a complete profilometry map and transmission image for another representative nanoflake. We calculated OD values and height profiles for different smooth regions of many nanoflakes. **Fig. B.**3 shows the OD increases exponentially with layer thickness, in agreement with Beer's law. We fit the data to a power function (OD) = A $(\text{thickness})^B$ + C. The offset parameter, C, pinned the fit through the measured OD (0.014) and known thickness (0.7 nm) of a monolayer MoS_2 crystal. We could not resolve MoS_2 step edges less than 5 nm due to the surface roughness of the ITO substrate and the limitations of the instrument.

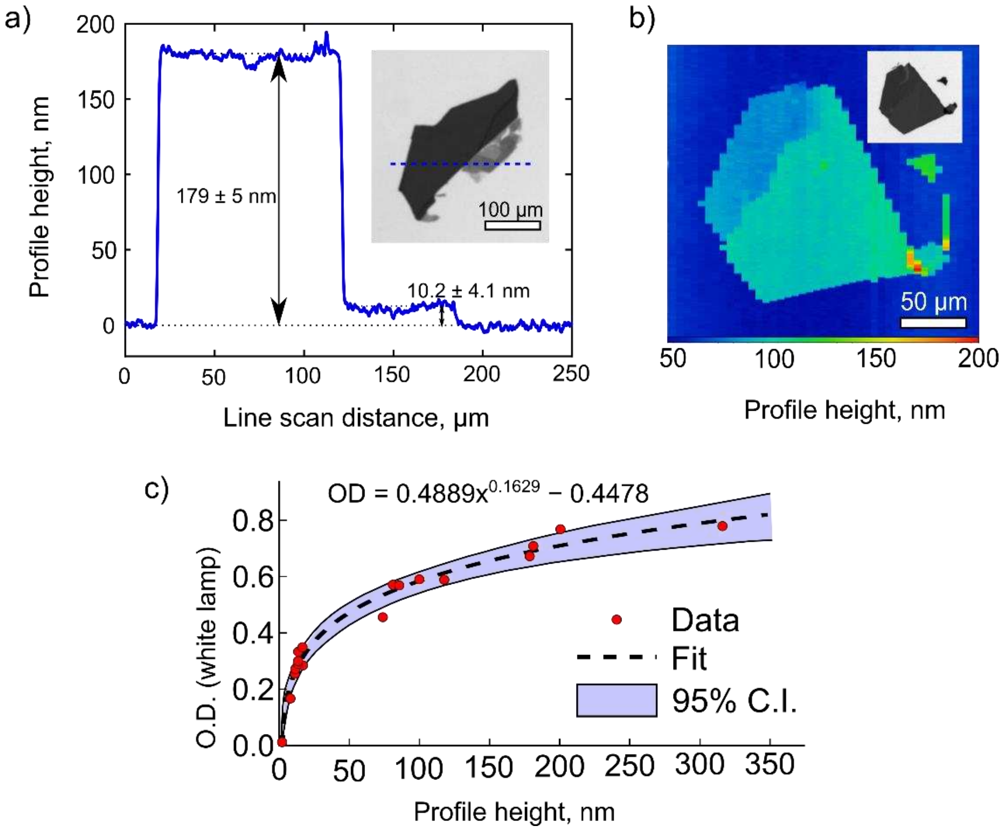

Fig. B.3 – Correlated profilometry and bright field transmission images. (**A**) Profilometer line scan across a MoS_2 nanoflake on ITO. The inset shows the correlated transmission image with dashed line representing the 250 um line scan. (**B**) 200 x 250 µm profilometry map of a representative MoS_2 nanoflake. We calculated the thickness for basal nanoflake regions after leveling and subtracting the substrate profile background. (**C**) OD versus profile height for 18 different nanoflake regions. We added a single data point at 0.7 nm for the OD value of monolayer MoS_2, as confirmed by absorbance and Raman measurements.

B.4 Transmission Image Processing

Image post-processing occurred using custom code in MATLAB (ver. R2023a). To detect the pixels associated with MoS_2 nanoflakes, we first applied a cut-off threshold to each image. All pixels lower than the mean minus 3σ of the background pixel intensity were defined as nanoflakes. For each image, we identified the nanoflake edge boundary pixels using the Canny edge function with the upper limit of 0.2, lower limit of 0.1, and 0.5 Gaussian filter parameter. The transmission images in Fig. B.4 below show the darker nanoflake material within the determined edge boundary before (green, outer line) and after (red, inner line) an applied potential step.

For each potential step, we calculated the Euclidean distance between each edge pixel of the first image to the nearest neighbor edge pixel in the final image of the movie. Each initial edge pixel position is assigned a length ($\boldsymbol{\ell}$, μm) from this vector distance (see zoom-in region for E= +1.55 V in Fig. B.4). For each one-hour potential step measurement, we define the nanoflake's lateral anodic dissolution rate (L, μm/hr) as the mean $\boldsymbol{\ell}$. Fig. B.4 shows a relative frequency distribution of $\boldsymbol{\ell}$ values for the potential steps E = +1.5 V (yellow, left), +1.55 V (blue, center), and +1.60 V (red, right). Because of non-concentric nanoflake shapes, the $\boldsymbol{\ell}$ distributions can skew for faster dissolution rates.

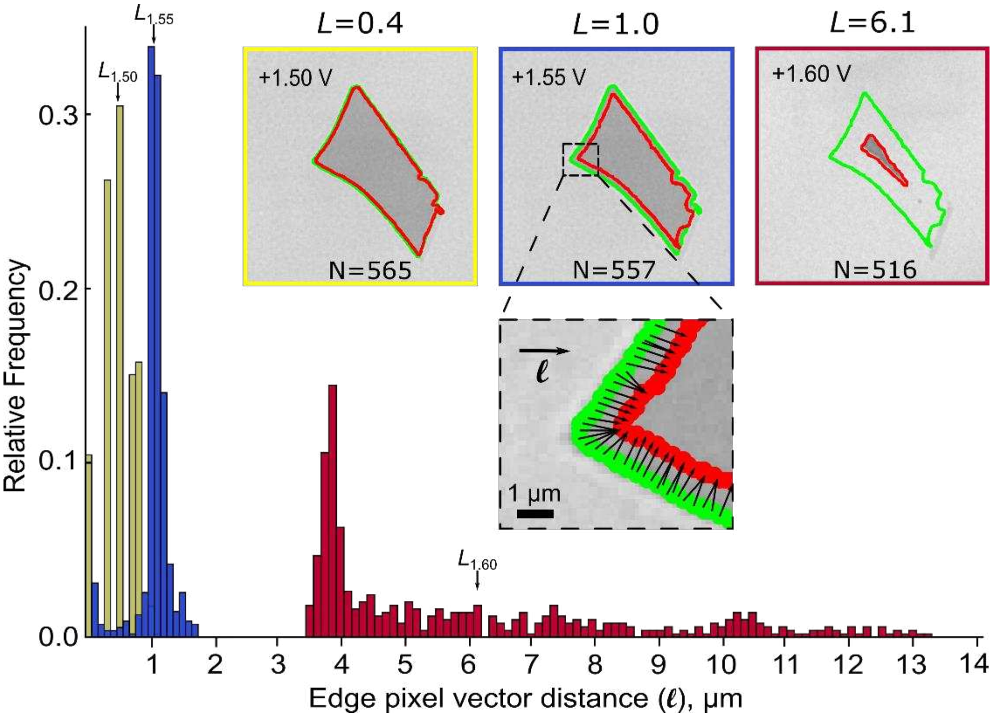

Fig. B.4 – Relative frequency distribution of individual edge distance vectors (ℓ) between sequential potential steps (+1.50, +1.55, and +1.60 V) for the nanoflake shown in Figure 4.1. The dissolution rates (*L*) reported in the main text are the average of all **ℓ** values for a nanoflake during a one-hour applied potential step. The inset images show the initial edge boundary (green) and final edge boundary (red) for each potential step. N represents the total number of edge pixels evaluated at the beginning of each potential step (i.e., total number of **ℓ** values for the respective potential step).

B.5 Influence of H_2O on Anodic Dissolution Rate

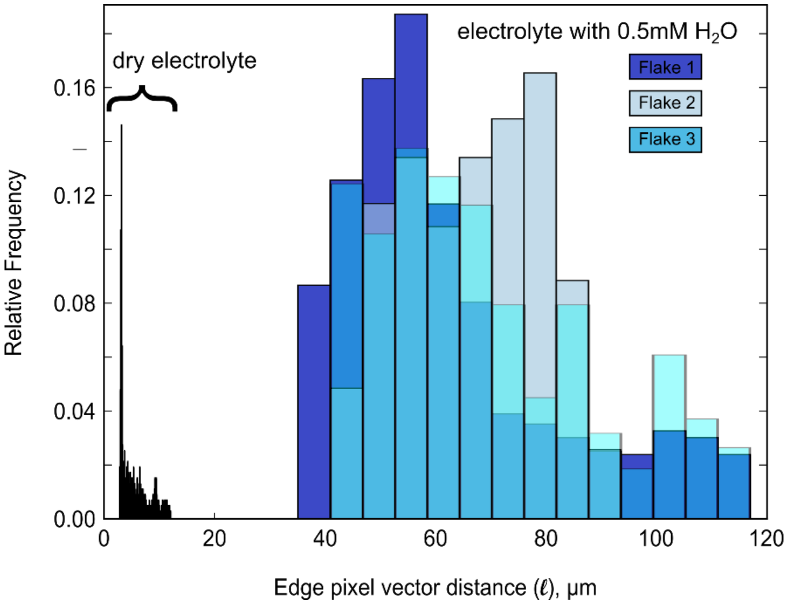

Fig. B.5 – Histogram of edge distance vectors (ℓ) for three nanoflakes after 150 μL of deionized H_2O was added to 15 mL of N_2 purged electrolyte solution. For comparison, an example distribution of edge distance vectors obtained from the neat acetonitrile electrolyte is shown in black. The calculated L values are an order of magnitude larger (60-68 μm/hr) for H_2O-exposed nanoflakes as compared to those in dry electrolyte (1-6 μm/hr). All data for measurements at $E = + 1.60$ V.

B.6 Interior versus Edge OD changes during Dissolution

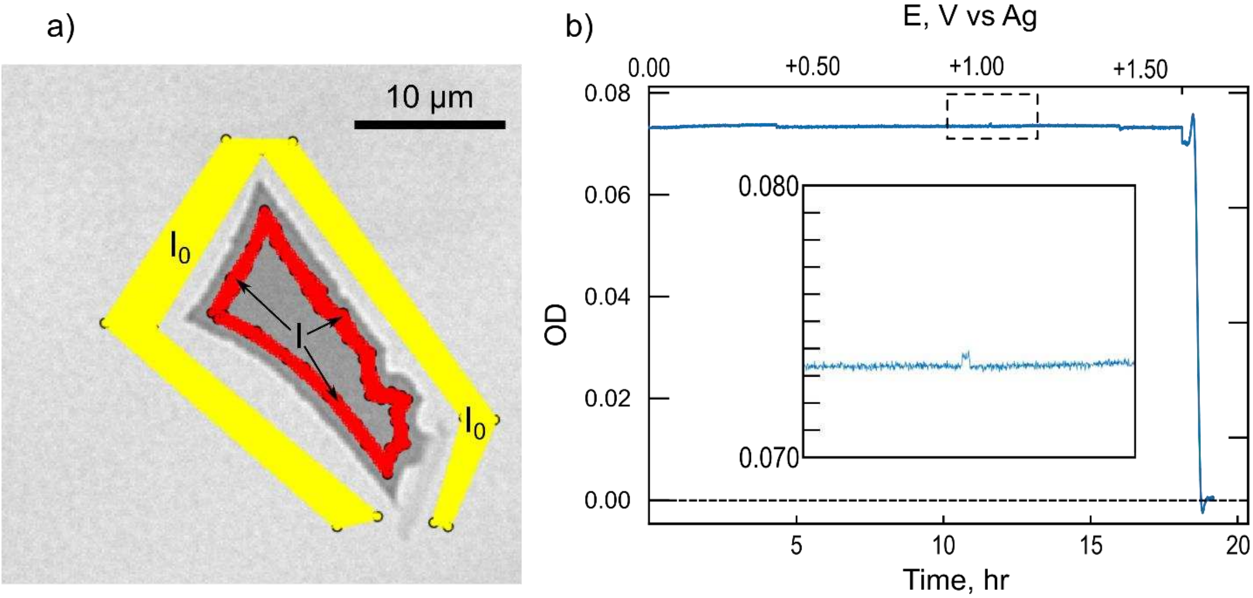

Fig. B.6 – Uniform edge dissolution of nanoflake. (**A**) Bright field transmission image of the same nanoflake as Fig. 3.1. The yellow and red pixels represent the light transmitted through the ITO background (I_0, yellow band outside nanoflake) and MoS_2 nanoflake (I, red band within nanoflake interior) regions. The transmission intensities of all pixels within the yellow and red regions were averaged to measure OD, where $OD = \log_{10}(I_0/I)$. (**B**) OD for the sample region in (**A**) versus time. The OD is stable within ±0.002, until the interior sample region undergoes anodic dissolution. The key point is that the edge pixels exhibit anodic dissolution but the interior nanoflake region remains intact.

B.7 Natural Versus Synthetic MoS_2 Transmission Images

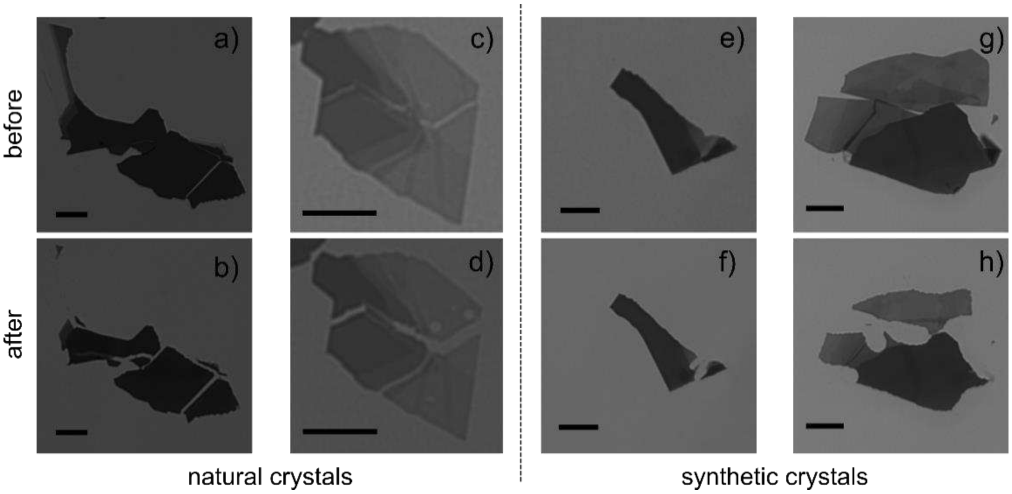

Fig. B.7 – Representative bright field transmission images of exfoliated MoS_2 nanoflakes before (top) and after (bottom) anodic dissolution. (**A-D**) Naturally occurring crystals from SPI. (**E-H**) Synthetic crystals from 2D Semiconductors. We observed more prevalent cracking and pitting in these nanoflake samples than the natural MoS_2 crystals, presumably due to doping heterogeneity or dislocations in these crystals. All scale bars represent 10 μm.

B.8 Correlation between nanoflake physical properties and E*D.*

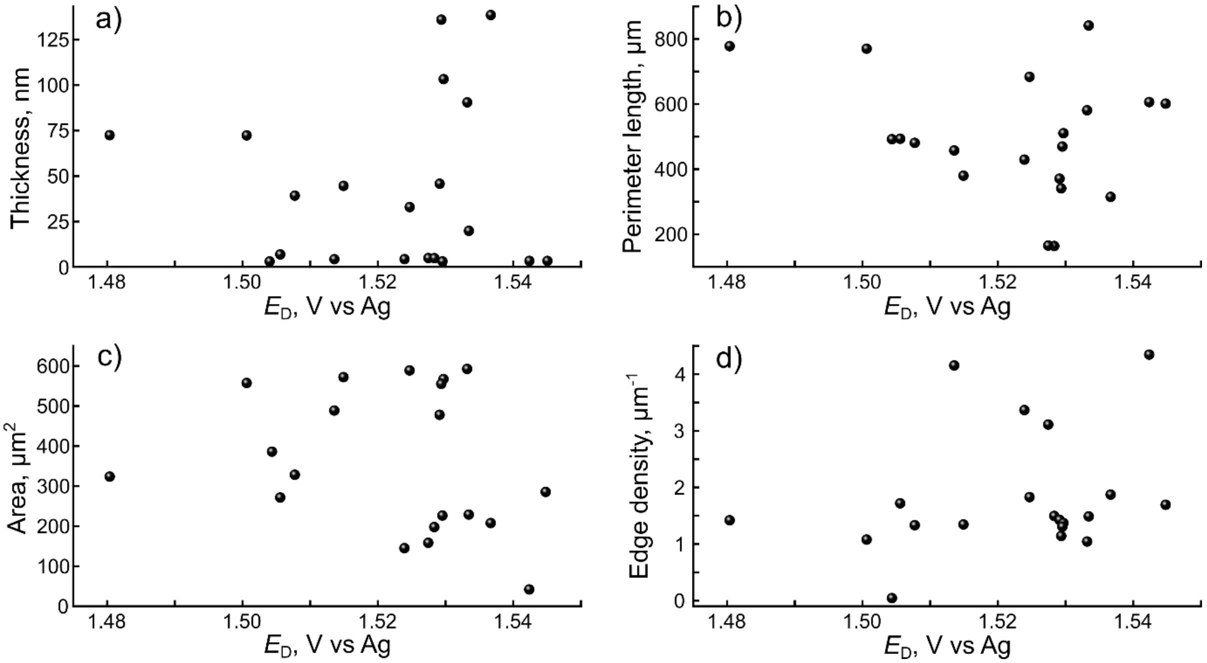

Fig. B.8 – (A) Optical density (OD), (B) perimeter length, (C) area, and (D) edge density (perimeter/area). Each data point represents one MoS$_2$ nanoflake (N=20).

B.9 Impervious Monolayer "Footprints"

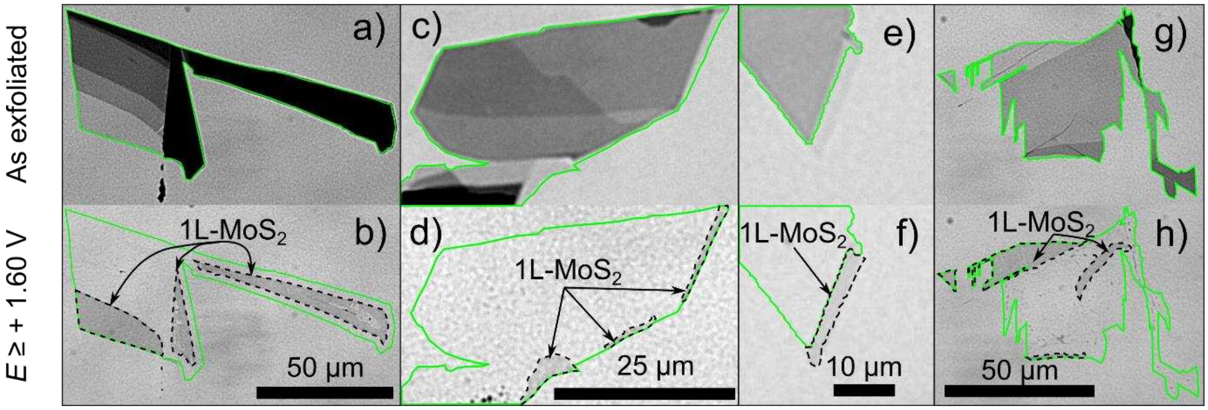

Fig. B.9 – Transmission images of monolayer MoS$_2$ regions that are uniquely impervious to anodic dissolution. (**A-B**) Mechanically exfoliated flakes before (**A**) and after (**B**) the 20-hour potential waveform in Figure 1c of the main text. The solid green (black dashed) boundary depicts the MoS$_2$ edge before (after) the 20-hour measurement. (**C-D**), (**E-F**), and (**G-H**) are the same as (**A-B**), but for additional nanoflake examples.

B.10 Impervious Monolayer MOCVD-grown MoS_2

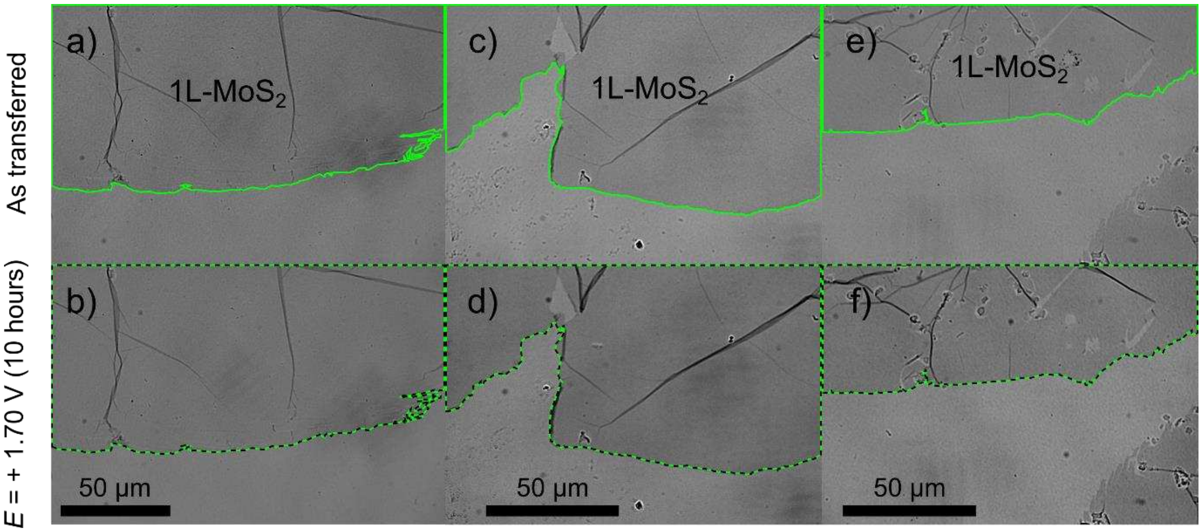

Fig. B.10 – Synthetic 1L MoS_2 sheets do not dissolute. (**A-B**) Transmission images of a CVD-grown monolayer MoS_2 sample in an electrochemical flow cell before (**A**) and after (**B**) more than 12 hours and $E \geq +1.60$ V. The solid green (dashed black) boundary depicts the MoS_2 edge before (after) electrochemical experiments. (**C-D**) and (**E-F**), same as (**A-B**), but for different regions of the sample. We observed neither edge nor interior dissolution for $E = +1.70$ V.

B.11 Monte Carlo Optimized Region of Interest (ROI) Selection

A Monte Carlo routine was used to calculate absorbance spectra for a defined subset of transmission image pixels within each ROI. The usefulness of this routine was two-fold: (1) it optimized the time required to analyse the substantial hyperspectral datacube, and (2) it indicated the optimal ROI size to reduce variance in the optical measurement. The ROI size used in the Monte Carlo routine is a subset of random pixels bound within a user-defined region of the transmission image (Fig 4.2C). The total size of that ROI is typically 10 – 50 μm in lateral dimensions, corresponding to a total of 15,000 or more pixels. The Monte Carlo routine iterates the absorbance calculation for the same image stack while using randomly selecting a defined number of pixels within the ROI. Fig. B.11 below shows the influence of ROI size on δA where each square pixel represents 183 nm x 183 nm (0.03 μm^2). Keeping in mind that δA is limited to < 0.003 from the "image-to-image" sample variation, an ROI pixel size of 1000 or more is selected to ensure the ROI sample size does not dominate δA.

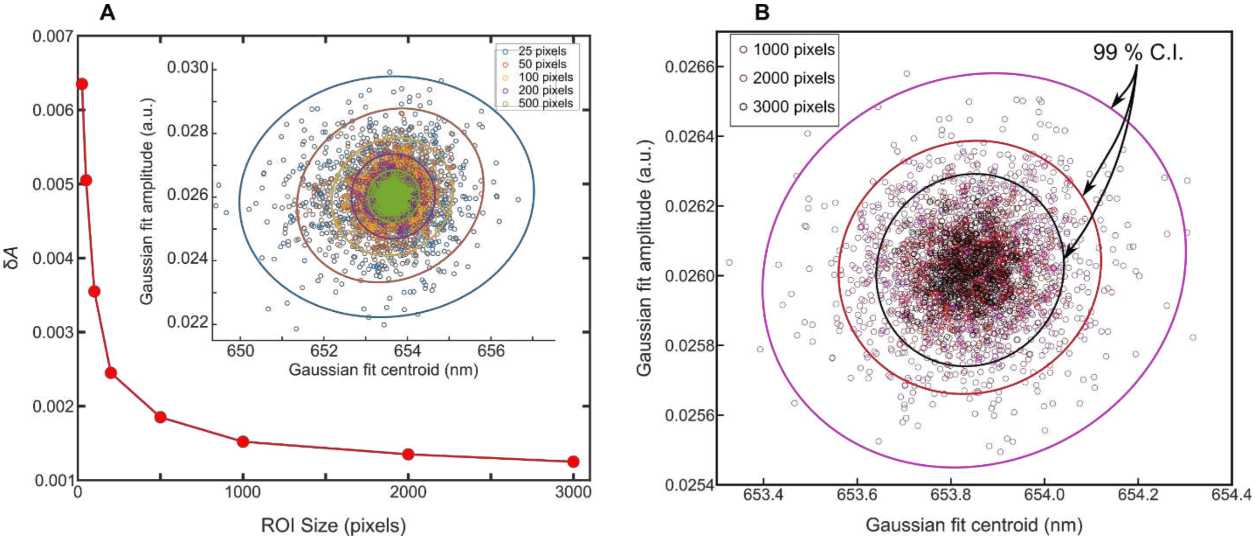

Fig. B.11 – Monte Carlo Optimization to Predict Uncertainty from MoS$_2$ heterogeneity. Results of 1,000 independent absorbance spectra calculations using randomly selected pixels of varying ROI size. **(A)** Red markers show uncertainty in absorbance (δA) as a function of the number of random pixels selected within the ROI. The inset shows a scatter plot of the 1000 best fit parameters for each spectrum using 25 to 500 random pixels; **(B)** Ellipses denote the 99 % confidence intervals (C.I.) in the absorbance peak Gaussian fit parameters for the three largest effective ROI sizes. The range of peak amplitude fits (i.e. absorbance) is consistently < 0.002 for ROIs comprised of 1,000 or more pixels. The random pixels are selected from a user-defined ROI region that is > 15,000 pixels.

Noting Fig. B.11 and Fig 4.3, the ML-MoS$_2$ samples are optically homogenous across domains that are tens of micrometers in lateral dimensions. The absorbance spectrum and δA is independently calculated for each iteration. For example, the inset of Fig. B.11 A shows the results of 1,000 Monte Carlo iterations using several different ROI sizes. The A exciton/trion superpeak amplitude and centroid is fit to a Gaussian function for each iteration.

B.12 Trial-to-trial Reproducibility

Concerning the reproducibility of the potential-dependent absorbance data in Chapter 4 and 5, several different electrochemical flow cells and ML-MoS_2 regions therein were measured. The fractional uncertainty of the background region $\left(\frac{\delta I_0}{\delta I}\right)$ was spatially invariant, so differences in calculated absorbance values likely stem from spatial heterogeneity of the ML-MoS_2 material. While outside the scope of this study, we attribute the spatial variance of the absorbance values to heterogenous domains of varying charge impurities, non-uniform substrate contact (i.e. atomic-scale “wrinkling”), or other defects. The data points in Figure B.12 below represent the Gaussian fit of the A-exciton/trion superpeak for simplicity.

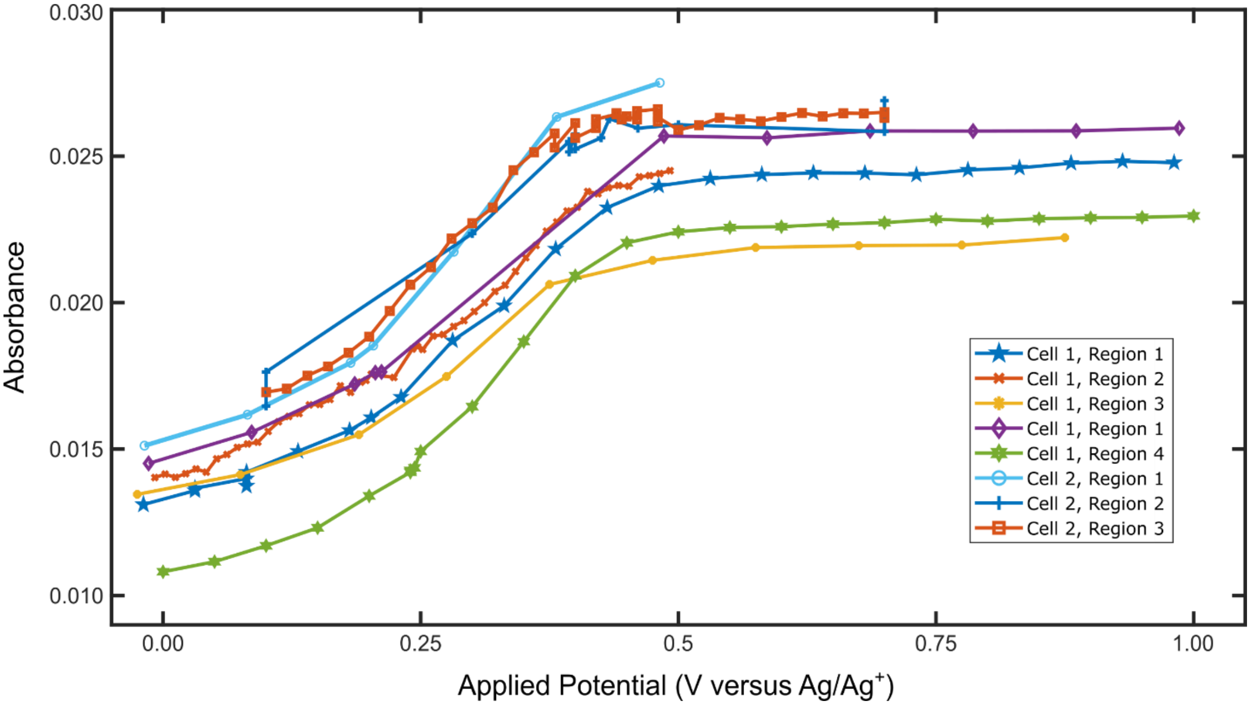

Figure B.12 – Multi-trial Potential-Dependent Comparison of A Exciton Peak Absorbance Measurements. Absorbance values versus *E* for multiple ML-MoS_2 regions among different electrochemical flow cells.

LIST OF ABBREVIATIONS

Abbreviation	**Description**
ML-MoS_2	Monolayer molybdenum disulfide
2D	Two-dimensional; sheet-like material that is 1-3 atoms thick
ITO	Indium-doped tin oxide coated glass substrate
MOCVD	Metal-organic chemical vapor deposition synthesis technique
WE	Working electrode
CE	Counter electrode
RE	Reference electrode
E	Applied potential (non-equilibrium), V vs reference
E_{onset}	Onset potential, V vs reference
E	Energy, eV
$\mathrm{E_F}$	Fermi energy, eV
$\mathrm{E_{CB}}$	Conduction Band Edge (minimum), eV
$\mathrm{E_{VB}}$	Valence Band Edge (maximum), eV
$\mathrm{E_g}$	Band gap energy, eV
$\mathrm{E_{A0}/E_{A^-}}$	A exciton/trion energy
$\Delta \mathrm{G_{CT}}$	Gibbs Free Energy of charge transfer
k_{ET}	interfacial electron transfer rate constant
n	Charge carrier concentration. Here, electron density of 2D material, cm^{-2}
MND	Mahan-Noziéres-De Dominicis
WM	Wannier-Mott
BGR	Band gap renormalization
$\Delta \mathrm{G_{CT}}$	Gibbs Free Energy of charge transfer